Sources paramétriques de haute énergie et de haute cadence dans l'infrarouge moyen et leurs applications en champ fort

Giedre Marija Archipovaite

université de BORDEAUX

THESIS PRESENTED

TO OBTAIN THE QUALIFICATION OF

DOCTOR OF

THE UNIVERSITY OF BORDEAUX

PHYSICS AND INGINEERING

LASERS, MATERIAL AND NANOSCIENCE

Giedrė Marija Archipovaitė

HIGH ENERGY AND HIGH REPETITION RATE PARAMETRIC SOURCES IN THE MID-WAVELENGTH INFRARED AND THEIR APPLICATIONS

Viva on 25 September 2018

Members of the examination panel:

Dr. Emma Springate	Central Laser Facility, STFC	Rapporteur
Dr. Jean-François Hergott	CEA Saclay	Rapporteur
Prof. Andrius Baltuška	Photonics institute, TU Wien	Examiner
Dr. Rytis Butkus	LRC, Vilnius University	Examiner
Prof. Lionel Canioni	CELIA, University of Bordeaux	President
Prof. Eric Cormier	CELIA, University of Bordeaux	Supervisor
Dr. Jean-Christophe Delagnes	CELIA, University of Bordeaux	Co-supervisor
Dr. Stéphane Petit	CELIA, CNRS	Co-supervisor

Abstract

Ultrashort pulse light sources in the near- to mid-wavelength infrared spectral region are in high demand for strong field physics in atoms, molecules and condensed matter. According to the three step model [1], the energy cut off of generated high harmonics scales as $I \times \lambda^2$, which favors longer driving wavelengths in order to generate more energetic XUV photons, and potentially shorter attosecond, soft X-ray pulses. Unfortunately, photon energy extension is at the cost of an efficiency drop scaling as $\lambda^{-5.5}$ [2]. The availability of a high-repetition-rate laser system is paramount to mitigate the efficiency issues and still produce high photon fluxes. Even though there are only a few laser gain media suitable for intense femtosecond pulse generation in the mid-IR spectral region, the overall scalability of the pulse repetition rate, the duration and power are still a challenge [3, 4]. Thus, parametric systems based on a nonlinear three wave-mixing, are an attractive alternative to generate the required ultrashort pulses for those experiments. Currently high power middle infrared parametric systems can't reach the required intensities to reliably drive high harmonic generation (HHG) in gas. However, these sources are attractive drivers for HHG in solids, which requires lower intensities on the target. On the other hand, high energy, but lower repetition rate systems are capable of generating energetic pulses for HHG experiments in gas. However, the overall efficiency of those drivers is still low. Depending on the required harmonics energy, the XUV could be efficiently generated by post-compressed NIR lasers.

This thesis describes the development of MWIR sources and their applications in strong field physics. We have chosen to investigate parametric sources driven by high average power fiber CPA pump laser and by high energy Yb:CaF_2 bulk laser system. The generated MWIR few cycle pulses are then used to probe laser material interaction through HHG in solids and gases.

Abstract

Les sources lasers à impulsions ultracourtes de forte puissance dans la région spectrale du proche à moyen infrarouge sont très demandées pour la physique des champs forts dans les atomes, les molécules et la matière condensée. D'après le modèle en trois étapes [1], l'énergie coupée des harmoniques élevées générées varie comme $I \times \lambda^2$. Cela favorise les longueurs d'onde plus longues pour générer des photons XUV plus énergétiques, et potentiellement des impulsions attosecondes plus courtes. Malheureusement, l'extension de l'énergie des photons se fait au prix d'une diminution de l'efficacité en $\lambda^{-5,5}$ [2]. La disponibilité d'un système laser à haute cadence est un atout majeur pour palier aux problèmes d'efficacité et produire des flux de photons élevés. Même s'il existe quelques matérieux de gain laser adaptés à la génération d'impulsions femtoseconde intense dans la région spectrale infrarouge intermédiaire, l'amélioration globale du taux de répétition, de la durée et de la puissance des impulsions sont encore des défis [3, 4]. Ainsi, les systèmes paramétriques basés sur un mélange non linéaire à trois ondes sont une alternative intéressante pour générer les impulsions ultracourtes requises pour ce type d'expériences. Actuellement, les systémes paramétriques à haute puissance dans l'infrarouge moyen ne peuvent pas atteindre les intensités requises pour génerer des harmoniques dans le gaz. Cependant, ces sources sont des moteurs intéressants pour la genération d'harmonique (HHG) dans les solides, qui nécessitent des intensités sur cible plus faibles. Par ailleurs, les systèmes à haute énergie, mais à taux de répétition plus bas, sont capables de générer des impulsions suffisamment énergétiques pour les expériences HHG dans le gaz. Cependant, l'efficacité globale de ces sources est encore faible. En fonction de l'énergie harmonique requise, le rayonnement peut être généré efficacement par des lasers NIR post-comprimés.

Cette thèse décrit le développement des sources MWIR et leurs applications en physique des champs forts. Nous avons choisi d'étudier des sources paramétriques pilotées par un laser à pompe CPA de puissance moyenne élevée et par un système laser à grande énergie Yb: CaF_2. Les impulsions MWIR générées sont ensuite utilisées pour sonder l'interaction du matériau laser à travers HHG dans les solides et les gaz.

Acknowledgements

There are many amazing people that I have met, worked and became friends with during the time I've spent in Bordeaux and Vienna doing awesome science. These three years were the time when I grew up a lot as a scientist, which wouldn't have happened without my supervisors and colleagues from CELIA, TU Wien, University of Grenoble, INRS and Szeged. I'd like to thank all of you for taking part in it.

First of all I'm very grateful for the CELIA team: Eric Cormier, Stéphane Petit and Jean-Christophe Delagnes. Thank you for the supervision and help with the experiments as well as for the freedom to work independently.

I'm equally grateful for Vienna team: Andrius Baltuška, Tadas Balčiūnas and Guangyu Fan. The experimental campaigns were challenging, but interesting. Also to the rest of Viennese team for great times during lunch breaks and after work.

To Sophie, Céline, Sonia, Emmanuelle and Melanie. Another lost foreigner was saved in the jungles of paperwork.

To the whole CELIA community. Morning chats in the coffee room, Christmas lunch, annual BBQ and Molkky cup – it was great to be a part of all of this.

It was also a pleasure to participate in the Bordeaux Optics Student Chapter activities. Interlabs and quizes were fun to organize, hope you'll continue celebrating the Pi(e) day and take care of my cardboard table tennis!

To the Bordeaux Lindy Hop community. You guys are awesome! I had a really great time with you in classes, socials, festivals and non-dancing activities. Thank you and see you on the dance floor! Couchsurfers, you're not forgotten, thank you for the picnics, weekly meetings and all the other random gatherings! Laser Trash Pandas, for the victories in Sunday

Pub Quiz!

A special part in my life is taken by my family and friends. Thank you for your support and encouragement. The process would have been much harder without you.

And last, but not least, all of this wouldn't have happened without the Laphia support. Thank you for choosing me to do science under your funding!

Contents

List of Figures

Notes

Subdivision of Infrared spectrum

The following subdivision scheme [18] of infrared spectrum will be used in this thesis:

Table 1 Subdivision of Infrared spectrum.

Division name	Abbreviation	Wavelength, μm
Near-infrared	NIR	0.75–1.4
Short-wavelength infrared	SWIR	1.4–3
Mid-wavelength infrared	MWIR	3–8
Long-wavelength infrared	LWIR	8–15

Abbreviations

BBO – Beta Barium Borate
CEP – Carrier Envelope Phase
DFG – Difference Frequency Generation
FCPA – Fiber Chirped Pulse Amplifier
FROG – Frequency Resolved Optical Gating
FWHM – Full Width Half Maximum
GRIIRA – Green Induced Infrared Absorption
GVM – Group Velocity Mismatch
HCF – Hollow Core fiber
HHG – High Harmonics Generation
IAP – Isolated Attosecond Pulse
IP – Ionization Potential
KTA – Potassium Titanyle Arsenate
LIDT – Laser Induced Damage Threshold

LN – Lithium Niobate
OPA – Optical Parametric Amplifier
OPCPA – Optical Parametric Chirped Pulse Amplifier
PPLN – Periodically Poled Lithium Niobate
SF – Sum Frequency
SHG – Second Harmonic Generation
WLC – White Light Continuum
XUV – Extreme ultraviolet radiation
YAG – Yttrium Aluminum Garnet
Yb:FCPA – Ytterbium doped Fiber Chirped Pulse Amplifier

Introduction

Starting this year, UNESCO declared May 16 to be the International Day of Light. The day is chosen to commemorate the demonstration of the first laser – ruby laser by Theodore Maiman on May 16, 1960 [19]. This also notes the time when, the photonics era started. Shortly after the demonstration of the first laser in 1961, the first parametric process – second harmonic generation – was demonstrated [5]. The efficiency of the process was very low at the order of 10^{-8}. In fact, the efficiency was so low, that the technician of the journal removed the second harmonic signal thinking that it was just some dust or another unimportant signal noise and the arrow pointed to nothing [20].

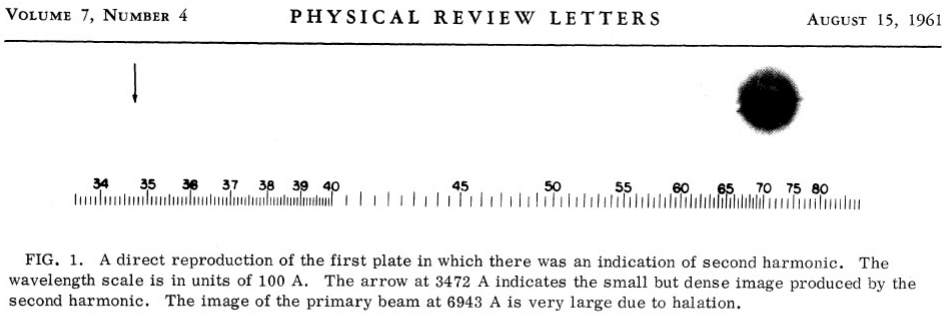

Figure 1 First demonstration of SHG generation. (Picture from [5]).

However it did not take long to define the phase-matching conditions and demonstrate the birefringence phase-matching in KDP crystal [21, 22]. A few years later, the optical parametric amplification was demonstrated by a few groups at the same time: Bell Telephone Laboratories [23] and Moscow State University [24]. In [24] a Nd:Glass laser was used and the fundamental signal at 1.06 μm was amplified by the second harmonic beam, while in [23] signal was at 0.63 μm. However, back then pump lasers featured long pulse durations and the ultrafast phenomena started a few decades later in the 90's after the demonstration of Ti:Sapphire (Ti:Sa) laser [25]. Ti:Sa lasers feature broandband spectra, thus ultrashort pulses could be generated with pulse energies of mJ level at kHz repetition rate. Although one could

argue that dye lasers were successfully used to generate femtosecond pulses from the 80's, they required constant maintenance, which involved handling poisonous and carcinogenic materials. Dye lasers emit radiation mostly in the visible and near infrared spectral region, and are attractive laser sources due to their wavelength tunability. Thus, Ti:Sa lasers became very common sources to pump fs OPAs. One of the reasons why Ti:Sa lasers were able to develop so successfully, was that MIT did not claim a patent. Many companies contributed into the development and helped to build the technology [26]. This provided solid products. After almost 30 years, these lasers are one of the most commonly used laser sources for pumping ultrashort OPAs.

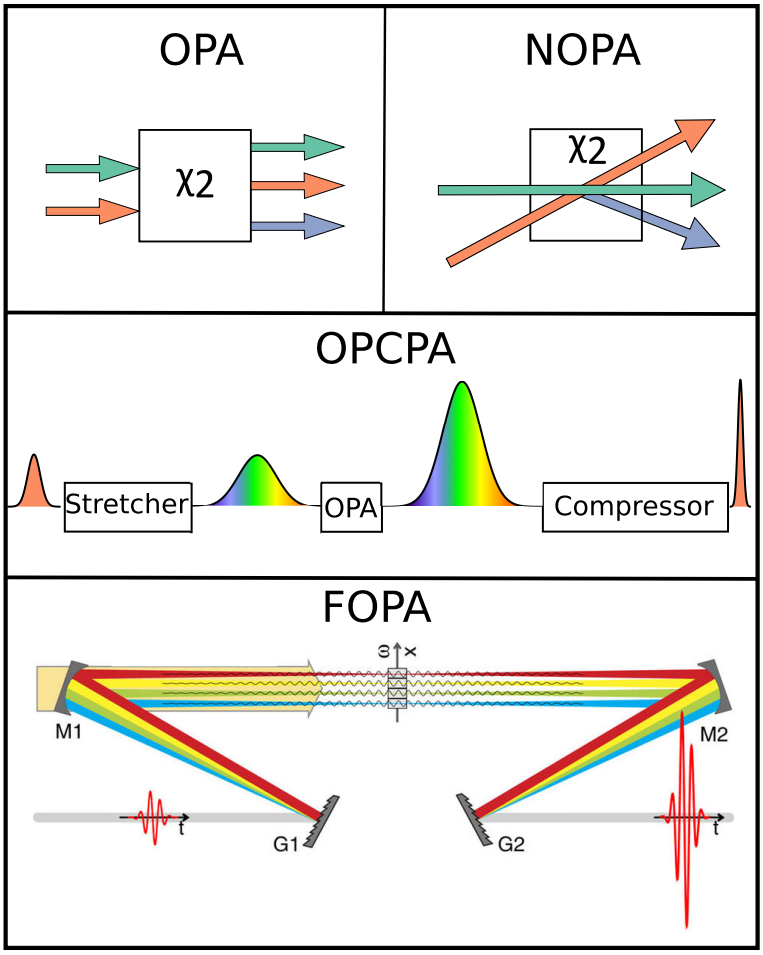

Figure 2 Different schemes for optical parametric amplification: Collinear OPA (top left), Non-collinear OPA(top right), OPCPA (middle), FOPA (bottom) (Figure for FOPA taken from from [6]).

Modified OPA techniques such as non-collinear OPA (NOPA) (Fig.2 top right), optical parametric chirp pulse amplification (OPCPA) (Fig.2 middle) or Fourier-domain optical parametric amplification (FOPA) (Fig.2 bottom) could be used to produce broadband amplification and result in shorter pulses or increased amplified pulse energy. The only difference between the OPA and NOPA is that in the case of NOPA, there is an angle between the signal and pump beams, which allows it to match the group velocities of the two pulses and broaden the amplification bandwidth. However, NOPA results in an angularly chirped idler beam, which limits the use of both beams in this configuration. OPCPA was developed in 1992 by Dubietis et al. [27] and this method is based on the same principle as the CPA, just adapted for the parametric amplifiers. In order to avoid nonlinear crystal damage during the amplification process, a short seed pulse is stretched in time, then after the pulse is amplified it is compressed back to the minimal duration, supported by the spectrum. The main advantage of OPCPA versus CPA is the capability to amplify broader spectra with the potential of tuning the central wavelength. FOPA was inspired by spatially dispersed amplifiers [28] and adapted for the OPAs by François Légaré group at INRS [6]. It uses a similar principle: the seed is dispersed by a grating and the nonlinear crystal is placed in the fourier plane. Then the pulse is reconstructed back to the initial pulse by another symmetrically placed grating, which recollects the spectrum. Furthermore, in the case of FOPA, multiple crystals with slightly detuned phase-matching angles could be placed in the Fourier plane, thus using one pump beam, an ultra-broadband amplification could be achieved.

Another method to achieve intense ultrashort pulses is to use multiple-beam pumping schemes. Here, a single signal is pumped with multiple pump beams, where each of them satisfies the phase-matching conditions. This was studied by a few groups: Smilgevičius at Vilnius University [29–31] and Mennerat [32] at CEA. It seemed to be a very promising technique for a few reasons. At the time, when experiments started, commercially available lasers featured low repetition rates for higher energy pulses, thus multiple beam pumping would increase the intensity on the crystal, which results in higher energy amplified pulses at a higher repetition rate. By adjusting the direction of the pump beam, the phase-matching conditions could be tuned and a broader spectrum could be amplified. Despite these benefits, this method's disadvantages outweigh the advantages. Firstly, parametric diffraction reduces the efficiency of the amplification process, as the diffracted beams contains a significant amount of energy. Parametric diffraction could be reduced by using small angles [30], but then the phase of pump beams should be stabilized. After the quick development of high power fiber lasers [33–35] and thin disk lasers [36, 37], the need of high repetition rate

pump lasers was solved. Bulk Yb amplifiers also provide excellent trade off between pulse energy and repetition rate [38].

Most of the applications concerning the laser sources described in this thesis require ultrashort – few-cycle, intense laser pulses in the short-wavelength infrared (SWIR) or mid-wavelength infrared (MWIR). Despite the post-compressed amplified Ti:Sa lasers [39] and Yb-based [40, 41] or Tm:FCPA [42] sources, it is hard to achieve few-cycle pulses directly from the laser gain media. Thus, different types of three-wave nonlinear interactions in the nonlinear crystal are used: OPA, DFG between two pulses, or intra-pulse DFG [43]. After demonstrating excellent performance, high power lasers were applied to pump OPAs.

One of the main advantages of optical parametric amplifiers is the tunability. Not only is the broadband spectrum generated, but it also can be tuned within the phase-matching conditions within the crystal's transparency range. This makes OPAs an attractive source for multidimensional spectroscopy [44], ultrafast surface dynamics [45] and other strong field physics experiments.

The high harmonic generation (HHG) experiment generating harmonics at the keV range could be called the holy grail experiment of the first 10 or 15 years of the new millennium. 2018 marks the 25th anniversary of the Three-Step model introduced by Paul Corkum in 1993 [1]. The three steps in the model are: tunnel ionization of an atom, acceleration of the electron and photo-recombination of the electron with its parent ion. The energy cut-off for the HHG depends on the driving laser intensity, which is limited by the ionization of the generation media and the wavelength of the laser. The cut-off energy scales as $I \times \lambda^2$, which means that higher energy photons could be generated by driving the process with laser sources featuring longer wavelengths.

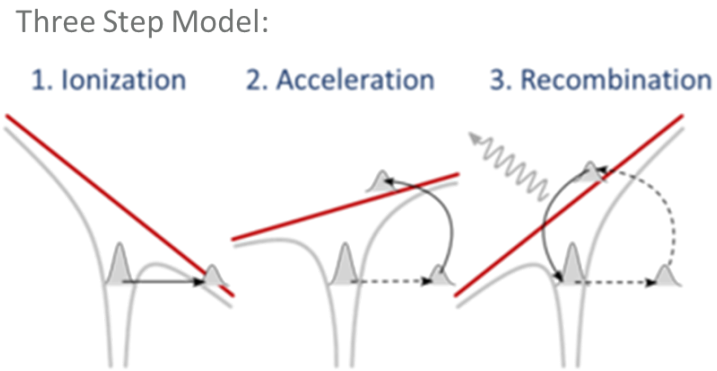

Figure 3 Three-Step model.

The mid-wavelength infrared OPA development faced the problem of a lack of suitable optics. The commonly-used fused silica (FS) is transparent up to 2.5 μm, but also features a strong absorption at 2.2 μm. A good replacement of FS is CaF_2, MgF_2, Ge or ZnSe, however optics made from these materials are more expensive and require coating, which adds costs to the overall set-up. It is even more tricky to manufacture polarization optics and diffraction gratings. Not to mention that commonly used nonlinear crystals with well developed growing techniques and good optical quality used in the near infrared OPAs are not suitable anymore, and new nonlinear crystals should be found. The lack of good quality optical elements in the short wavelength and middle wavelength infrared didn't prevent the development of systems at those wavelengths, however, the efficiency of high power OPAs was limited to 5% [46, 47].

The low efficiency limits HHG generation in gas with MWIR sources. A few experiments were done by the Kapteyn and Murnane group [48, 49] and the Baltuška group [50] and within the collaboration between both groups they have generated soft X-rays reaching keV region [51]. The HHG dependence on the wavelength was experimentally confirmed and the laser source requirements were estimated for different gases in a series of publications by the Kapteyn-Murnane group [48].

At the time where mid-wavelength infrared driven HHG was facing efficiency issues, the development of HHG sources took another direction – compact, reliable and user-friendly high harmonic sources featuring high flux for everyday use in experiments. Here HHG is driven by post-compressed Ti:Sa or Yb:FCPA lasers and harmonic signal could reach power level of sub-mW [52]. Furthermore, these sources at sub-100eV photon energies are already commercially available [53, 54].

Even though HHG in gas experiments attracted most attention first, lately more and more groups have started studying the high harmonic generation in solids, which is not the same as previously-mentioned HHG from solid targets. These experiments require lower intensities, thus high power OPAs are very attractive sources to drive them. Comparing with the HHG in gas, the cut-off in solids scales linearly with the electric field, while it scales linearly with the intensity for the dilute gas [55]. Also the emergence of the secondary plateau and different ellipticity dependence shows, that the electron dynamics is different from the Three-Step model, widely used to describe the HHG in gas. In the case of solids, two mechanisms, based on inter-band polarization and intra-band current, are being considered. Both of them rely on Bloch theorem [56].

But the progress in the mid-wavelength infrared OPAs side is also moving fast. Recently, a 150 µJ OPA at 3 µm was delivered to the Extreme Light Infrastructure (ELI) facilities by Fastlite [57] and the first results are to be reported soon. Another interesting switch happened with another ELI system – SYLOS, where initially a Ti:Sa based system was expected, but the Nd:YAG pumped OPA won the project call. This system works at 1 kHz repetition rate and generates CEP stable 45 mJ pulses with the duration shorter than 10 fs [57].

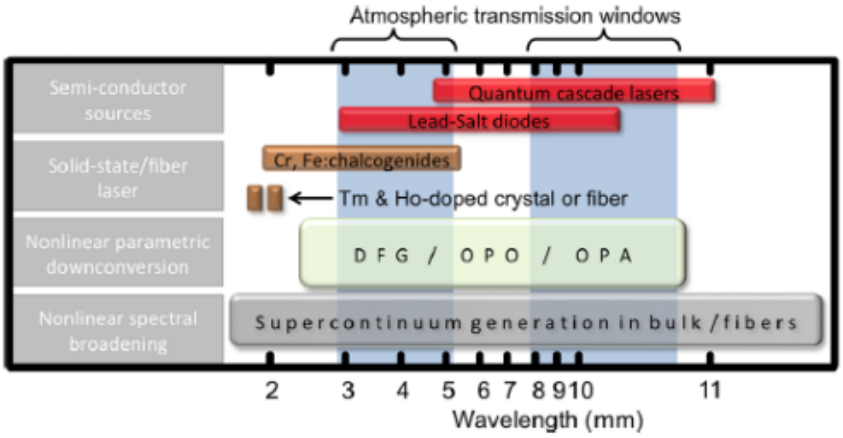

Figure 4 Sources covering MWIR spectral region. Picture taken from [7].

Even though this thesis focuses on parametric sources and their development, the SWIR and MWIR spectral regions could also be covered by semiconductor sources, solid state and fiber lasers as well as supercontinuum sources (See Fig.4). Unfortunately, the direct

intense femtosecond pulse generation from the laser gain medium in the SWIR and MWIR is still a challenge [3, 4]. However, a well developed Yb:FCPA technique (CPA adapted to fiber amplifiers) was successfully transferred to Tm:FCPAs. Current state of the art Tm doped FCPA laser systems [42] could be post-compressed in gas-filled-hollow core fibers and successfully used for high harmonics generation.

While the direct ultrashort pulses are on the way, one could still exploit the advantages of parametric sources: wavelength tunability and higher pulse energies, while pumping with high energy, lower repetition rate near infrared lasers. Therefore, this thesis will discuss the sophisticated beauty of the parametric source development. Also, a small part of this work is dedicated to an alternative solution for driving HHG in gas. When suitable, post-compressed diode pumped solid state lasers at 1 μm could be used.

The results provided in this thesis cover the development of the OPA sources in SWIR and MWIR and high harmonic generation experiments in gas and solids. There were a few important experiments conducted. Two main laser sources were used: high repetition rate ytterbium doped fiber CPA (Yb:FCPA) and high energy diode pumped solid state Yb lasers. In the first part of the thesis (chapter 2 and 3), experiments done with the high power system are described. This system is based in Bordeaux, CELIA laboratory and consists of:

- 2 μm OPA and its applications for testing new nonlinear crystal;
- 3 μm OPA and its applications for HHG in solids.

The high energy bulk Yb regenerative amplifier is located at Photononics Institute at Vienna University of Technology, where a few joint experimental campaigns within the collaboration with the Andrius Baltuška group were performed. Experiments done with this laser system are described in chapter 4:

- 2.4 μm high energy OPA;
- DFG in the middle infrared, tunable in the 5-10 μm range;
- HHG driven by short wave infrared;
- HHG driven by post-compressed Yb source.

Chapter 1

Optical parametric amplifiers

The process of optical parametric amplification (OPA) in nonlinear crystals is well known and described in [9, 58]. In this chapter, a short overview of the most important and relevant topics, necessary for successful development of the OPA systems in the SWIR and MWIR regions will be provided.

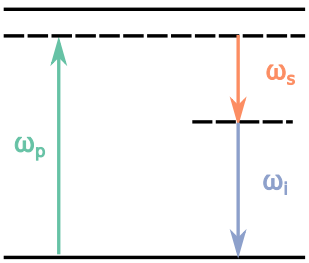

Figure 1.1 The energy levels for the process of optical parametric amplification; ω_p, ω_s, and ω_i are pump, signal and idler frequencies

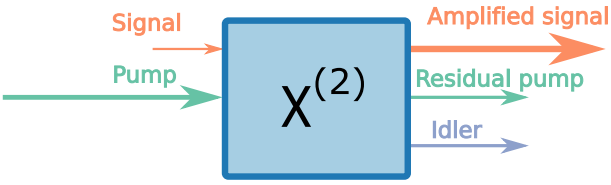

Figure 1.2 The process of optical parametric amplification in a non-centrosymmetric media exhibiting the second order nonlinearity (nonlinear crystal): a weak signal is amplified and idler generated at the cost of pump depletion.

The optical parametric amplification is a nonlinear process, which takes place in a nonlinear crystal. A nonlinear crystal is a non-centrosymmetric media exhibiting the second order nonlinearity. Fig.1.1 depicts the scheme of energy levels of the optical parametric generation process. There ω_p, ω_s, and ω_i are pump, signal and idler photon frequencies. It is a three-wave or three-photon interaction, where a strong pump photon disappears leading to the instantaneous creation of a signal and an idler photon. Figure 1.2 is a schematic of optical parametric amplification. The only difference between the generation and amplification is that in the case of optical parametric amplification, the signal photon is already present at the input of the nonlinear crystal, thus the signal gets amplified. The common designation for

pump, signal and idler photons is that the highest energy photon is a pump, the medium is a signal and the lowest energy photon is called an idler. Unfortunately, sometimes especially when the amplification of the difference frequency signal takes place, the designation of signal and idler interchange. So the idler beam could be also the one, which was additionally generated during the amplification process.

As OPA is a parametric process, there is no energy loss in the system. The energy is conserved and the process is instantaneous. Energy conservation law is written as:

$$\omega_p = \omega_s + \omega_i. \tag{1.1}$$

Momentum conservation sets an indispensable condition for the process to take place, which is known as the phase-matching condition:

$$\begin{aligned} n_p\omega_p &= n_s\omega_s + n_i\omega_i \\ \Delta k &= k_s + k_i - k_p \\ \Delta k &= 0; \end{aligned} \tag{1.2}$$

Here, n is the refractive index, where p, s and i idexes denotes pump, signal and idler waves. k is the wave vector and in order to obtain an effective nonlinear interaction between the three waves the phase mismatch (Δk) should be zero or very close to zero. In Fig.1.3 are sketched three main configurations for three wave mixing: non-collinear, not phase-matched (a); non-collinear, phase-matched (b); and collinear, phase-matched (c).

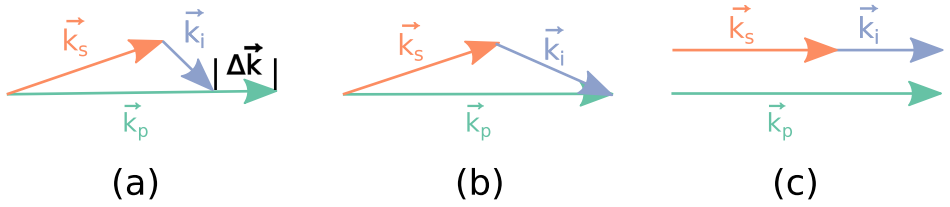

Figure 1.3 Wave vectors for non-collinear not phase-matched three-wave process (a), non-collinear, phase-matched three-wave process (b), and collinear three-wave process (c) in a nonlinear crystal.

Nonlinear coefficient

The nonlinear coefficient d_{eff} shows the effective nonlinearity of the crystal. d_{eff} depends on the crystal's symmetry and polarization of interacting waves. The coefficient is a simplified expression of the nonlinear susceptibility tensor, which is a 3×6 matrix with 10 independent

elements.

The d_{eff} calculations for all non-centro-symmetrical uniaxial crystal classes are discussed in [59]. For example, authors show, that for a negative uniaxial crystal of crystal class 3m (such as LN) the d_{eff} value for the type I phase-matching conditions is written by:

$$d_{il} = \begin{bmatrix} 0 & 0 & 0 & 0 & d_{31} & -d_{22} \\ -d_{22} & d_{22} & 0 & d_{31} & 0 & 0 \\ d_{31} & d_{31} & d_{33} & 0 & 0 & 0 \end{bmatrix}$$

$$d_{eff} = d_{31} sin\Theta - d_{22} cos\Theta sin3\phi \tag{1.3}$$

Here, Θ is the angle between the propagation vector and the optical axis, and ϕ is the azimuthal angle between the propagation vector and the xz crystalline plane (see Fig.1.5). The units for d_{eff} are pm/V and values for the specific three wave mixing interactions could be found in the literature, for example in [60] or taken from programs, calculating phase-matching conditions, such as SNLO [61]. For better performance of the amplification, crystals with higher d_{eff} for the selected process are preferred.

Nonlinear crystals in the MWIR

The choice of the right nonlinear crystal is important for attaining successful performance at the OPA stage. The most common, commercially available nonlinear crystals are: BBO, KTA, LBO, $LiNbO_3$ (bulk and periodically poled), AGS, AGSE, ZGP. The oxide crystals are limited for use in the near and short wave infrared and the longer wavelengths demand non-oxide crystals (see Fig.1.4). These crystals are more complicated to grow, thus the commercial availability and crystal quality might be lower than the conventionally used oxides in the short wave infrared [7]. As half of the crystals listed before were used in the experiments described in this thesis, it might be interesting to compare and discuss the particular interest to use one or another in a particular case.

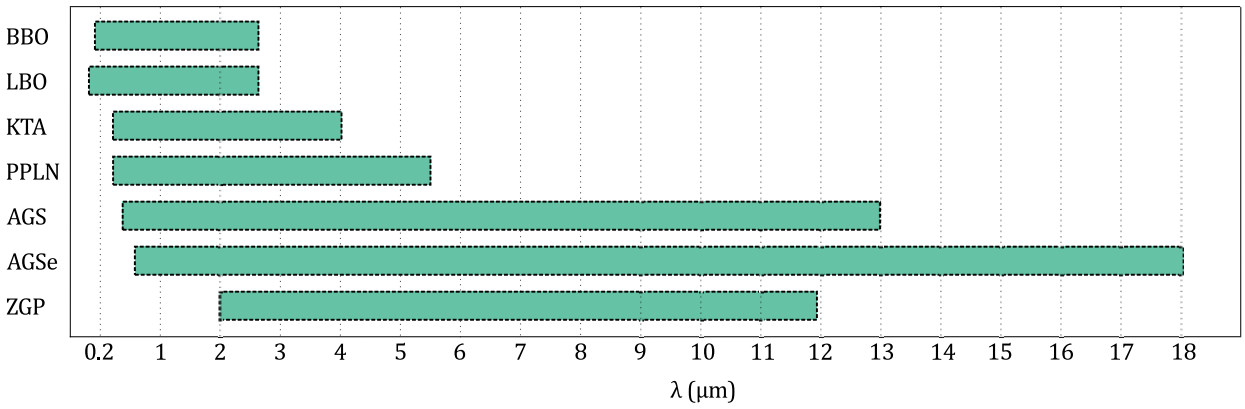

Figure 1.4 Transparency of nonlinear crystals in the MWIR.

BBO crystal is transparent in the region between 185 – 2600 nm, thus it is broadly used in the short wave infrared OPAs, but not suitable for longer wavelengths. Featuring a high damage threshold, well developed growing technique and reasonable d_{eff} (around 2 pm/V), it is the most commonly used crystal for the near infrared and short wavelength infrared systems which are also commercially available: OPA TOPAS [62] or OPCPA Venteon OPCPAS [63]. The non-collinear configuration at the magic angle provides ultrabroadband amplification at 800 nm, which is the key point of the OPCPA systems working in this region. As the crystal was well applied for the systems in the near infrared, when the demand of ultrashort pulses in the longer wavelengths appeared it was successfully adapted for short-wavelength infrared OPAs [64].

LBO crystal is similar to the BBO and is mostly used for the NIR OPAs [65, 66], as its transparency range is also limited at 2600 nm. Comparing with the BBO, it features broader phase-matching in the case of collinear amplification, thus a broadband-generated idler beam does not acquire the angular chirp and can be amplified in the following stages.

KTA transparency window extends further into the mid-wavelength infrared, the crystal is transparent up to 4000 nm, so it is an attractive alternative for the BBO crystal for use in a longer wavelength OPAs. The crystal features a high damage threshold, the d_{eff} is comparable to the BBO and is also about 2 pm/V. However, there are still challenges to overcome with the crystal growing technique – large aperture crystals feature strong inhomogeneities, which is a huge drawback for high intensity systems as it makes it difficult to maintain the good quality of the beam profile, as well as to reach reasonable amplification efficiencies.

$LiNbO_3$ – these crystals come in bulk or periodically poled as well as aperiodically or with a chirped period or fan out grating, in order to achieve the quasi-phasematching and increase the d_{eff}. These crystals are commonly doped with MgO in order to reduce the effects of photorefraction and blue-and-green-light induced infrared absorption (GRIIRA) [67] and significantly increase the optical damage threshold [68]. Due to the enhanced parasitic phase-matching, which is stronger in the PPLN, the GRIIRA effect induces beam distortions, which limits the power scaling in PPLN OPAs. Also the limited aperture size of the periodically poled crystals could prevent the use of PPLN for the booster amplifier stages and instead the bulk crystals are implemented for the last stage of the OPA set-up [69]. The transparency is extended up to 5500 nm.

AGS crystal is transparent up to 11 000 nm, which means that it is an attractive material to generate wavelengths in the long wavelength infrared (LWIR) region. The d_{eff} is also high and depending on the configuration could reach 8-15 pm/V. However, it is a semiconductor with the bandgap of 2.7 eV, which is a disadvantage for pumping the system with the near infrared pump lasers (Ti:Sapphire or lasers emitting closer to 1 μm). Multiphoton absorption could result in beam distortions and reduced efficiency of the amplification stage. The crystal also features a high nonlinear refractive index ($n_2 = 1.5\times10^{-14}$ cm^2/W) [70], which reduces the critical power needed for the self focusing process to take place, but the critical power could be increased by using longer pump wavelengths. So there are a few reasons to favor the longer wavelengths for the parametric interactions in this crystal. And indeed the AGS crystal is commonly used for the difference frequency generation between the signal and idler beams coming out of the short wave infrared OPAs, pumped with the near infrared lasers [71, 72].

AGSe - the crystal is similar to the AGS, but features a lower bandgap of 1.8 eV, thus the three photon absorption would influence the performance up to 2.07 μm, which makes 1 μm pump lasers more favorable to pump the OPAs for the DFG mixing in the AGSe. Also the crystal is transparent up to 18 μm and the d_{eff} is almost two times higher than in the AGS.

ZGP crystal features a very high nonlinear coefficient with a d_{eff} around 75 pm/V. However, the crystal is not transparent for wavelengths shorter than 2 μm. Thus, the crystal is usually used in the 2 μm laser pumped OPAs [73–75]. The ZGP crystal also features high damage threshold.

Choosing the right crystal for nonlinear interactions

As the key factor for the OPA stage is the nonlinear crystal, it is crucial to make the right choice of which crystal to use for the particular applications. First of all, the crystal must be transparent for all the interacting wavelengths - the absorption of the idler in the short wave infrared would prevent the amplification of the signal in the visible [8]. Then the crystal should have a high nonlinear coefficient d_{eff}, which allows us to achieve a high efficiency using shorter crystals. In order to evaluate the efficiency of nonlinear media, a figure of merit (FOM) could be used. FOM is expressed as d^2/n^3; refractive indices vary for different nonlinear crystals so they must also be taken into account in order to accurately evaluate the materials nonlinear response. Values for the most common crystals could be found in Table.1.1. If the OPA is operating in the femtosecond regime, then the group velocity mismatch (GVM) also plays an important role and could limit the interaction length between the three beams. It might cause problems if the non-collinear configuration is not feasible or the d_{eff} of the crystal is not sufficient to use short crystals. Also, in order to amplify or generate ultrashort pulses the crystal should support a broadband phase-matching. The damage threshold is one of the parameters limiting the achievable intensities, thus if one is aiming at amplification of intense ultrashort pulses, the crystal of choice should feature the high optical damage resistance. Even though, the laser induced damage threshold (LIDT) of the crystal could be high, it is equally important to pay attention to the LIDT of the coatings as usually it is lower than the crystal itself. A table, summarizing these parameters for the crystals discussed in the previous section, is provided below. Unfortunately, LIDT data is only available for long pulse durations and is expected to be higher for femtosecond pulses.

Table 1.1 Nonlinear crystal properties. d_{eff} is for interaction between 1030 nm pump and 3 μm signal, LIDT data for 1064 nm.

Crystal	**Transparency,** μm	d_{eff}**, pm/V**	**LIDT MW/**cm^2	**FOM** ($\times 10^{24}$)
BBO	0.185–2.6	1.8 (type I)	50 000 (1 ps)	0.7
LBO	0.16–2.6	no phasematching at 3 μm	19 000 (1.3 ns)	0.1
KTA	0.35–4	2 (type II)	500 (10 ns)	0.7
LiNbO3	0.33–5.5	4 (type I)	10 000 (6 ps)	1.4
AGS	0.5–13	14 (type II) 1800 nm + 2400 nm	10 (20 ns)	13
AGSe	0.71–18	28 (type I) 1800 nm + 2400 nm	25 (50 ns)	40
ZGP	0.74–12	78 (type I) 2000 nm + 6000 nm	60 (100 ns)	170

1.1 Critical Phase-matching

Phase-matching is an important parameter, which determines the efficiency of the amplification stage. The energy flow from the pump to signal and idler is optimized, when the $\Delta k = 0$. In the case of collinear configuration, the phase-matching condition could be written as [8]:

$$n_p\omega_p - n_s\omega_s - n_i\omega_i = 0 \tag{1.4}$$

Because $\omega_p = \omega_s + \omega_i$, thus $\omega_s = \omega_p - \omega_i$ the phase-matching condition could be rewritten to:

$$\begin{aligned} n_p\omega_p &= n_i\omega_i + n_s(\omega_p - \omega_i) \\ \omega_p(n_p - n_s) &= \omega_i(n_i - n_s) \end{aligned} \tag{1.5}$$

Here $\omega_i < \omega_s < \omega_p$ and if we assume that the process takes place in the isotropic medium with positive dispersion, or $n_i < n_s < n_p$ (or $n_i > n_s > n_p$ in the case of negative dispersion), which means, that in these cases the phase-matching condition cannot be satisfied, because $n_p - n_s > 0$ and $n_i - n_s < 0$. The solution for this would be the use of anisotropic materials, such as birefringent crystals. The birefringent crystals are crystals in which the refractive index depends on the polarization and propagation direction. There are two propagating modes – ordinary and extraordinary. For the ordinary beam the refractive index is a constant and does not depend on the propagation direction in the crystal. For the extraordinary beam, on the contrary, the refractive index depends on the propagation direction in the crystal. To

be more precise, the angle between the beam propagation direction and the crystal optical axis. This angle is called the phase-matching angle and could be found from the refractive index ellipsoid:

$$\frac{1}{n_e(\Theta)^2} = \frac{\cos^2(\Theta)}{n_o^2} + \frac{\sin^2(\Theta)}{n_e^2} \tag{1.6}$$

The graphical scheme of the index ellipsoid together with the ordinary and extraordinary directions are depicted in Fig.1.5 [8]. Here, the case of the positive uniaxial crystal is depicted. The crystal is called positive if $n_o < n_e$ and if $n_e < n_o$ it is negative. Depending on the pump beam polarization and it's relation with the other two waves the phase-matching could be divided into two types: type I and type II (see the summary of polarizations in Table 1.2).

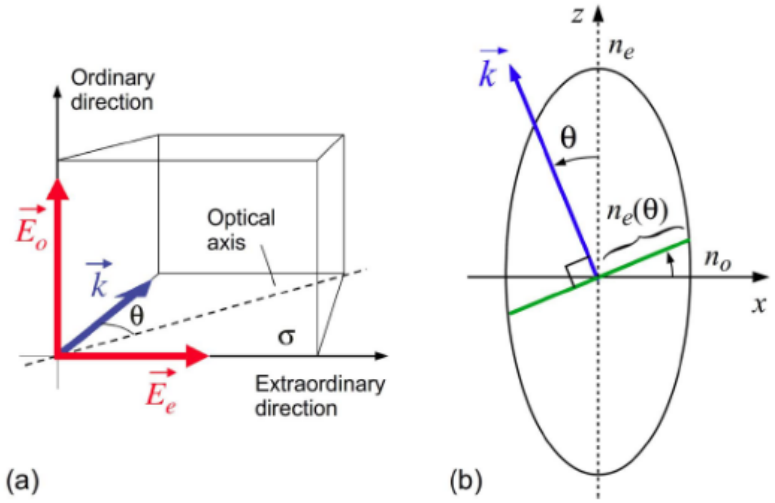

Figure 1.5 (a) ordinary and extraordinary directions in uniaxial birefringent crystals. (b) section of the index ellipsoid and graphical meaning of the extraordinary refractive index for a positive uniaxial crystal. The optical axis is in the z-direction. (Figure taken from [8])

Table 1.2 Summary of polarization configurations for positive and negative uniaxial crystals.

Phase-matching type	Positive Uniaxial, $n_o < n_e$	Negative Uniaxial, $n_e < n_o$
Type I	ee-o $n_p^o\omega_p = n_i^e\omega_i + n_s^e\omega_s$	oo-e $n_p^e\omega_p = n_i^o\omega_i + n_s^o\omega_s$
Type II	oe-o $n_p^o\omega_p = n_i^o\omega_i + n_s^e\omega_s$	eo-e $n_p^e\omega_p = n_i^e\omega_i + n_s^o\omega_s$

The phase-matching angles for different interactions can be found in [76].

Usually, a Sellmeier formula is used to calculate the wavelength-dependent refractive index. The general form of the formula is:

$$n^2(\lambda) = 1 + \sum \frac{A_j \lambda^2}{\lambda^2 - B_j} \tag{1.7}$$

Here, wavelength in the formula is in micrometers. The coefficients A_j and B_j are obtained from experimentally measured refractive indexes in the wavelength range of interest. Sellmeier expressions and coefficients for all commonly used crystals could be found in Nonlinear Optical Crystals: A Complete Survey by D. Nikogosyan [60].

There are different programs developed to calculate phase-matching such as spdcalc online calculator [77], NIST Phasematch [78] or SNLO [61]. However, one of the most popular ones is SNLO. It is a free software, which has a variety of functions helping us to choose the crystal for nonlinear interactions and simulating the performance. One of the features is the calculation of the phase-matching angle. In a table below, you can see the summary of parametric processes carried out in experiments described in this thesis, the corresponding crystals and phase-matching angles.

Table 1.3 Phase-matching angles for interactions experimentally done during thesis.

Crystal	**Interaction**	**Θ, deg**
BBO	515 nm + 700 nm –> 1950 nm type I	21.7
BBO	1030 nm + 2100 nm –> 2020 nm type I	21.3
KTA	1030 nm + 1570 nm –> 3000 nm type II	42
KTA	1030 nm + 1800 nm –> 2400 nm type II	45
AGS	1800 nm + 2400 nm –> 7140 nm type II	39

1.2 Non-critical phase-matching

Temperature Phase-matching

Phase-matching could be also achieved by changing the temperature of the nonlinear crystal. This is because the refractive index always has some temperature dependence. In the case, when the three interacting beams are aligned on a certain axis of the crystal phase-matching could be adjusted in such a way that phase velocities of the interacting beams are equal. The adjustment is done by changing the temperature in the crystal. Only crystals with a very strong temperature dependence are used to achieve this type of the phase-matching, for example Lithium Niobate (LN) or Lithium Triborate (LBO). One of the advantages of this type of phase-matching is that there is no walk off between the waves of different polarization (o and e), so smaller beams could be used to reach higher intensities. Also, interacting beams could be focused more tightly, because non-critical phase-matching is less impacted by the beam divergence. However, the drawback of using the temperature phase-matching is that the temperatures needed to fulfill the phase-matching conditions are much higher than the ambient temperature in the laboratory, which means that an oven must be used and measures to ensure careful and gradual warming up and cooling down should be taken. On the other hand, when the required temperature is achieved, the process is stable and not impacted by the room temperature fluctuations.

Quasi-phase-matching

It is not always possible to achieve efficient phase-matching based on a material's birefringence. This is the case in the shorter wavelength region where the refractive index is changing fast with the wavelength, but the birefringence (the difference between ordinary and extraordinary refractive indexes) stays nearly constant. Thus the birefringence is not sufficient to compensate for the dispersion of the refractive indexes. Another example, where the critical phase-matching cannot be achieved is when a particular index of nonlinear coefficient d_{eff} needs to be accessed, for example d_{33}. It requires all three beams to have the same polarization, thus the critical phase-matching conditions cannot be satisfied. However, there is a way to achieve phase-matching in the materials, where the phase mismatch is too high to operate in the critical phase-matching regime.

The parametric process is considered to be efficient as long as the phase mismatch is smaller than $\pi/2$. The crystal length, where the process is efficient is called the coherence length and is defined as:

$$L_{coh} = \frac{2}{|\Delta k|} \tag{1.8}$$

If the mismatch is high, then the coherent length could be as short as 10 μm. If one could obtain the mismatch at a distance longer than the L_c, then the parametric process could take place and phase-matching could be achieved. This is possible and the method is called quasi-phase-matching. Quasi-phase-matching is based on the periodic inversion of the optical axis along the crystal length. The schematic view of the homogenous and periodically poled crystals as shown in Fig.1.6. The crystal axis is inverted by 180 degrees, with the inversion period equal to the doubled coherence length. And the phase-matching condition, where Λ is the period of crystal axis inversion is written as:

$$\Delta k = k_1 + k_2 - k_3 - \frac{m2\pi}{\Lambda} \tag{1.9}$$

The axis inversion results in the inversion of the sign of the nonlinear coefficient and compensates for the vector mismatch. The amplitude of the generated wave grows at the distance L_c, then the optical axis reverses and the phase of the wave continues to change, but in the other direction. Thus, the process continues and the amplitude of the generated wave grows (Fig.1.7 (b)). In the case of perfect phase-matching (Fig.1.7 (a)), the amplitude of the generated wave grows linearly with the propagation distance in the nonlinear crystal. When the wave vector mismatch is high (Fig.1.7 (c)), then the amplitude of the generated wave is periodically oscillating between the generation and the back-conversion modes. And finally, in the case of quasi-phase-matching the amplitude of the generated wave is growing with the propagation distance, but slower than in the perfect phase-matching process. So, if the d_{eff} is the same for perfect phase-matching and quasi-phase-matching, then the efficiency of the quasi-phase-matched process will be lower by the factor of $2/\pi$. But usually quasi-phase-matching allows us to use the higher d_{eff}, which could significantly increase the efficiency. The birefringence phase-matched interaction in bulk LN crystal has the d_{eff} value of ~ 4 pm/V, while the periodically poled LN has the d_{eff} of ~ 25 pm/V. Signals generated in the PPLN crystal are expected to be 40 times stronger than in the same length of bulk-LN.

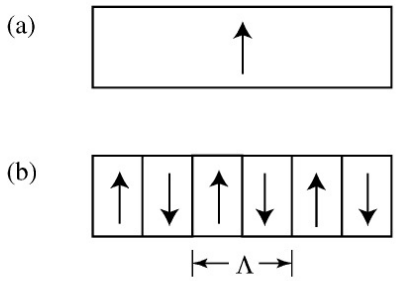

Figure 1.6 Schematic view of bulk (a) and periodically poled (b) crystals. In (b) the crystal axis is inverted with the period Λ. (Figure is taken from [9].)

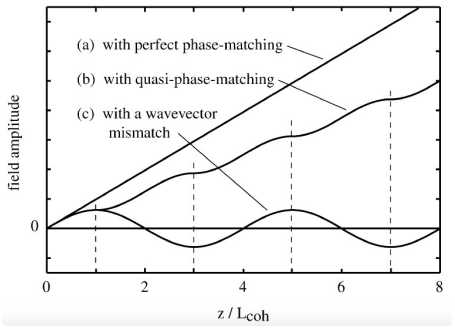

Figure 1.7 Field amplitude growth as a function of propagation distance in the case of perfect phase-matching, quasi-phase-matching and the vector mismatch. Figure is taken from [9].

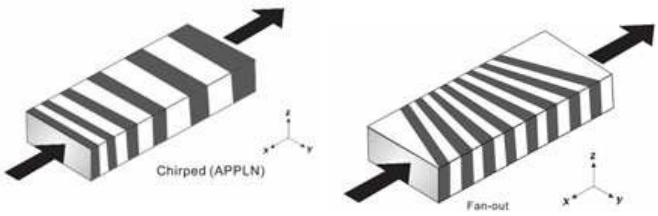

Figure 1.8 The schematic view of an aperiodically poled crystal with the negative poling chirp (left) and fan-out crystal (right). (Picture is taken from [10].)

The amplification bandwidth at 3.6 μm is 300 nm in the PPLN crystal [79]. However, it could be improved if the poling period is aperiodic (chirped). The chirped period allows us to phase-match all the wavelengths of interest and the spectral gain is inversely proportional to the chirp rate. Furthermore, if the fan out structure (see the bottom figure of Fig. 1.8) is applied, phase-matching can be adjusted by translating the crystal through different chirp zones. However, at the output of the crystal, the amplified beam acquires spatial chirp as the phase-matching is different along the beam profile. On the other hand, fan out structure has advantages to be used in FOPA, where beam is spatially dispersed and thus different wavelengths are amplified at different spots in the crystal. Initially, FOPA set up was based on multiple nonlinear crystals [6], but later a fan-out PPLN was introduced [80]. The use of fan out PPLN solves a few drawbacks initially present in the multi-crystal set up: optical path introduced in each crystal should be precisely matched, which becomes more and more complicated with the increase of the number of crystals used. Also there could be pre-pulses

generated due to the diffraction on the edges of the crystals.

To sum up, the main advantages of the quasi-phase-matching are [67]:

- The crystal could be designed to feature phase-matching for a certain process all over the crystal's transmission range;
- It is possible to employ the highest nonlinear coefficient (d_{eff}), which might lie on the diagonal of the susceptibility tensor and need to have all the interacting waves of the same polarization, thus impossible to use in critical phase-matching;
- The Poynting vector walk-off could be eliminated and the angular acceptance increased by propagating all the three beams along the optical axis of the crystal.
- the amplification bandwidth could be improved by implementing an aperiodic poling period, where the amplification takes place for each spectral component as long as the phase mismatch is not too high, or the pump beam will get depleted [79]. Furthermore, if the poling featured the fan out structure, the broadband spectrum could be tuned.

Amplification of ultrashort pulses: non-collinear phase-matching

In the case of ultrashort pulse amplification, the approximation of monochromatic waves cannot be applied anymore. We should take into account the spectral bandwidth, spectral phase, group velocity, and other concepts of short pulses.

In order to generate short pulses, the spectral bandwidth of our pulses should be larger, the relationship between these two parameters for Gaussian transform limited pulses is expressed as:

$$\Delta\nu \times \Delta t_p = 0.44 \tag{1.10}$$

Here t_p is pulse duration and ν is spectral bandwidth in frequency range. Thus, the broader pulse spectrum is the potentially shorter pulses could be generated.

Because pulses are propagating in the nonlinear crystal with different group velocities (the velocities at which the envelope of a pulse propagates in the medium), after a certain distance the pulses will not overlap in the crystal anymore. This distance could be expressed as:

$$L_v = \left| \frac{t_p}{\frac{1}{v_{gp}} - \frac{1}{v_{g(s/i)}}} \right| \tag{1.11}$$

Here t_p is the pulse duration and v_g is the group velocity of pump, signal or idler pulses. Thus the interaction length for shorter pulses is shorter and could limit the amplification efficiency of the amplification stage.

The amplification bandwidth is defined as [11]:

$$\Delta\nu \cong \frac{2(\ln 2)^{1/2}}{\pi}\left(\frac{\Gamma}{L}\right)^{1/2}\frac{1}{|\frac{1}{v_{gs}}-\frac{1}{v_{gi}}|} \tag{1.12}$$

Here v_{gs} and v_{gi} is the group velocity of signal and idler waves, Γ is a nonlinear coefficient and L is the crystal length. The amplification bandwidth is maximized when the group velocity mismatch (GVM) is minimized between the signal and idler pulses.

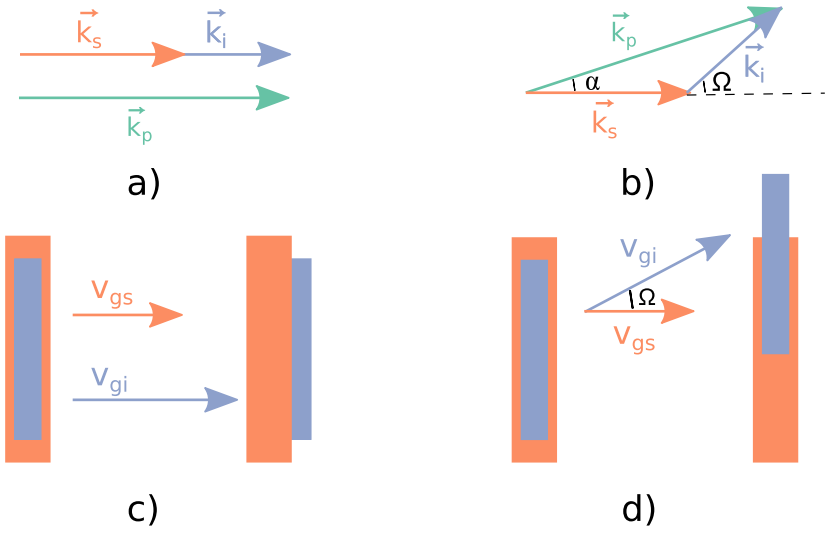

Figure 1.9 (a) Schematic k vectors of a collinear interaction geometry; (b) schematic k vectors of a non-collinear interaction geometry; (c) representation of signal and idler pulses in the case of collinear interaction; and (d) representation of signal and idler pulses in the case of non-collinear interaction. Here k denotes k vectors and v_g is group velocity; indices p, s, and i are for pump, singal, and idler (Picture adapted from [11].)

It is important to note that the GVM between the pump and amplified signal pulses limits the interaction length and the GVM between the signal and idler pulses limits the amplification bandwidth. Nevertheless, these limitations can be overcome by applying the non-collinear configuration to intersect the three beams in the crystal. In the case of collinear geometry, the signal and idler pulses get quickly separated in time, but in the case of the non-collinear geometry, pulses stay overlapped in time and are just transversely shifted and

not perfectly overlapping in space. The schematic geometry is depicted in Fig.1.9. In this case the phase-matching condition becomes vectorial and can be written as:

$$\begin{aligned} \Delta k_{\parallel} &= k_p \cos(\alpha) - k_s - k_i \cos(\Omega) = 0 \\ \Delta k_{\perp} &= k_p \sin(\alpha) - k_i \sin(\Omega) = 0 \end{aligned} \tag{1.13}$$

α is the angle between the pump and signal vectors and Ω is the angle between the signal and idler vectors. In order to obtain a broadband phase-matching, both $\Delta k_{\parallel}$ and $\Delta k_{\perp}$ should be equal to 0. After taking into the consideration the fact that the angle between signal and idler is not fixed and depends on the signal wavelength (if the signal increases by $\Delta\omega$, then the idler decreases by $\Delta\omega$) we get:

$$v_{gs} = v_{gi} \cos(\Omega) \tag{1.14}$$

Thus, the broadband phase-matching can be achieved at a certain angle Ω between the signal and idler beams, where the signal group velocity projection is equal to the idler group velocity projection along the signal direction. Equation 1.14 could be satisfied just when $v_{gi} > v_{gs}$, which is the case for all negative uniaxial crystals for the type I interactions. However, practically it is difficult to operate the angle between the generated idler and signal beams; it is much more convenient to know the angle between the input signal and pump beams. This angle is sometimes called the magic angle and could be written as:

$$\alpha = \arcsin\left(\frac{1 - \frac{v_{gs}^2}{v_{gi}^2}}{1 + \frac{2 v_{gs} n_s \lambda_i}{v_{gi} n_i \lambda_s} + \frac{n_s^2 \lambda_i^2}{n_i^2 \lambda_s^2}}\right)^{1/2} \tag{1.15}$$

1.3 Seed generation: white light continuum

White light continuum (WLC) is a third order nonlinear process, where the spectrum of narrowband ultrashort intense pulse gets broadened hundreds or thousands of times, while propagating in a dielectric medium. It is a key process for generating the seed for ultrashort optical parametric amplifiers. The supercontinuum generation was first observed in the 70's and because the process is complex it is still being investigated [81, 82]. The main factors contributing to the WLC generation are self phase modulation, cross-phase modulation, 4-wave mixing, Raman scattering, filamentation, self-focusing, and self-defocusing. The process can take place in different media, but bulk materials are the most suitable for stable everyday performance and provide smooth spectrum characteristics as well as high temporal

and spatial coherence [83].

The threshold for WLC generation is defined the same way as the critical power for self-focusing as this is the required process, which leads to different nonlinear effects stimulated by the increased intensity. When a intense pulse propagates trough a material it can change it's properties in a way that it acts as a lens. The sign of a formed lens depends on the nonlinear refractive index (n_2) of the material. In order to get the self-focusing, the (n_2) must be >0. The critical power is given by [84]:

$$P_{cr} = \frac{0.15\lambda_0^2}{n_o n_2} \tag{1.16}$$

here λ_0 is the wavelength of the pump laser, n_o – linear refractive index and n_2 – nonlinear refractive index, which is a parameter quantifying the nonlinearity of the medium. One could note that the process does not depend on the beam intensity, but the peak power. A critical power of self-focusing for some of the most commonly used materials for 800 nm and 1030 nm pump wavelengths is depicted in Fig.1.10 [12] and is in the range of few MW.

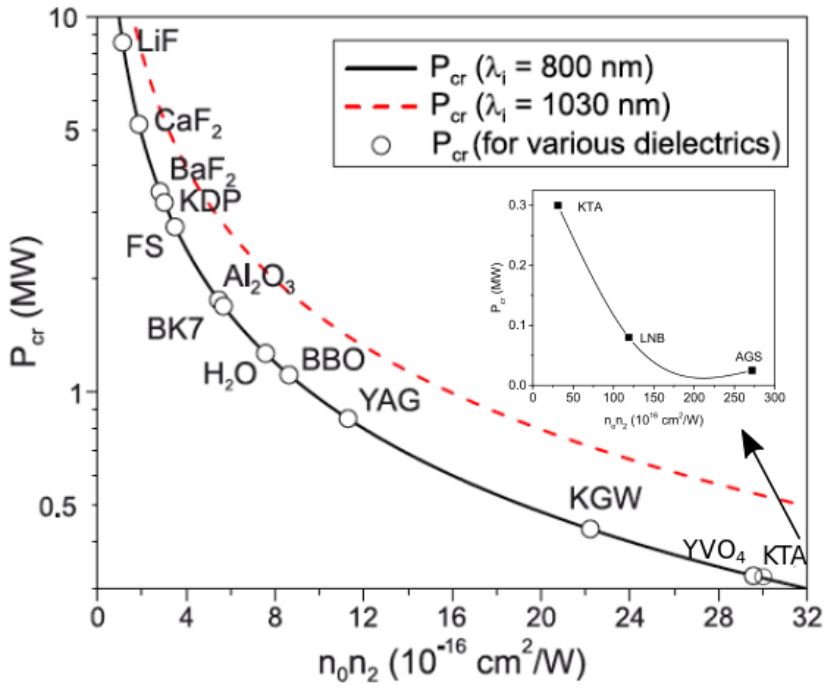

Figure 1.10 Calculated critical power for 800 nm and 1030 nm pump wavelengths. The circles show the values for different materials pumped with 800 nm laser. (Figure adapted from [12].)

Spectral broadening was also studied in [85] and the results showed that broadening to the blue wavelengths side is much stronger than into the red side. Furthermore, the continuum generation depends on the material band gap energy (E_g) and the strongest broadening into the shorter wavelengths is observed in materials with the highest E_g. Materials with the highest band gap energy are also the materials with the lowest nonlinear refractive index, as the relationship between these two parameters is inversely proportional to the E_g^4 [86]. The WLC generation under different conditions in YAG and sapphire was done in [82], and the study reveals that YAG crystal is a better material for WLC generation, while pumped with a NIR laser, as it provides smoother, more stable and more energetic spectrum in both sides of the broadening. Also, a longer crystal further improves the stability and robustness of the system. The latter was also observed in our experiments, as shifting from a 4 mm YAG plate to a 15 mm rod significantly improved the stability, generated more energetic spectrum and the most importantly, the red side of the continuum spectrum spread up to 2-2.4 μm, which simplifies the set up of the OPAs in the MWIR. As it is shown in Fig.1.11, the continuum spectrum extends up to 2.4 μm (the detection of longer wavelengths was limited by the spectrometer (Nirquest 256 from Ocean Optics). The amplified signal is provided in Fig.1.12 and shows the tunability over the whole range of interest (up to 2 μm, where the degeneracy takes place). The efficiency and the spectrum width here depend on the crystal and the phase-matching conditions used in the particular configuration, thus could be optimized for the targeted spectral region.

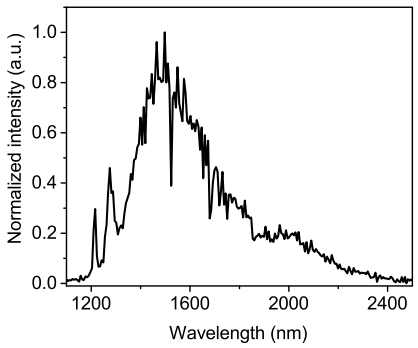

Figure 1.11 Spectrum of WLC generated in 15 mm YAG. Parameters of the driving laser: 1030nm, 380 fs, 220 mW, 100 kHz.

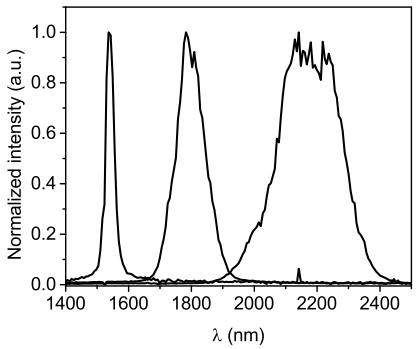

Figure 1.12 Amplified WLC spectrum from Fig.1.11, by tuning the phasematching angle, we reach amplification at the degeneracy wavelengths. Amplified spectra are individually normalized.

1.4 Dispersion and pulse compression in the mid-wavelength infrared

After the pulse has been amplified in the crystal and passed through all the optical components in the system, it accumulates the spectral phase, which has to be compensated for to achieve the shortest possible pulse duration – preferably the transform-limited pulse duration. As for most of the ultrashort OPAs, the seed signal is generated via white light continuum generation. The broadband output usually corresponds to positively chirped pulses. The spectral phase for the signal pulses should be compensated for by using materials with negative dispersion. However, in the SWIR and MWIR regions, the negatively chirped idler pulses are the main output. The pulses with the negative chirp should be compressed with the materials featuring a positive dispersion. Additionally, it could occur that even the idler pulses exit with a positive chirp due to the propagation through different optical elements with the positive dispersion in the system or the signal was purposely stretched to obtain the negative chirp.

The common methods for pulse compression are the use of grating pairs, prism pairs, chirped mirrors, bulk materials and adaptive optical systems. For the compression of pulses in the mid-wavelength infrared, the most common way is just to simply use the bulk materials [87] as the method is cost effective and the implementation is simple. However, there are some systems with grating compressors [88] and acousto-optic modulators to correct the accumulated spectral phase [89]. The grating compressors feature negative dispersion, so as in the case of OPCPA in [88], the signal was also stretched by a grating pair which induced positive dispersion to the generated idler beam. It was then possible to use the grating pair for the idler compression. Also, high efficiency gratings have a very high cost and potentially lead to the loss of up to 20% of the signal at the end of the system. The technology of chirped mirrors is well matured in the near infrared spectral region. However, there is still a lack of commercially available products for the spectral range around 3 μm (at the moment of the writing the manuscript just one company (Ultrafast Innovations) was found providing chirped mirrors at this spectral region). Thus, as aforementioned, bulk materials are mostly considered for the pulse compression in the mid-wavelength infrared. Nevertheless, even if it looks simple, a few considerations should be addressed:

- Semiconductor materials, such as germanium or silica feature a high nonlinear coefficient, which results into the low input threshold for the self focusing and beam

distortions. So one has to be careful, when choosing the right material for the post-compression of intense MWIR pulses.

- Bulk materials can not compensate for the third order dispersion, which is always positive in the transmission range of the glasses [87]. Thus it could be the limiting factor in achieving the transform-limited pulse durations.

The summary of commonly used materials and their group delay dispersion (GDD) at different wavelengths, which were used during experiments described in this thesis, is provided in the Table 1.4.

Table 1.4 GVD and TOD of commonly used materials for the pulse compression in the mid-wavelength infrared. Data is provided for 1.03 µm, 1.5 µm, 2 µm and 3 µm.

Material	GVD, fs^2/mm 1.03 µm	TOD fs^3/mm 1.03 µm	GVD, fs^2/mm 1.5 µm	TOD fs^3/mm 1.5 µm
YAG	65	65	15	145
Ge	-	-	-	-
ZnSe	660	545	400	390
CaF_2	20	20	45	-20
BBO	45	60	-1	150
KTA	-5	25	-30	90
$LiNbO_3$	290	255	125	365
Sapphire	30	60	-25	175
Si	-	-	1175	1225
Material	GVD, fs^2/mm 2 µm	TOD fs^3/mm 2 µm	GVD, fs^2/mm 3 µm	TOD fs^3/mm 3 µm
YAG	-60	385	-360	2180
Ge	-	-	1525	3170
ZnSe	280	365	160	440
CaF_2	-20	120	-105	585
BBO	-110	825	-	-
KTA	-80	275	-290	1445
$LiNbO_3$	-35	790	-595	3875
Sapphire	-120	530	-550	3160
Si	810	840	520	820

1.5 Carrier envelope offset stabilization

The stability of the carrier envelope offset (CEP) has a high importance for the experiments requiring ultrashort pulses with few cycle pulse duration. CEP is the offset between the opti-

cal phase and the maximum of the wave envelope of an optical pulse. As was demonstrated in [90], the generated high harmonic signal changes by tuning the CEP. The CEP tuning corresponding to the envelope phase is depicted in Fig. 1.13: the initial pulse has the carrier envelope offset equal to zero, afterwards the CEP is shifted to $\pi/2$ and lastly to π.

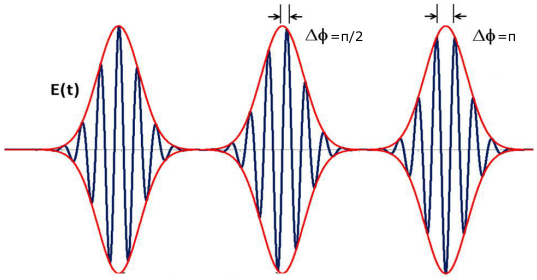

Figure 1.13 The CEP tuning from $\Delta\phi = 0$ to $\Delta\phi = \pi$. (Modified figure from [13])

CEP could be actively or passively stabilized. Active stabilization includes different configurations and implementations of feedback loops. Passive CEP stabilization is achieved in the OPA by generating the idler beam from the same laser-frequency-driven seed generation and pump beams.

In the Table 1.5 [91] a summary of the phase properties in three different OPA configurations is provided. For A and C configurations, the OPA pump and the white light are sharing the same frequency. In the case of A, it is the fundamental frequency, and in the case of C it is the generated second harmonic. In both cases the passive stabilization of the idler pulses is achieved. However, in B configuration the white light continuum generated from the fundamental frequency of the pump laser is amplified by the second harmonic pump, which leads to un-stabilized idler pulses. Thus, at least one additional parametric stage is needed to achieve the passive CEP stabilization. This could be done by amplifying the idler beam with the fundamental beam and generating the passively stabilized idler, as it was done in [65].

Table 1.5 Phase properties of various OPA designs.

OPA configuration	A	B	C
Pump frequency, ω_p	ω_0	$2\omega_0$	$2\omega_0$
Central frequency of the white light, ω_p	ω_0	ω_0	$2\omega_0$
Phase offset of pump,Φ_p	Φ	$2\Phi+\pi/2$	$2\Phi+\pi/2$
Phase offset of signal,Φ_s	$\Phi+\pi/2$	$\Phi+\pi/2$	$2\Phi+\pi$
Phase offset of idler,Φ_i	$-\pi$	$\Phi-\pi/2$	$-\pi$
Self stabilization?	Yes	No	Yes

The CEP stability could be measured by recording the spectral interference between the white light continuum and the generated second harmonic signal [92]:

$$I(\omega) \propto I_F(\omega) + I_{SH}(\omega) + 2[I_F(\omega) I_{SH}(\omega)]^{1/2} \cos(\omega\tau_d + \Theta_0 + \pi/2) \tag{1.17}$$

Here $I(\omega)$ is the spectral interference signal and I_F is the signal of the fundamental frequency and I_{SH} of the second harmonics, the $\omega\tau_d$ is the delay between the two pulses and Θ_0 the phase, thus the spectral interference signal is a function of Θ_0 at the constant $\omega\tau_d$. The signal does not depend on the intensity fluctuations, because it is the position of the interference fringes, which holds the information about the CEP. In fact, this is not true for the real experimental conditions. When the OPA is unstable, the filament is generated at different longitudinal positions in the media, which introduces an additional phase noise. If the pump laser or OPA is very unstable, a reliable f-2f CEP stability measurement cannot be performed [65].

The CEP shift after propagating in the dispersive media of the thickness d depends on the difference between the phase and group refractive indexes [93]:

$$\Delta_{CE} = \frac{\omega}{c}(n_g - n)d \tag{1.18}$$

Here n_g is the group refractive index. Afterwards one can estimate the material length to be inserted to change the CEP by 2π and thus control the CEP position.

The classical experimental set up of the f-2f interferometer is depicted in Fig.1.14. Firstly, the white light continuum is generated. Usually it is done in a piece of YAG, Sapphire or an other common bulk material. However, the spectral broadening could also be achieved in a hollow core fiber filled with gas [92, 94], where broadening can be controlled by changing the gas pressure. Then, the second harmonic of the signal is generated in a nonlinear crystal.

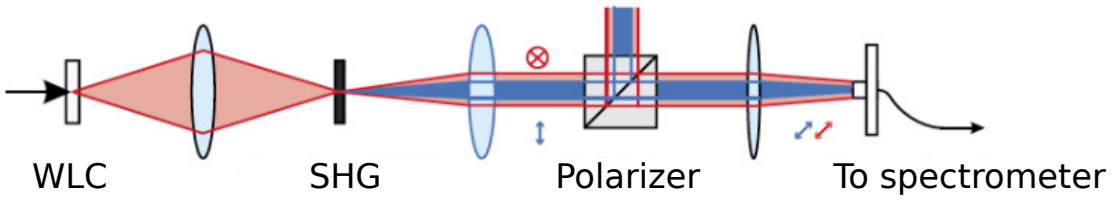

Figure 1.14 The f-2f interferometer. WLC- white light continuum, SHG - second harmonic generation stage; arrows indicate the polarization direction. (Modified figure from [14])

Since type I phase-matching is realized, the continuum pulses and the second harmonic pulses hold perpendicular polarizations. In order to have interference between the two signals, they should go through the polarizer set at 45 degrees, so a fraction of both beams with the same polarization is selected and sent to the spectrometer. It is important to note that this is an inline configuration and the delay between the two pulses arriving at the spectrometer should not be longer that the coherence length:

$$L_c = \frac{c}{\Delta\nu} \tag{1.19}$$

Here $\Delta\nu$ is the bandwidth of the pulse spectrum. In such a configuration, the delay between the two pulses and the inter-fringe period can be adjusted by inserting additional material in the beam path between the white light continuum generation and the second harmonic generation stages. If this is not feasible, a classical interferometer with two branches and a delay line should be implemented.

For the successful implementation of this method it is important to generate an octave spanning white light continuum and use a spectrometer with a resolution compatible with the inter-fringe period. However, when the WLC generation is driven by a MWIR source, this is a challenging task. The signal tends to drop significantly in the region covering the SH wavelength region. One of the solutions would be to phase-match the second harmonic generation of the generated supercontinuum for the regions, where the WLC signal is sufficient to measure the interference [95, 14]. It is also possible to generate the SH signal first and then use it as a pump for the f-2f interferometer, in this case, the measured CEP instabilities would be twice as high as from the original pulses in the mid-wavelength infrared.

1.6 High power systems: thermal effects and damage threshold

Parametric sources, contrary to laser sources, do not require population inversion (and thus the energy storage) which significantly reduces the crystal heat load. This is important, when operating high power systems. If, at high average power, the crystal has absorption for one of the three wavelengths, the temperature of the crystal would increase. The non-homogenous heating would result in a spatial temperature gradient as well as the refractive index changes. Even at a relatively low OPA output power of 2 W, the temperature in the crystal increases by 50 K [96] and the temperature difference reaches 150 K, when the repetition rate is increased from 150 kHz to 1 MHz with the output of the OPA of 14 W. The varying refractive index induces varying phase-matching conditions and this limits the achievable amplification gain as well as inducing the gain narrowing and beam profile distortions. Furthermore, the crystal may break due to thermally induced stress (see Fig.1.16).

Thermal properties of borate crystals were investigated in [97]. As most of the high power pump lasers are based on Yb doped laser technologies, pump wavelengths are either 1030 nm, or the second harmonic wavelength at 515 nm. If the broadband OPA is operating at 800 nm, then the process is pumped by the SH beam and this would make the most impact to the thermal heat load in the crystal. However, as mentioned earlier, one has to be careful while choosing the signal and idler wavelengths. If the OPA is based on borate crystals, then the signal wavelengths must be limited to be higher than 700 nm, otherwise the generated idler beam will be longer than 1950 nm and will get absorbed. The same applies for the generated parametric superfluorescence, which lies within the same wavelength range as signal and idler beams, thus stronger signal and lower pump intensities as well as both pulses well matched in time and space are recommended. The input of the pump absorption in the protective coating also plays a significant role: by removing the coating the temperature increase could be reduced by 25 % [96], but in that case the Fresnel reflection should be taken into account, or the crystal should be cut at the Brewster angle. However, in the type I phase-matching configuration, the signal beam featuring perpendicular polarization to the pump would still experience losses.

One of the parameters that determines the amplification gain in the nonlinear crystal is the intensity of the pump beam, which is limited by the laser-induced damage threshold of the crystal, or more commonly by the damage threshold of the coatings of the crystal, which usually feature a lower damage threshold. Sometimes, if the losses due to the reflections are

significantly over-compensated by the amplification, it could be preferable to use uncoated crystals, which, as mentioned before, also improves the crystal's ability to handle the high average power. However, this applies only to the crystals with a small refractive index, otherwise the transmission of the crystal without the antireflective coatings for the pump could be just 50% [98]. Commonly, crystals transparent in the mid-wavelength infrared region have a high reflective index and good quality coatings are important for the successful implementation of the crystal.

The mechanism for the LIDT process depends on the laser wavelength and pulse duration. The damage threshold scales with the pulse duration as a squared root of the ratio between the actual pulse length over the pulse length of the known value of the LIDT [99]. However this is valid only for pulse durations longer than 10 ps. For the ultrashort pulses, the damage mechanism is more complicated and the scaling law in the femtosecond regime was suggested to depend on the pulse duration with the power of factor k ($F_{th} \sim t^k$), which is not dependent on the material or pulse duration and is equal to 0.30 ± 0.03[100].

Technology of ultrashort pulse OPAs in the near and short wave infrared has already matured, but the crystal providers still provide the damaged threshold mostly in the ns regimes. Even though sometimes publications include the beam intensities in the crystals the reported numbers could be impressively high or not measured using the certified ISO standards. A BBO crystal was reported to be able to handle 1.9 TW/cm^2 of the pump beam at 1030 nm and the pulse duration of 580 fs [64]. The reported values of LIDT for longer pulses at 1064 nm in BBO crystals are: 0.5 GW/cm^2 at 10 ns and 50 GW/cm^2 at 1 ps [101]. Different types (blank LN, doped with 5% MgO, PPLN) of lithium niobate crystals were tested in [102]. R-on-1 method was used for the laser pulses with a pulse duration of 1 ps at 1030 nm at two different repetition rates of 10 kHz and 100 kHz. R-on-1 method is performed as following [103]: the surface is divided into a number of sites and each site is irradiated with a number of laser pulses with the same fluence. The laser fluence on site is increased until the damage of the site is reached. The damage probability is determined from one site, however multiple sites are used for statistical evaluations. The results show that the damage threshold is indeed slightly higher for uncoated samples and lower repetition rates. The crystal doping with Mg:O slightly increases the damage threshold and the PPLN samples feature 1.7 times lower LIDT compared to the bulk Mg:O doped crystals at the lower repetition rate. At 100 kHz the difference is smaller – 1.5 times, but still could be a limiting factor for the power scaling in PPLN OPAs in the high power regimes.

It could be hard to estimate the LIDT for ultrashort pulses, because there is no complete study for the ultrashort pulse regime and the wavelength and pulse duration scaling is not straightforward. The damage threshold was experimentally measured in a few commonly used crystals: BBO, $LiNbO_3$ and LGT, (which is a new nonlinear crystal with the promising parameters for a broadband phase-matching in MWIR, while pumping with the source at 967 nm). The measurements took place in Laboratoire Lasers, Plasmas et Procedes Photoniques (LP3) at university of Marseille and were conducted by dr. Jean-Christophe Delagnes within the collaboration with the local group.

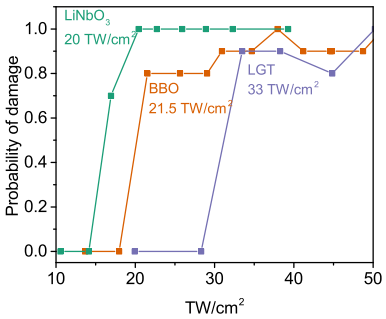

Figure 1.15 Laser induced damage threshold probability for BBO, $LiNbO_3$ and LGT crystals.

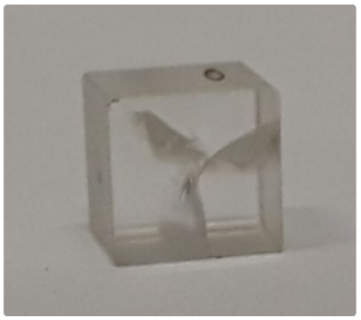

Figure 1.16 Cracked 5 mm BBO crystal due to thermally induced stress.

The method of 1-on-1 was used and the available laser source was the Ti:Sapphire laser with a pulse duration of 15 fs. 1-on-1 test is performed as following [103]: the surface is divided into a matrix of sites, which are well separated. A laser pulse with a certain energy is irradiating a number of sites with one pulse per site and the state (damaged/not damaged) of the site is recorded, the probability of damage is calculated. Then the pulse energy is increased and the steps are repeated till a 100 % of damage is reached. $LiNbO_3$ and LGT crystals were not coated and the BBO had a anti-reflecting coating for the pump at 1030 nm and signal/idler pulses at 2 µm. The measured damage threshold values are: 20 TW/cm^2 for $LiNbO_3$, 21.5 TW/cm^2 for BBO and 33 TW/cm^2 for LGT crystal. It is hard to directly compare the results with the LIDT values at longer pulses, mostly because the measurements are reported at longer wavelengths: 1030 nm or 1064 nm, however a linear dependence of LIDT on the wavelength is expected [104]. LIDT for $LiNbO_3$ is 3 times lower compared to the value reported at 1 ps, 0.3 J/cm^2 and 1.05 J/cm^2. This could be due to the poor crystal quality, because the attempt to obtain the efficient parametric amplification was not successful in this crystal sample. However, the LIDT in BBO at 15 fs is 20 TW/cm^2, which is 660 times

higher than at 1 ps pulse duration (50 GW/cm^2).

Chapter 2

High repetition rate OPAs in SWIR and MWIR

The experiments described in this chapter took place in CELIA laboratory at University of Bordeaux. The study of two OPAs are presented: the first one is operating at 2 µm and the second one at 3 µm. Also a new nonlinear crystal (LGT) was tested and implemented into both systems. The pump laser for these systems is a high power Yb:FCPA laser Solstice: 100 kHz, 380 fs, 1030 nm, up to 370 µJ. The OPAs were built in order to use them to drive experiments of HHG in gas and/or solids. However only 3 µm OPA was successfully used to generate HHG in ZnSe.

2.1 Yb:FCPA pump laser "Solstice"

The OPAs, presented in this chapter are pumped by Ytterbium (Yb) doped fiber chirped pulse amplifier (FCPA) [15, 105], built in-house.

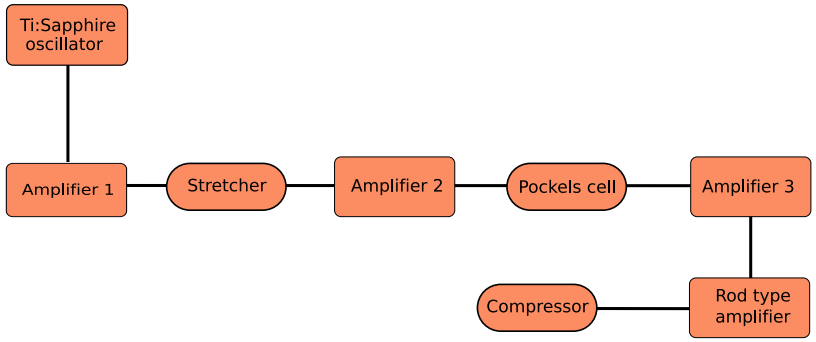

Figure 2.1 The pump source for the OPA experiments - FCPA "Solstice" [15].

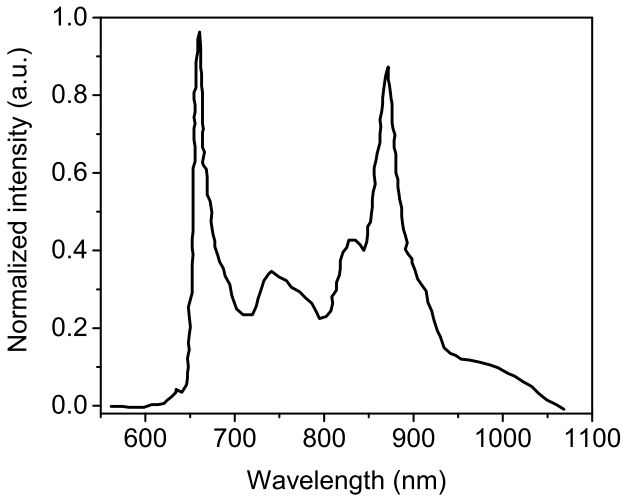

Figure 2.2 Broadband spectrum of Ti:Sapphire oscillator "Rainbow". Spectral part around 1030 nm is used to seed the Yb:FCPA.

The seed source for the Ytterbium doped fiber amplifiers is a Ti:Sapphire oscillator "Rainbow" (Femtolasers) with a broad spectrum spreading from 650 nm to 1050 nm (see Fig.2.2). This laser has a CEP stabilization and works at 77 MHz repetition rate, and the output power is 180 mW. The spectral part at 1030 nm with the power of 1 mW is selected to seed the first amplifier. All the fiber amplifiers are pumped by diode lasers at 976 nm. The first three amplifiers consist of the same type of fiber – an Yb doped fiber with a core size of 40 μm. Firstly, pulses are amplified up to 300 mW, which is the required power level to pass through the stretcher, so that there is enough energy left to seed the second amplifier and reduce the level of amplified spontaneous emission (ASE). The femtosecond output of the first amplifier is stretched up to 3 ns in an Öffner type stretcher based on transmission gratings. Pulses propagate through the stretcher twice and the transmission efficiency is 57 %. Pulses are amplified further in a second amplifier, where the power reaches 1 W. After passing through the Pockels cell, the repetition rate is reduced to 100 kHz. Then the pulses are amplified in the third amplifier, where the output power reaches 1 W. The output of the third amplifier is then divided into two equal parts and is sent into the final all-silica double-clad large-mode-area rod type fiber amplifiers (fiber core diameter is 80 μm, inner clad diameter is 200 μm, core numerical aperture NA=0.02). The pulse duration after amplification in the rod is 1.5 ns: it is reduced, compared to the stretched pulses, due to the gain narrowing in the amplifiers. The seed for the amplifiers features a spectral bandwidth of 20 nm and the system output is 7 nm at Full Width Half Maximum (FWHM) signal level. The output spectrum is provided in Fig.2.4. After the amplification in the rod, the pulses are

compressed down to 350-380 fs. The autocorrelation of the pulse is depicted in Fig.2.3. The pulse duration was 380 fs and later was improved to 350 fs. The efficiency of the compressor is 90 %. The initial output power was 50 W [15], but then the threshold for transverse mode beating decreased due to the fiber aging. The mode beating appears at a certain laser output power. These fluctuations are caused by a constant energy transfer between the fundamental and higher order modes [106]. In all the experiments described in this thesis, only one rod was used, which allowed the output power to reach up to 37 W (370 µJ).

Table 2.1 Progressive stages of pulse amplification in FCPA "Solstice".

Parameter	**Power**	**Energy**	**Rep. rate**	**Pulse duration**	**Fiber** Core and inner clad diameter
Rainbow	3 mW	40 pJ	77 MHz	6 fs	
Amplifier 1	300 mW	4 nJ			40/200 µm
Strecther	170 mW	2.3 nJ		3 ns	
Amplifier 2	1 W	13 nJ			40/200 µm
Pockels	0.8 mW	8 nJ	100 kHz		
Amplifier 3	1 W	10 µJ			40/200 µm
Rod	41 W	410 µJ		1.5 ns	80/200 µm
Compressor	37 W	370 µJ		350-380 fs	

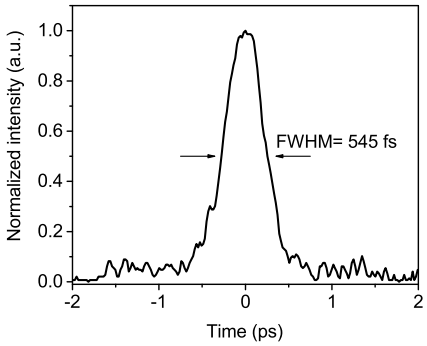

Figure 2.3 Autocorrelation trace of Yb:FCPA "Solstice". Pulse duration is 380 fs.

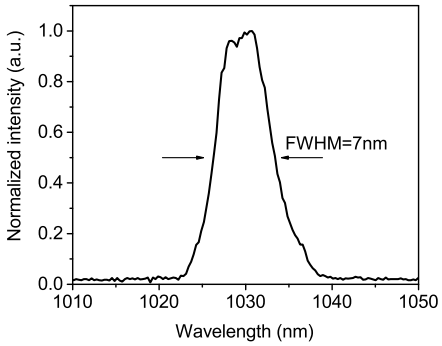

Figure 2.4 Output spectrum of Yb:FCPA.

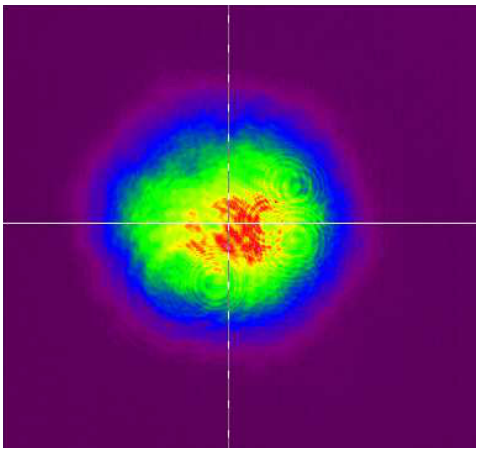

Figure 2.5 Near field beam profile of the rod-type amplifier.

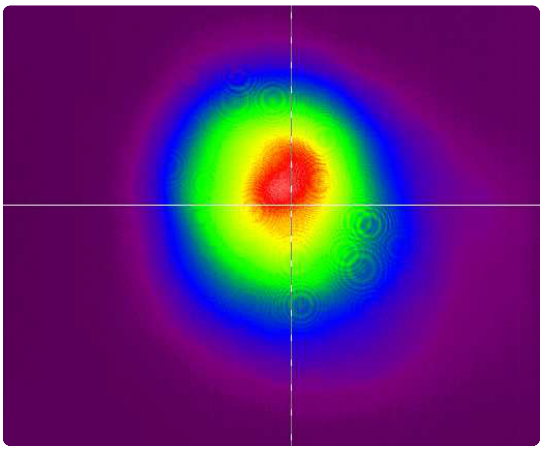

Figure 2.6 Beam profile at the entrance of the OPA, FWHM – 2x2.2 mm.

The spatial beam profile of the rod-type fiber is shown in (Fig.2.5). Afterwards pulses are compressed and delivered into the OPA set up. The distance between the compressor and the entrance of the OPA is about 5.5 meters. Fig.2.6 shows the beam profile after reducing the size with a telescope, consisting of a pair of +500 mm and -200 mm lenses. The beam size after the telescope is about 2.1 mm and is well maintained after 8 m.

2.2 2 μm OPA

State of the art of parametric 2 μm sources

For a long time, the direct intense femtosecond pulse generation from the laser gain medium in the short wavelength infrared was a challenge [3, 4] and intense, ultrashort pulses were exclusively based on the parametric sources. Today, state of the art Tm doped FCPA laser systems [42] could be post-compressed in gas-filled-hollow core fibers and successfully used for high harmonics generation. Still parametric sources have the advantage of wavelength tunability and reaching higher peak power, especially while pumping with high energy, at a lower repetition rate using near-infrared lasers. More details on high energy OPAs will be provided in the next chapter while here we concentrate on high repetition rate systems. Table 2.2 summarizes the state of the art parametric systems in the vicinity of 2 µm.

The most commonly used crystals for the pulse amplification at 2 µm are BBO. Well developed growth methods provide low-cost and featuring high damage threshold BBO crystals with stable and robust performance. Periodically poled crystals were also implemented, but

Table 2.2 State of the art of 2 μm OPAs.

Ref.	λ, μm	Energy, μJ	Rep. rate, kHz	Pulse duration, fs	Nonlinear crystal	Pump laser	CEP stable?
[107]	2	15	1	15	BBO	Ti:Sa	Yes (330 mrad -10s)
[69]	2.1	1.2 mJ	3	15	MgO:PPLN	Yb:YAG	Yes
[108]	1.8	145 nJ	3	11	BBO	Yb:KGW	Yes (135 mrad rms)
[109]	2.1	85	1	32	MgO:PPSLT BBO	Yb:YAG Nd:YLF	Yes (194 mrad 30s)
[110]	2.2	220	1	23	MgO:PPCLN	Nd:YLF	Yes (150 mrad 10s)
[111]	2.1	10	100	16	BBO	Yb:FCPA	Yes (600 mrad 30s)
[112]	2.1	740	1	16	PPLN LN	Nd:YLF	Yes
[113]	1.8	240	1	16	BBO	Ti:Sa	No
[95]	2.1	372	3	32	BiBO	Ti:Sa	Yes (sub 250 mrad 11 min)
[64]	2	60	100	33	BBO	Yb:FCPA	Yes
[71]	2.4	1.2 mJ	0.5	115	KTA	$Yb:CaF_2$	Yes
[114]	1.8	2.5 mJ	1	–	BBO	Ti:Sa (TOPAS)	NA
[115]	2	372	1	–	BBO	Nd:YAG	Yes

the limited aperture and parasitic phase-matching as well as photo-refractive effects prevents power scaling. Bulk crystals are often preferred for use in the booster amplifiers [69, 109], unless a large aperture crystals are available as in [112]. However, in [112] 20% of the output of the OPA belongs to the superfluorescence (this process could be also known as spontaneous parametric down conversion).

Methods to prevent high superfluorescence level were discussed and implemented in [110]. There, the superfluorescence level at the output of the system was 7 % and with pump scaling was estimated to not to exceed 10 % of the increased output signal. Authors suggest a few methods for suppressing the superfluorescence. Firstly, the seed energy for OPA stages should be maximized. If any lossy elements must be inserted, they should be placed into the pre-amplified signal, where losses could be compensated for by following stages and the low signal level for the first amplifier would not be affected. In [110] 2 μm seed energy was maximized by placing the AOPDF after and not before the OPA1, so

the losses were later compensated for by the OPA2 and did not affect the seed for OPA1. Secondly, inserted hard apertures would block the superfluorescence-based higher modes between the two amplification stages. Setting the pump beam size significantly smaller than the signal would implement a soft aperture. This helps to clean the wavefront, and to select the signal with the highest signal to noise ratio by also transferring the clean pump beam profile into the amplified signal. In [110], the second stage pump beam was more than two times smaller than the signal beam and in the last amplifier nonlinear crystal was placed 2-3 diffraction lengths after the signal focal point. Lastly, optimize the pulse durations and spectra for each amplifier, which also would avoid running the amplifiers at a high saturation regime. Superfluorescence will be suppressed, when all signal frequencies near the pump peak are well seeded and the signal is chirped enough to push frequencies, which are at the edge of the phase-matching bandwidth, to the edges of the pump pulse. However, this will reduce the amplification bandwidth compared to the spectral bandwidth expected from the phase-matching curves.

An important factor in achieving few-cycle ultrashort pulses is a generation of a broadband seed. It is also crucial that those pulses were CEP stable, when the pulse duration reaches few optical cycles. The advantage of parametric amplifiers is that the CEP could be passively stabilized. Almost all of the systems feature passively stabilized CEP and in the case of [113] the output signal beam would be CEP stable if the idler beam is extracted from the amplifier. There are few ways to generate CEP stable pulses in the short wave infrared region and the method chosen will depend on the available pump laser. One of the methods would be the intrapulse DFG. The intrapulse DFG could be generated directly from a broadband Ti:Sa oscillator [109]. If the Ti:Sa spectrum is not broad enough, then a fraction of Ti:Sa amplifier could be broadened by self-phase modulation in a gas filled hollow core fiber, post-compressed by a set of chirped mirrors and then sent to the nonlinear crystal for the intrapulse DFG generation [69, 112]. Another way is to use the DFG between two pulses. These two pulses are usually relatively narrowband pump (either Ti:Sa or around 1 μm) and the signal of the visible OPA which is pumped with the second harmonic beam. The seed for the visible OPA could be generated via the white light continuum [111, 108, 107, 64] or direct amplification of the broadband Ti:Sa oscillator spectrum [115]. And lastly idler generation in the OPA, where both pump and signal are driven by the same laser pulses: either SHG or fundamental beams [71]. In the experiment described in the 2 μm part of this chapter, the second method was used. The DFG between the SHG pumped OPA signal around 700 nm and fundamental beam at 1030 nm provided broadband signal at 2 μm.

2 μm OPA experimental set up

The OPA set up presented in this chapter was initially built by dr. Julien Nillon and presented in his PhD thesis [65]. Then it was adapted for a different pump source and a few modifications of the initial architecture were made. The modifications of the architecture were mostly inspired by the 1.8 µm sub-two-cycle OPA constructed in Munich by Homann et al. [108].

The initial system was based on idler generation in a quasi-collinear OPA working at the degeneracy. In that case, signal and idler wavelengths overlap and their separation is complicated. Even though one could separate the two beams by implementing a non-collinear OPA scheme, the generated idler beam would then acquire an angular chirp, which afterwards affects our ability to use the beam for strong field physics experiments, and reach high intensity on the target. The new set up is based on collinear DFG between 700 nm broadband signal and fundamental pump wavelength, which lets us avoid the degeneracy regime and allows us to use chromatic beam separation.

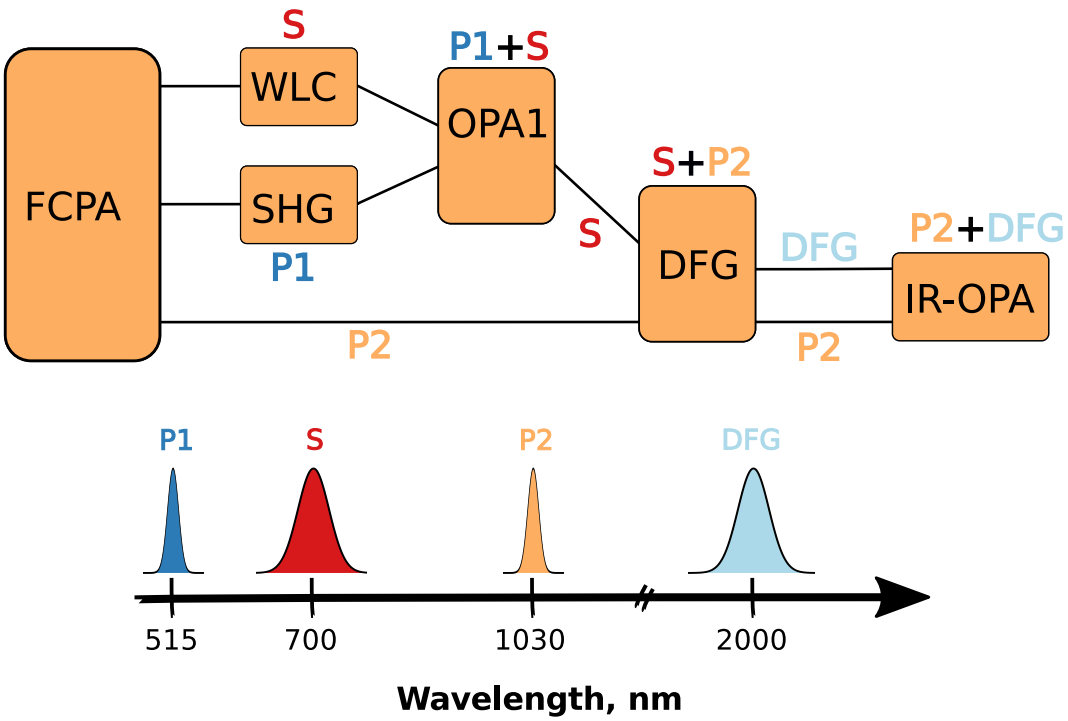

Figure 2.7 The block-scheme of 2 µm OPA set up (top) and the wavelengths used for parametric processes (bottom). P1 - pump of the OPA1 (515 nm), P2 - pump for the IR-OPA (1030 nm).

The scheme of the set up is depicted in Fig.2.7. Here, the pump beam is divided into 4 parts: seed generation in WLC, pump for OPA1, DFG in the second stage and pump for IR-OPA. Firstly, white light continuum, driven by the fundamental beam, is generated in YAG. Simultaneously, the rest of the pump is sent to a second harmonic crystal to generate the pump beam for the first parametric amplifier (OPA1). In OPA1 signal around 700 nm is amplified. In the next stage, the amplified signal is then mixed with the residual fundamental beam and broadband DFG signal is generated at around 2 µm. Lastly, the DFG signal is further amplified in the Mid-IR stage. Here, pump is the fundamental wavelength.

An extra note for the wave mixing in the DFG stage could be taken here. In this stage, the DFG signal is generated between the previously amplified supercontinuum around 700 nm and the fundamental laser beam. The broadband amplified supercontinuum acts as a pump beam (being shorter wavelength) and narrowband fundamental at 1030 nm is the signal beam. The outcome of the stage is a broadband DFG signal around 2 µm. Fig.2.8 shows the tunability between the amplified WLC and generated DFG signals.

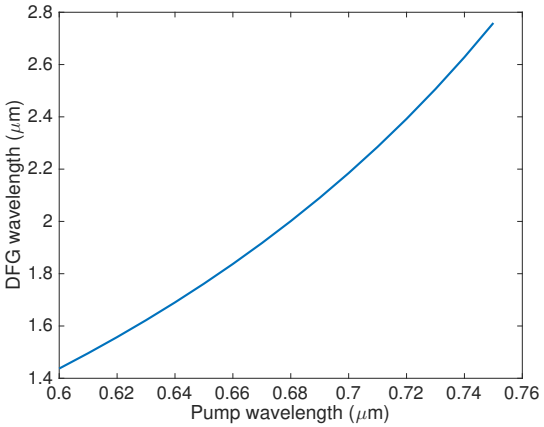

Figure 2.8 Calculated generated DFG signal dependence on the pump wavelengths, while mixing with the fundamental laser beam.

White light continuum generation

At the beginning, white light continuum was generated in a 4 mm YAG plate: the short medium length demanded tight focusing conditions and so a 100 mm lens was used for this purpose. 350 mW of the fundamental beam is focused with a 100 mm lens, the intensity and peak power is estimated to be 3.5 TW/cm^2 and 14 MW, the critical power for WLC

generation is 1.4 MW. The optimized power for the WLC generation exceeded the critical power by about 10 times. This could be the result of instabilities and higher power would assure the presence of WLC signal to seed the OPA. The generated spectrum was broad enough, it fully covered the required spectral region in the near-IR spectral region around 700 nm. However, the pump laser instabilities had a strong impact on the successful WLC generation. Due to the tight focus, energy fluctuations of the pump laser would quickly result in a multi-filamentation (Fig. 2.9), no WLC generation at all or even the laser induced damage of the YAG plate. Even though the RMS of the pump laser was measured to be 1 % for the pulse to pulse stability.

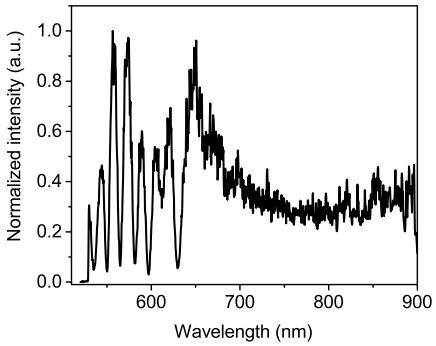

Figure 2.9 The interference fringes showing the multifilament generation in a 4 mm YAG plate.

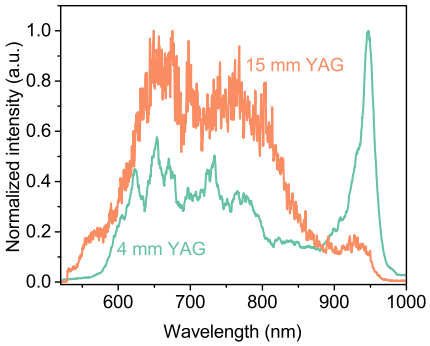

Figure 2.10 WLC generation in 4 mm and 15 mm YAG.

Longer material length allows us to use loose focusing, because the beam has a longer distance to accumulate nonlinearities, thus lower intensity is required for the process to take place. Furthermore, focusing conditions could be chosen to generate the WLC further from the surface, which might reduce the possibility of laser induced damage as it was reported in [82]. We have confirmed that longer material provides more stable supercontinuum generation, and prevents us from damaging the crystal. This time the WLC was generated in a 15 mm YAG rod and the pump beam was focused with a 200 mm lens, which also reduced the required pump power for WLC generation from 350 mW to 130 mW. Spectra comparison in Fig. 2.10 shows that the spectrum generated by both methods has a reasonable spectral intensity, thus is suitable to seed the first stage. However, the overall system performance is increased when the WLC is generated in the rod. Similar results were also obtained in [82], where white light continuum was generated in 6 mm and 10 mm YAG crystals. Spectral broadening was investigated under different focusing conditions and the visible part was much less influenced by either the divergence of the input beam, or by the crystal length.

Both the spectral intensity and spectral broadening stays at the same level of magnitude. However, the signal generated in the infrared side could differ by one order of magnitude.

OPA 1

The generated WLC is re-imaged into the first amplifier by a -200 mm ROC silver mirror, the fundamental is rejected with a short-pass dichroic mirror. To pump the first amplification stage a second harmonic wavelength has to be used, thus the SHG is generated in 1 mm BBO crystal (Θ = 23.4 deg). 25 W is sent to the crystal and 5 W of SH is generated, the efficiency of the stage is 20 %. The rest of the fundamental beam is later used to generate the difference frequency in the DFG stage and pump the last amplification stage. The pump beam is focused into a first stage (5 mm BBO, Θ = 21.3 deg) by 300 mm lens. The broadband signal around 700 nm is amplified up to 1.5 W (500 mW of superfluorescence). The efficiency of the stage is 30% and gain is 500.

In the first amplification stage a non-collinear configuration at the magic angle was used, providing broadband amplification around 700 nm. The magic angle between signal and pump pulses inside the crystal is 2.1 deg. Phase-matching and signal amplification gain curves for different crossing angles are depicted in Fig. 2.11 and Fig. 2.12. The amplification bandwidth significantly changes even due to a small (0.1 deg) deviation in the crossing angle between pump and signal.

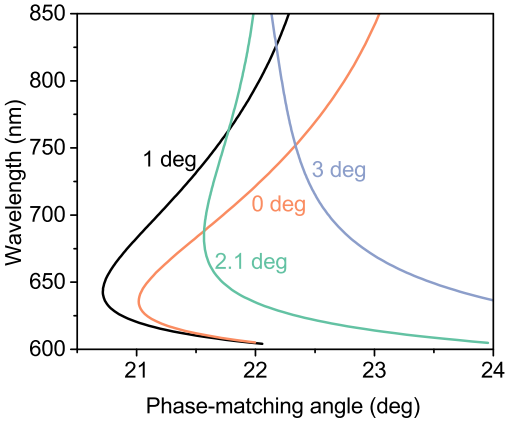

Figure 2.11 Phase-matching curves for different angles between pump and signal beams in BBO crystal. Data from SNLO software.

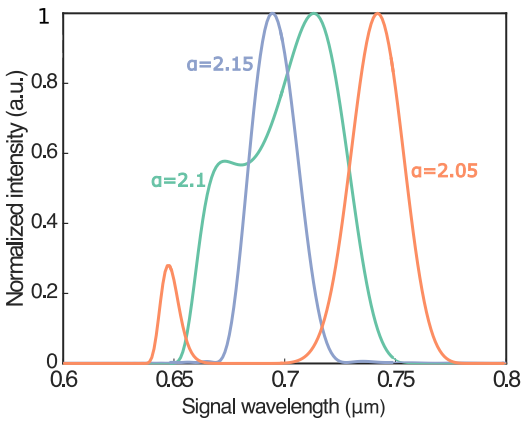

Figure 2.12 Typical amplification bandwidth at different angles between pump and signal beams in BBO crystal.

The phase-matching width could be further increased taking advantage of the broadband pump. The width (FWHM) of fundamental pump spectrum is 7 nm (see Fig. 2.13). Even though the second harmonic spectrum is narrower by a factor of $\sqrt{2}$, the spectrum is still broad (5 nm) and a wider area for phase-matching conditions is covered. The marginal phase-maching curves are depicted in Fig. 2.14. The vertical line in Fig.2.14 depicts the broadest possible phase-matching conditions within the pump wavelength at a certain angle. In this way, we could evaluate the expected amplification bandwidth. The amplified spectrum is expected to extend from 667 nm to 745 nm ($\Delta\lambda$ = 78 nm).

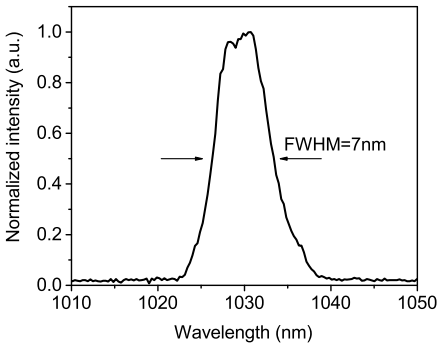

Figure 2.13 Spectrum of the pump laser

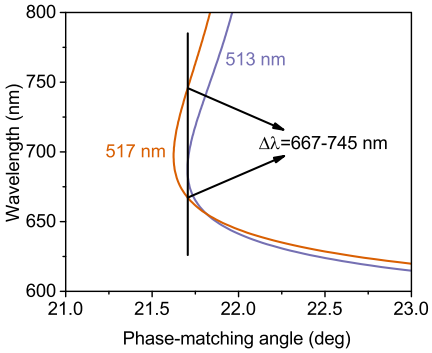

Figure 2.14 Phase-matching curve for minimal and maximal wavelengths of broadband pump.

Normalized spectra of experimental results are depicted in Fig. 2.15. The WLC (blue shadowed spectrum) provides a strong and sufficiently broad and flat spectrum in the vicinity of 700 nm, which is the region of interest for the amplification in the OPA1, in order to generate the idler around 2 µm. OPA1 is pumped with the SH and 53 nm (FWHM) broadband spectrum around 700 nm is amplified. The spectrum is narrower than expected because, it was optimized for the power, at the cost of spectral bandwidth reduction. Optimization for power was more important because the beam was meant to serve as a pump beam for the next stage and the bandwidth was still broad enough to generate broad DFG signal.

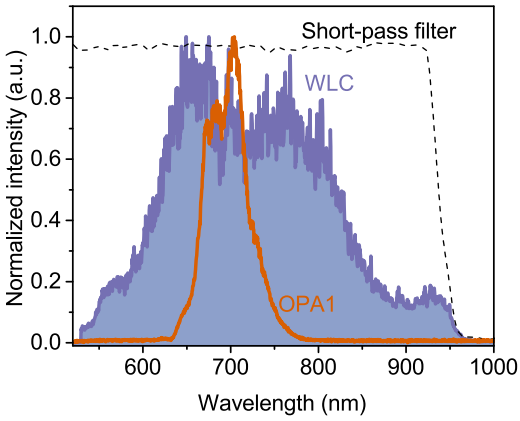

Figure 2.15 Spectra of WLC and the OPA1.

DFG and IR-OPA stages

Here we take the amplified signal from the previous stage and use it as a pump beam to pump the DFG stage. Which means that in the DFG stage we mix the broadband pulses at around 700 nm and narrowband 1030 nm fundamental. It is important to keep the DFG stage collinear in order to avoid angular dispersion of the generated idler beam. The amplified signal from the OPA1 is collimated by -300 mm ROC silver mirror and focused into the DFG crystal (5 mm BBO, Θ = 21.3 deg) with a 1000 mm lens. The collimated fundamental beam is focused with a 1000 mm lens. Losses for the fundamental beam are as high as 60 % – just 12 W out of 20 W, left after the SHG stage, are delivered to the DFG stage. These high losses are due to the beam clipping as optics with a limited aperture (0.5 inch) were used. The generated broadband idler is around 2 µm. The DFG signal power is 30 mW and the efficiency of the stage is 2%.

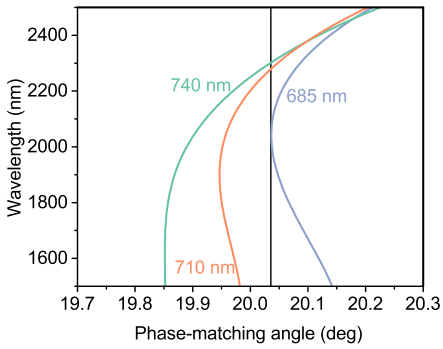

Figure 2.16 The phase-matching curves at the DFG stage for the limiting spectral wavelengths of the pump.

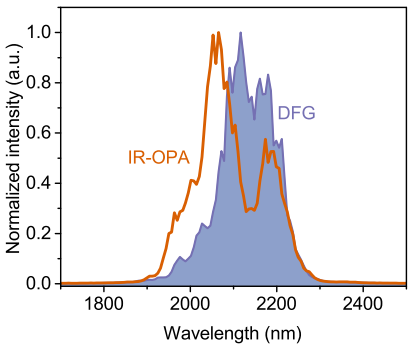

Figure 2.17 Experimental spectra of the DFG stage and IR-OPA.

A 150 nm width DFG beam centered at 2.1 µm is generated. This spectrum supports 43 fs pulses (6 optical cycles) and lies between 1.9 µm and 2.3 µm. As it could be seen from Fig. 2.16, the phase-matching limit to the longer wavelength side is indeed 2.3 µm, however, even though the phase-matching looks far extendable on the blue side, there the DFG is limited by the energy conservation. The marginal wavelengths of pump spectrum at the FWHM, when mixed with 1030 nm would provide spectrum between 2.05 µm and 2.6 µm.

After the DFG signal is generated, it is further amplified in a 5 mm BBO, type I configuration. Here, a spectrum slightly broader than that of DFG is amplified – 170 nm, which supports 38 fs (6 optical cycles). The magic angle for the intersection inside the crystal for these wavelengths is 0.85 deg. As we can see from Fig. 2.18 and Fig. 2.19 the angle between the pump and signal is less sensitive in the case of amplification of longer wavelengths compared to OPA in the visible.

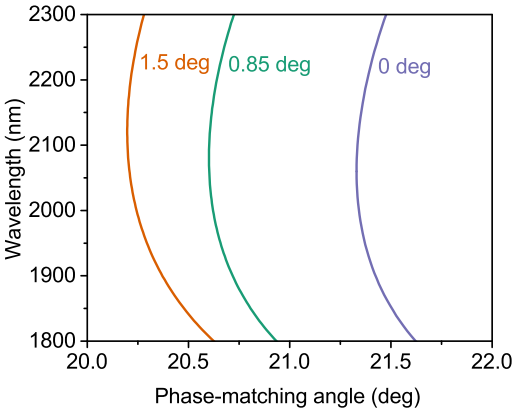

Figure 2.18 The phasematching curves for different intersection angles in BBO crystal for broadband amplification at 2 µm, magic angle is 0.85 deg.

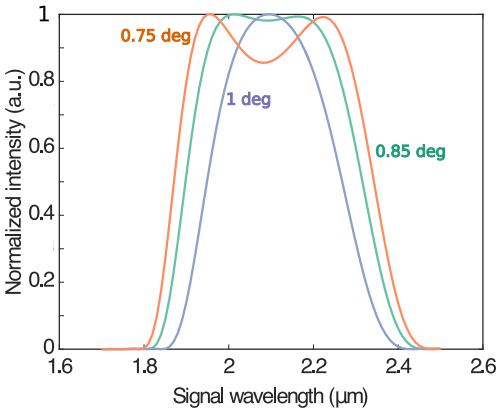

Figure 2.19 The development of amplification at different angles between pump and signal beams in BBO crystal.

Summary of the 2 µm OPA

Table 2.3 Summary of 2 µm OPA performance.

Stage	BBO Crystal	Output wavelength	Output power	Efficiency	Gain
OPA1	5 mm	700 nm	1.5 W	30 %	5000
DFG 1	5 mm	2 µm	30 mW	2 %	
IR-OPA	5 mm	2 µm	150 mW	1.5 %	5

To sum up, the output of this OPA provided 1.5 µJ pulses at 2.1 µm, the pulse duration was not measured and post-compression not performed, but it was evaluated that pulses featuring the output spectrum could support 40 fs - 6 optical cycles. The summary of all the stages is shown in Table 2.3. The pros of the configuration:

- Even though the overall efficiency of the system was low, the 2 µm beam was generated in a collinear configuration out of degeneracy, did not feature angular dispersion, and was easily separated from the signal and pump beams.
- The WLC tests lead not only to the improved generation stability, but also to the extension of the generated spectrum in the infrared side, which simplified the development of the 3 µm OPA system, described later in this chapter.
- Optical components for the 3 µm OPA were chosen more carefully to handle high power beams.

The cons of the configuration were:

- The white light continuum generation: the seed signal for OPA was unstable, which led to fluctuations in the whole system. Stability was improved by changing the WLC stage configuration.
- Due to small aperture of some of the optical components, the beam delivery losses were too high to fully exploit the pump laser.
- The chosen configuration might have not been the most efficient as a lot of power is used for the DFG signal generation, which features low efficiency and just half of the laser power is left for further amplification.

Despite the limited performance, the system was successfully used to study a new nonlinear crystal (LGT) as detailed at the end of the chapter.

2.3 3 μm OPA

Introduction to MWIR OPAs

There are only a few laser gain media suitable for intense femtosecond pulse generation in the mid-wavelength infrared spectral region. The overall scalability of the pulse repetition rate, the duration and the power are still a challenge [3, 4]. To mention but a few state of the art laser sources, four-cycle pulses were achieved in a graphene mode-locked Cr:ZnSe at 2.4 μm with an output power of 250 mW and a pulse energy of 2.3 nJ [116]. In an amplified architecture, 300 μJ pulses were generated in Cr:ZnSe at the repetition rate of 1 kHz with a pulse duration of 300 fs [117]. Fiber technology is also able to produce MWIR radiation where, for instance, 207 fs pulses at 2.8 μm were generated in an Er-doped fluoride glass fiber laser providing peak powers up to 3.5 kW [118]. However, these sources are not yet sufficient for high order harmonic generation and other strong field physics experiments.

An alternative approach to simultaneously generate high energy short pulses in the MWIR region is based on nonlinear frequency conversion by means of three-wave mixing in a second-order susceptibility crystal. A summary of parametric sources at 3 μm is given in Table 2.4. The reported systems are mostly based on periodically poled crystals. This is mainly due to their high d_{eff} and extended transmission into the MWIR together with the possibility to use a near-infrared pump laser. However, there are some limitations in terms of

the power scaling [119]. As an alternative, KTA crystals could be used [120, 88, 121].

Table 2.4 State of the art of 3 μm OPAs.

Ref.	λ, μm	Energy, μJ	Rep. rate, kHz	Pulse duration, fs	Nonlinear crystal	Pump laser	CEP stable?
[46]	3.1	18	160	67	PPLN	$Nd:YVO_4$	Yes 250 mrad 30min
[43]	3.6	2	1	25	PPSLT	Ti:Sa	NA
[122]	3.4	21.8	50	44.2	APPLN	$Nd:YVO_4$	NA
[123]	tunable: 2 - 3.7	1	1	4 opt. cycl.	APPLN	Ti:Sa	NA
[89]	3.1	40	100	40	PPLN	Yb:YAG	Yes 81 mrad rms
[88]	3.9	8	20 Hz	85	KTP KTA	Nd:YAG	No
[119]	3.07	10	125	72	PPLN	Yb:FCPA	Yes
[120]	3	8	100	85	CPPLN KTA	Yb:FCPA	Yes

Most applications of high repetition rate parametric lasers sources are white light generation [14] and high order harmonic generation in solids [120]. Only high energy systems working at lower repetition rates were able to provide HHG in gases [88, 50]. So far, the HHG in gas, thus the attosecond pulse generation reaching the water window, are not yet accessible with the high power MWIR drivers, but these sources are suitable for strong field physics experiments in solids. The solid HHG driven by 100 kHz system [120] produces results in agreement with the experiments driven by lower repetition rates [55, 75], which means that the increased thermal load on the sample does not affect the process. The material damage is mainly caused by multi-photon absorption and tunnel ionization. Driving experiments with longer wavelength (3.25 μm) laser source allows us to reach similar intensities of the electric field while invoking different physical processes (tunneling ionization versus multi-photon absorption) if compared to the Ti:Sa sources. Thus, longer wavelength drivers for experiments in solid state materials have the advantage of higher damage threshold, which is due to the smaller photo-absorption cross-section in the case of high order processes [55]. Both HHG in solids and WLC generation were demonstrated with the 3 μm parametric source described in this section.

The experimental set up

The scheme of our three-stage optical parametric amplifier is shown in Fig. 2.20. The system was pumped by the laser system "Solstice", which was described earlier. This Yb:FCPA delivers 350 fs pulses and pulse energy of 290 μJ (29 W) was available for this experiment at repetition rate of 100 kHz.

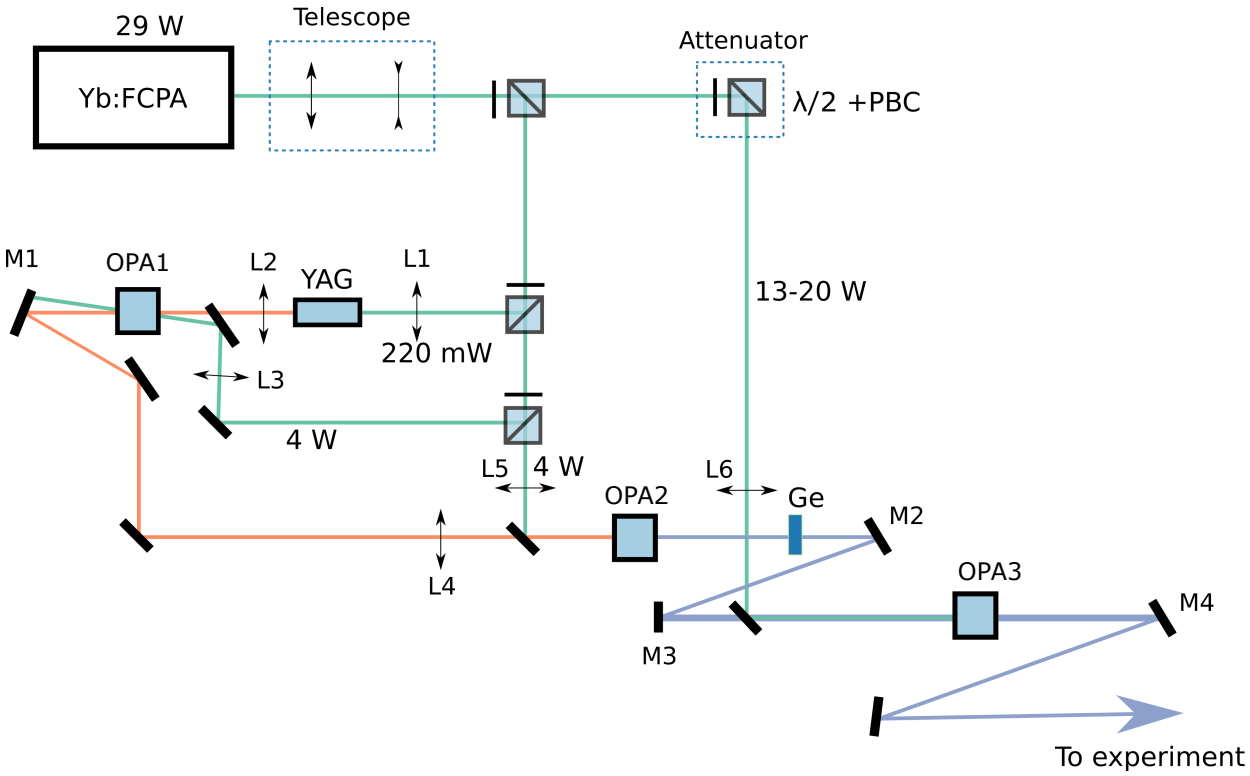

Figure 2.20 Scheme of a three-stage OPA. Beam size reducing telescope consist of two lenses with the focal length of +500 mm and -200 mm. The attenuator consist of $\lambda\backslash 2$ plate and a polarizing beamsplitter cube (PBC). Lenses: L1 – 250 mm, L2 – 50 mm , L3 – 300 mm, L4 – 150 mm, L5 – 300 mm, L6 – 750 mm. Mirrors, ROC: M1 – -250 mm, M2 – -500, M3 – -1000 mm, M4 – -500 mm.

Firstly, a white light continuum is generated in a 15 mm YAG rod. The infrared part of the continuum afterwards serves as a seed for the first amplification stage (OPA1). In OPA1, a 6 mm KTA crystal is used and the stage is pumped by the fundamental frequency (FF) (1030 nm). A broadband signal at 1600-1700 nm is amplified in a non-collinear configuration. Then, pulses amplified in the first stage are further amplified in OPA2. Here a chirped PPLN crystal is used. A collinear configuration is implemented in order to generate angular chirp-free idler at 3 µm. This broadband idler is later amplified in the last stage. To select

the idler beam, we use chromatic separation in a 3 mm Ge filter that absorbs the signal and pump beams. In the last stage we again use a KTA crystal (10 mm). Here KTA is chosen due its higher damage threshold and less expressed parasitic phase-matching. After the full characterization of OPA3 output, the beam is used for HHG generation in ZnSe.

This architecture was chosen after a successful WLC generation to the infrared side of the pump. It simplifies the passive CEP stabilization and reduces the required number of stages to achieve it. Because the WLC is generated from the FF and it is also used to pump the OPA1, the generated idler pulses are already passively stabilized. CEP stabilization is achieved after only one stage, compared to the 2 μm system, where at least two are required. Furthermore, there is no SHG stage, which makes the system potentially more efficient.

White light continuum generation

The seed for the parametric amplifiers is a white light continuum generated in a 15 mm YAG rod. Contrary to the 2 μm system, here not the visible, but the infrared part is amplified (see Fig.2.21).

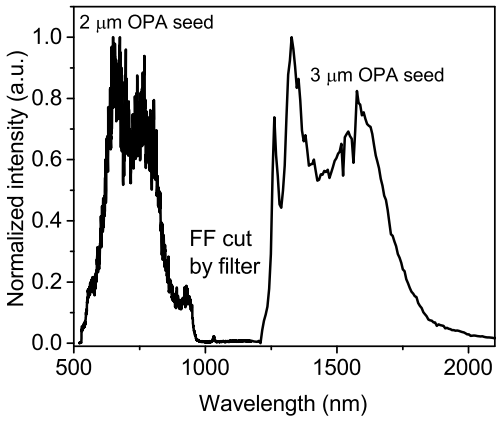

Figure 2.21 White light continuum in 15 mm YAG rod. The fundamental frequency is cut by the filter.

In order to generate a sufficiently broad and stable seed for the SWIR OPA, we tested WLC generation in YAG crystals with different length and at various focusing conditions. After selecting the optimal crystal length, we performed a power scan. This experiment was done within a collaboration with Dr. Julien Nillon from Amplitude Systemes at their

facilities in Pessac (France). We had 4 YAG crystals available: 4 mm, 7 mm, 10 mm and 15 mm. And 5 lenses to focus beam into the crystal: 50 mm, 100 mm, 150 mm, 175 mm and 250 mm. The experimental set up is the same as depicted in the bottom of Fig.2.25. For each crystal we measured spectrum at each focusing conditions. The optimal crystal position at the focus was defined by approaching the focal spot and reducing the pump power for a stable, single-filament WLC. As this continuum would be later used to seed SWIR or MWIR OPAs, we have focused only on the infrared side of the WLC. The development of spectra is shown in Fig.2.22.

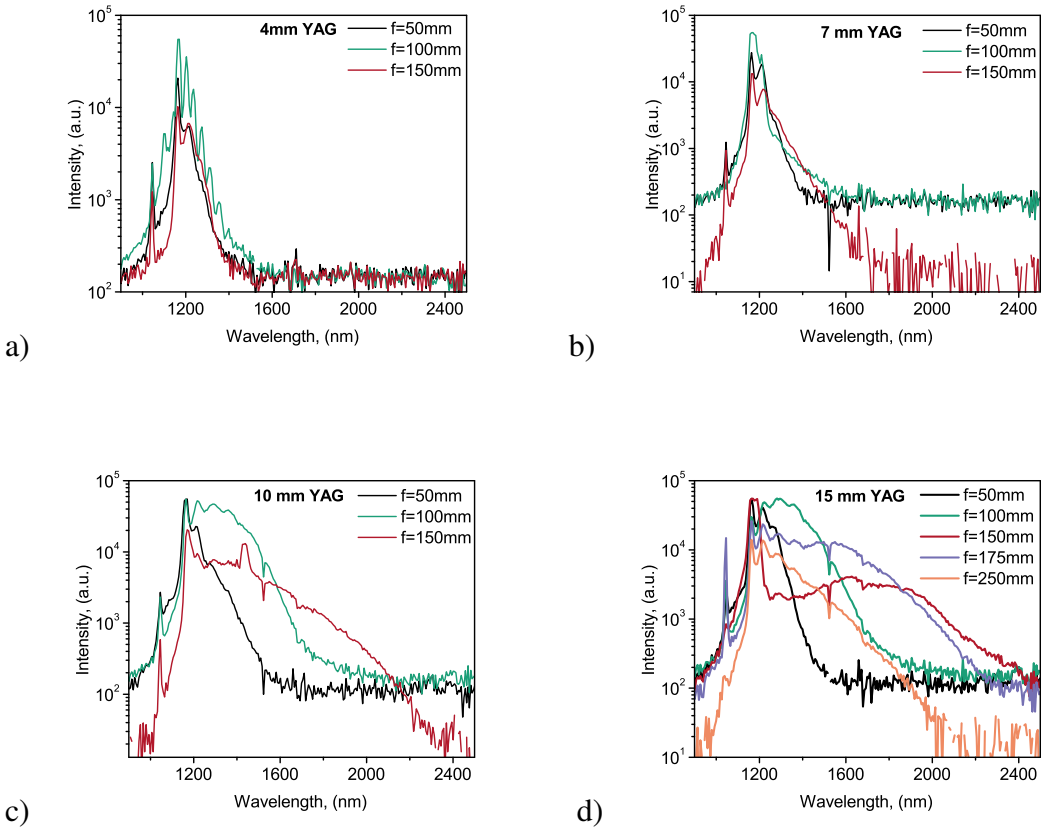

Figure 2.22 White light continuum generation in different length YAG rod and at various focusing conditions. The fundamental frequency is cut by the filter.

We could see, that when we increase the crystal's length, the supercontinuum broadens towards the infrared side. The broadest WLC is obtained in 10 mm and 15 mm crystals, while focusing with a 150 mm lens. The spectrum reaches 2.4 µm. The slope of spectral intensity is steeper in 10 mm YAG, thus 15 mm YAG provides a stronger seed signal for the OPA. In the 15 mm crystal we could also clearly observe that there are optimal focusing conditions.

When the 150 mm lens is changed to the longer ones, the broadening cut off is reduced. After identifying the optimal crystal length, we performed the power scan (see Fig.2.23). The spectral broadening is constantly increasing until the threshold of the multifilamentation is reached at 330 mW.

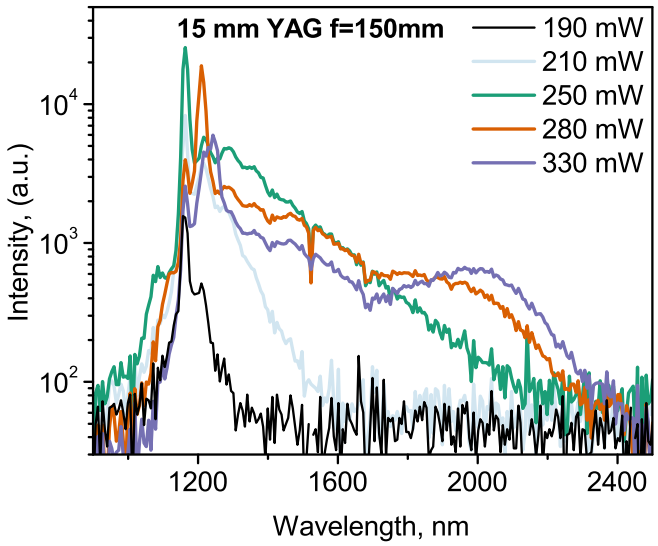

Figure 2.23 Power scan in 15 mm YAG rod. The fundamental frequency is cut by the filter.

A very similar experiment was conducted in [82]. Here, the authors also show that there are optimal focusing conditions for obtaining the largest broadening into the infrared side. When increasing the focal length of the focusing lens, the maximum spectral width is reached and then starts to decrease. In [82] the broadest continuum in 10 mm YAG was achieved, when the pump beam divergence was 14 mrad. Also, a broader continuum was generated in a the 10 mm long YAG crystal compared to the 6 mm long. The long generation medium allows us to use looser focusing conditions, thus when the longer filament is formed the broadening process develops smoothly.

In the case of tight focusing and short WLC generation media, the point where the continuum is generated is fixed. Energy fluctuations of pump laser would mostly impact the stability of the generated continuum. However, when loose focusing conditions and long media are used, the energy fluctuations of the pump laser would also impact the position in the media, where WLC is generated. The pump beam propagates in the media and accumulates intensity-depended nonlinearities, thus when energy varies, the continuum is generated after a different propagation distance. This impacts the imaging into the OPA stages. The

divergence of generated WLC is fluctuating, which results in shifting the focal point of the seed beam along the nonlinear crystal in the OPA.

Afterwards, the conclusions from previously described supercontinuum generation experiments were to be applied to the development of the seed generation for our 3 μm OPA. We have chosen the focusing conditions using the same method – by testing lenses with different focal lengths and looking at the broadening as well as the stability of the filament. The system is pumped by Yb:FCPA Solstice, so conditions for optimal WLC generation differ from the ones obtained during the previous WLC optimization experiment. Here, the optimal conditions were: pump pulse energy of 0.22 μJ and a focusing lens with the focal length of 250 mm. The beam size on the focusing lens was about 2 mm, thus the estimated beam size in the focus is about 100 μm. The intensity at the focal point is 80 GW/cm^2 and peak power of 6 MW. Our configuration allows generation of spectra extending up to 2.2 μm (Fig.2.24).

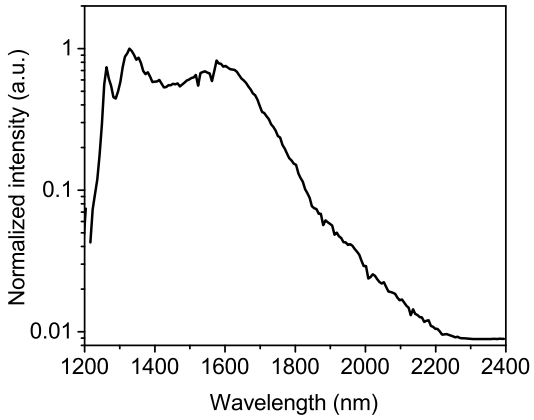

Figure 2.24 Infrared side of the WLC generated in 15 mm YAG rod.

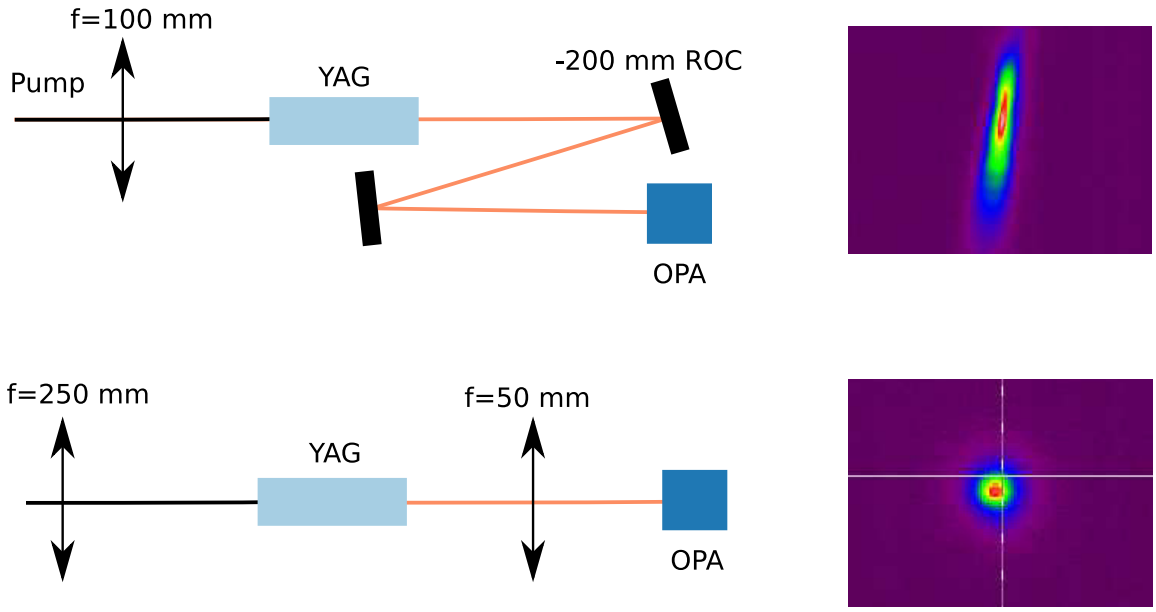

Figure 2.25 Folded WLC generation set up in the 2 µm OPA (top) and in line set up in the 3 µm OPA (bottom) and the corresponding beam profiles.

After the generation, the WLC is re-imaged into the first amplification stage by a 50 mm lens. Fig.2.25 shows two different imaging configurations. Folded continuum imaging used in the 2 µm OPA is shown in the top scheme. Here WLC was re-imaged with -200 ROC mirror, which required using a small reflection angle, and due to the large beam size, was difficult to implement. This resulted in the elliptical WLC beam at the focus. In that case, the crystal should be placed out of the focus, so the stage is not optimally seeded – intensity of the seed is lower, which might result into parasitic generation of superfluorescence.

In the 3 µm set up, inline imaging is used (see the bottom scheme of Fig. 2.25). Here, OPA1 is inline with the WLC, which, compared to the 2 µm OPA, better maintains the beam quality. In the inline configuration, the seed maintains the quality of the pump beam.

OPA1

The first OPA stage consists of 6 mm KTA crystal. The phase-matching conditions for the non-collinear interaction are shown in Fig. 2.26. The amplified signal will be further amplified in the next stage, thus a non-collinear configuration was suitable to use. The angularly chirped idler beam is rejected after the OPA1. Theoretically the optimal angle between the signal and pump beams is 4.7 deg. However, experimentally the best amplification was

achieved when the two beams were intersecting with the angle of 2.5 deg. This is due to the optimal overlap of both beams throughout the whole crystal length – if the angle is increased the interaction length is shortened which results in lower amplification. The interaction length for an angle of 4.7 deg would be 2 mm, which is one third of the 6 mm crystal, which was available for the experiment. Another reason for the improved amplification at a smaller intersection angle is that the crystal is cut at 39.5 deg and the phase-matching angle for the intersection of 4.7 deg is around 55 deg. The crystal should have been tuned further to allow all of the beams to propagate along the crystal without getting clipped by the edges.

In the OPA1 a pump pulse of 40 μJ is focused by a 300 mm lens to reach a peak intensity of about 0.5 TW/cm^2. The beam sizes of the pump and signal beams at the crystal are 80 µm and 70 µm respectively. A 200 nm broad spectrum centered around 1.6-1.7 µm (Fig.2.27) is amplified up to 60 nJ in a non-collinear configuration with the internal angle between pump and signal beams being 2.5 deg.

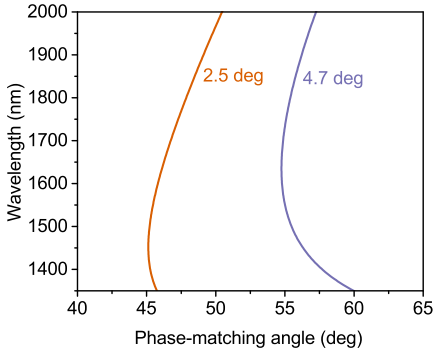

Figure 2.26 The theoretically (4.7 deg) and experimentally (2.5 deg) optimal phase-matching curves for signal amplification in the OPA1.

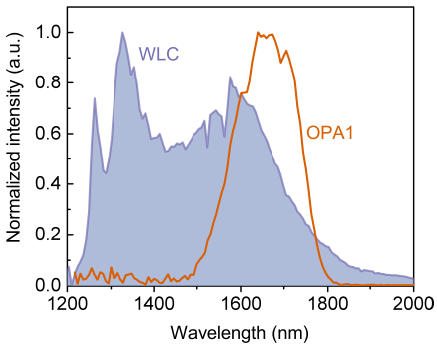

Figure 2.27 Spectra of seed and amplified pulses in the OPA1.

OPA2

In the second OPA stage a 7.4 mm long cPPLN crystal (HC Photonics Corp.) was used. The poling period is linearly chirped from 28.4 to 31 µm. Here, CPPLN crystal was chosen for its broader and flatter spectral gain profile as well as limited back conversion compared to PPLN crystals [124]. Additionally, the d_{eff} is more than 10 times higher than a KTA crystal. The collinear configuration allows generation of angular chirp free idler pulses, which are

later amplified in the last OPA stage.

The seed and amplified signal spectra are shown in Fig.2.28. One could notice that spectrum of amplified signal is narrower than the seed. This is because the stage was optimized for the generation of the idler pulses. Two different spectrometers were used to measure signal and idler beams of this stage. A grating spectrometer (Nirquest 256) based on InGaAs detector with the resolution of 7.6 nm and the detection range lying between 900 nm and 2.5 µm was used to measure the signal beam. To measure the spectrum of idler beam spreading between 2.4 µm and 3.3 µm we used an acousto-optic device based spectrometer (Mozza). This is a scanning spectrometer, thus a real time/single shot spectrum recording is complicated. The principle of the spectrometer's operation is as following: a generated acoustic frequency diffracts a corresponding single optical frequency, then the diffracted signal is recorded with a photodiode. During the measurement, the acoustic frequencies are scanned and the optical spectrum is reconstructed. The detection range of this spectrometer is 1 – 5 µm. The scanning speed, thus also the spectral resolution could be chosen in the range of 2 – 100 cm^{-1}; 2 cm^{-1} at 3 µm corresponds to a resolution of 1.8 nm. A larger scanning step is very useful to position the spectrometer along the beam. Also, in the fast scan regime the optimization of the amplification is easier as the spectrum is monitored in an almost real time.

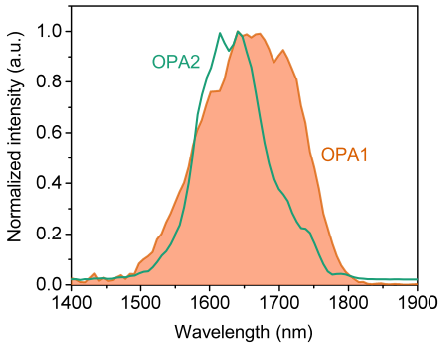

Figure 2.28 Spectrum of the amplified signal in the OPA2. Measured with Nirquest 256.

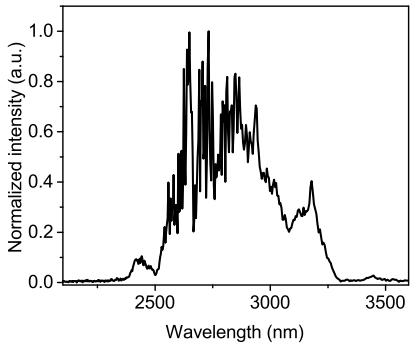

Figure 2.29 Spectrum of the generated idler pulses in OPA2. Measured with Mozza.

Despite the many advantages of PPLN crystals, they also have a few drawbacks, such as phase-matched parasitic effects. Spectra of a second harmonic generated in OPA2 is shown in Fig. 2.31. There spectra were measured at the output of the OPA2 with and without seeding. The integrated signal of the seeded OPA is 0.7 of the unseeded one. When the

OPA is pumped with 23.5 µJ, 300 nJ of SHG is being generated, which corresponds to 1.3% efficiency. Furthermore, the generated SH phase-matches afterwards with the seed pulse and generates new difference-frequency wavelengths. This DFG signal is at 720 – 785 nm range and indeed a red beam appears at the output of the OPA2.

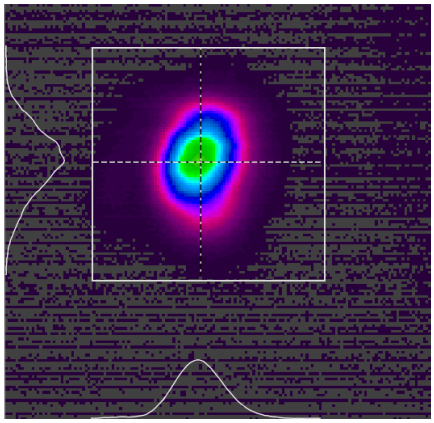

Figure 2.30 Beam profile of collimated idler beam of OPA2.

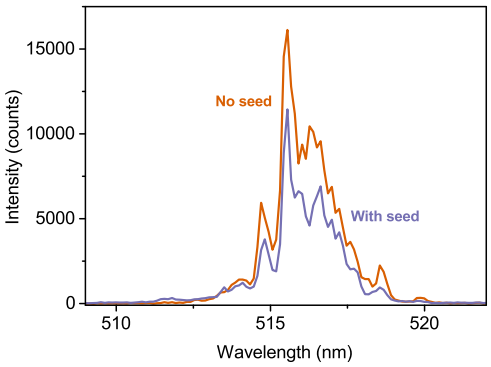

Figure 2.31 Parasitic second harmonic generation in cPPLN crystal.

In OPA2 40 μJ of pump is used and the signal coming from the previous stage is further amplified up to 2 μJ, and 0.75 μJ of idler at 3 μm is generated. The pump beam is focused with a 300 mm lens, with the focus shifted 80 mm after the crystal. The pump intensity at the crystal was 46 GW/cm^2. Efficiency in this stage reaches 4% for a gain of 33. The power scaling of the stage is shown in Fig.2.32. We could see that at first the efficiency is increasing, but then suddenly drops. This drop could be related to the previously described parasitic phase-matching. Pump beam energy gets drained for the parasitic second harmonic generation, which then starts depleting the amplified signal. The threshold for this process is between 15 and 20 μJ; which corresponds to the estimated pump intensity of 17 GW/cm^2 and 23 GW/cm^2. Finally, the pumping level is set to generate sufficient seed for the OPA3. The beam profile of collimated idler beam is shown in Fig.2.30.

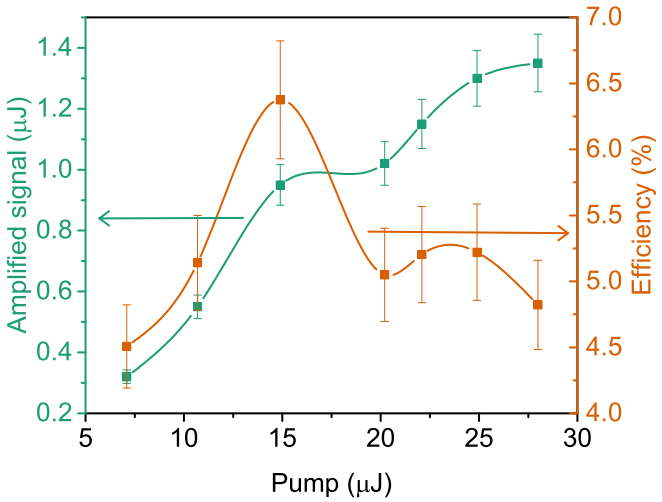

Figure 2.32 Power scaling in the second amplification stage – cPPLN crystal.

OPA3

Idler pulses generated in the previous stage are collinearly amplified in a 10 mm long KTA crystal in the last OPA stage. While the cPPLN used in the second stage provided an ultra-broad gain bandwidth, KTA has been chosen here for the last power stage. Parasitic phase-matching was already observed in the second stage, and so would be equally expected in this stage. Enlarging the pump beam size, thus reducing the intensity on the crystal would decrease the threshold for the parasitic processes. However, the enlargement of the seed beam would be also needed, which might prevent sufficient seeding and provoke parametric superfluorescence generation. Due to its thermal, mechanical and optical properties, a KTA crystal based architecture can achieve better performance when scaling up the average and peak power. KTA features a reduced absorption in the 2-5 μm region, as well as broad angular and temperature bandwidth and low dielectric constants. KTA crystal is also non-hydroscopic. Furthermore, the power scaling limitations in PPLN were observed in [119]. The authors list different processes causing the beam degradation, such as GRIIRA (Green Induced Infrared Absorption), linear absorption, photorefractive effect and pyroelectric effects. Furthermore, the beam degradation is also related to the signal/idler beam presence. Even though the process is not yet fully identified, it's likely that the nonlinear absorption phenomenon also takes place.

The phase-matching curve for collinear amplification in this stage is shown in Fig. 2.34. The phase-matching conditions are slightly broadened due to the broadband pump. An

amplified spectrum is provided in Fig. 2.33. The spectrum is much narrower compared to the seed, this is due to the collinear phase-matching conditions (Fig. 2.34). An internal angle of 2.1 degrees in the crystal on the plane perpendicular to the optical axis was implemented in order to separate the amplified signal from pump and idler.

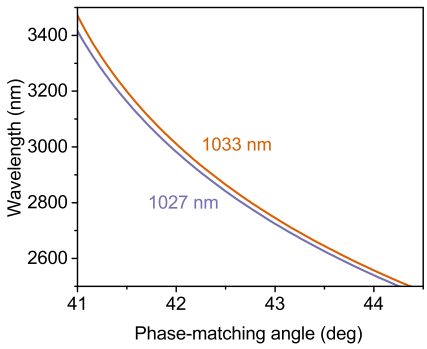

Figure 2.33 Phase-matching curve for 3 µm amplification in the OPA3.

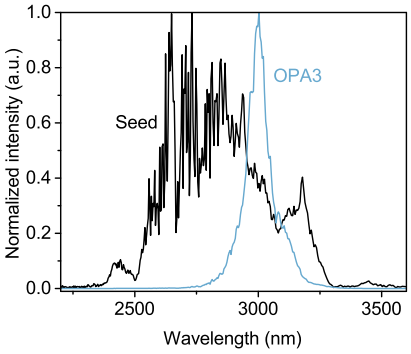

Figure 2.34 In the last amplification the stage idler of the second stage is amplified.

After the generation, the seed signal for this stage is collimated and focused by -500 mm ROC and -1000 mm ROC silver mirrors, while the pump beam is focused by +750 mm lens. The focus is shifted after the crystal in order to better match pump and seed spot sizes which are measured to be around 420 μm (FWHM) for the pump and 640 μm (FWHM) for the signal beam. Peak intensity of the pump is 0.1 TW/cm^2. The mismatch between the spot sizes is kept in order to extract the maximum energy from the pump beam and to suppress the potential superfluorescence due to weak seeding at the edge of the signal beam and to increase the spatial beam quality by selecting the central part of the seed for amplification. The amplified signal is afterwards collimated by -500 mm ROC silver mirror.

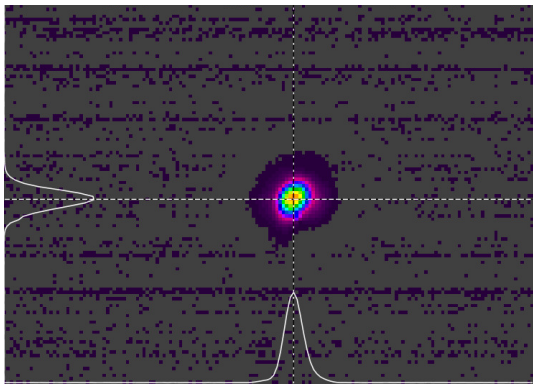

Figure 2.35 Beam profile of seed pulses at the OPA 3, FWHM 640 µm .

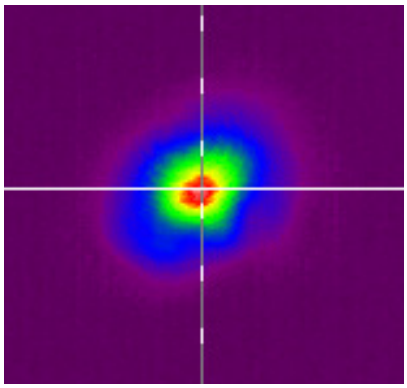

Figure 2.36 Pump beam profile at the OPA 3, FWHM 480 µm.

In order to separate the seed of the third stage from the residual pump and signal beams after the OPA 2, a 3 mm uncoated germanium filter is inserted. The transmission of the filter is 45 %, so only 330 nJ of seed is injected in the amplifier. The remaining laser energy (130 μJ) is used to pump the last stage and the signal is amplified up to 8.2 μJ. The maximum level of superfluorescence is estimated by blocking the seed and measuring the pulse energy, which is about 200 nJ (2.5 %) and is likely to decrease when amplification process takes place. The efficiency of the amplification in this stage is 6.3 % and the gain is 25. The overall efficiency of the system, energy conversion from total pump into the idler beam is 2.8 %, which is similar to the other high repetition rate set-ups 2 % [125] and 4.5 % [122]. For the last stage when the energy of the pump pulses was set to 200 μJ, 15 uJ (7.5 % stage efficiency) pulses at 3 µm were achieved with slight changes to the spectral and temporal characteristics. The power scaling and efficiency curves at two different times are provided in Fig. 2.38 and Fig. 2.37. The data for Fig. 2.37 were taken at the beginning of the characterization of the OPA3. Maximum efficiency was about 9.3 %. As time passes, we have observed that the efficiency of the OPA is decreasing. Measurements taken after about 6 months show the efficiency decreased by 4 %; the maximum efficiency was 5.3 %. The decrease in the stage performance could be linked to the aging of the crystal. However, it was suspected that the amplification efficiency also depends on the beams position in the crystal. This could be caused by the crystal's non-homogeneity. It is hard to estimate the impact on the amplification process, as the crystal aperture is small and the day to day variations do not exceed 10-15 %. Afterwards, the hypothesis of the crystal's non-homogeneity was confirmed on the large aperture crystal, when testing a 25 mm $\times$ 25mm KTA for the high energy OPA experiments. More information about this test is provided in the Appendix 1.

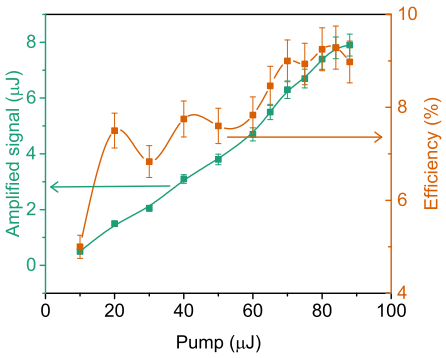

Figure 2.37 Power scaling with the highest efficiency of 9.3 % at the OPA3.

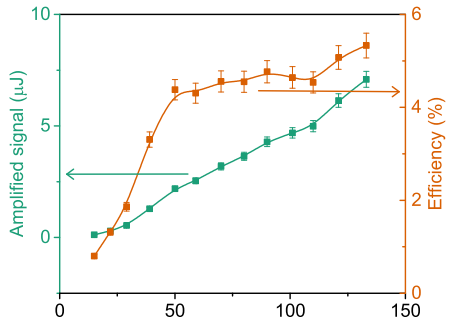

Figure 2.38 Reduced power scaling to the efficiency of 5.3 % at the OPA3 after 6 months of operation.

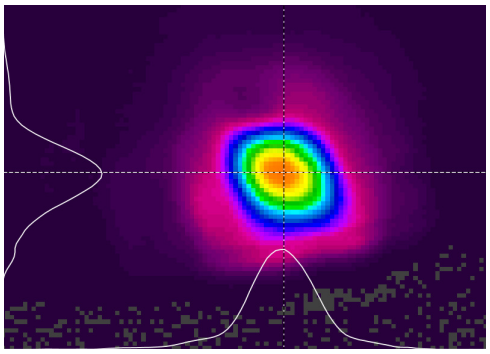

Figure 2.39 Beam profile at the output of OPA3.

Pulse duration

Pulse temporal characteristics were measured with a Second Harmonic Frequency Resolved Optical Gating (FROG) [126] device built in-house. The scheme of the set up is depicted in Fig.2.40.

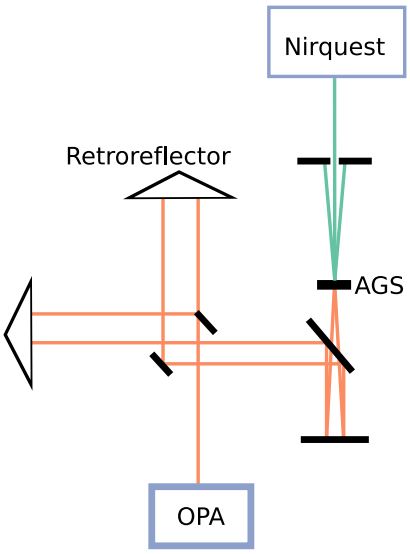

Figure 2.40 Scheme of FROG set up.

The input beam is split into two equal parts and sent into two retroreflectors. Here, the beam is split to two parts using a squared-shape mirror clipping half of the beam. This type of beam splitting was chosen, because a suitable beamsplitter for SWIR and MWIR region was not available in the laboratory. However, one should be careful to have a spatial-chirp-free pulses while using beam clipping to divide the beam. In our case, we didn't observe any spatial chirp, thus this beam splitting method could be considered reliable and should not impact the measurement of pulse duration. In the retroreflectors we change the height of the beams, so it is easier to recombine them. One of the retroreflectors is set on the automated translation stage, which allows us to find the time delay to overlap pulses and to perform the FROG scan. Afterwards both beams are combined in a second harmonic generation crystal and a sum frequency (SF) (vectorial second harmonic) is generated. A spectrogram of the SF signal is recorded and so a collection of spectra at different delay times is measured. Then, information about pulse temporal characteristics could be retrieved. For the information retrieval we use the Frog3 program (Femtosoft technologies). Measured and retrieved spectrograms are shown in Fig.2.41 and Fig.2.42. In our case the SH signal was generated in a 400 μm thick $AgGaS_2$ (AGS) crystal and the spectrograms were recorded with a NIRQuest 256 (Ocean Optics) spectrometer.

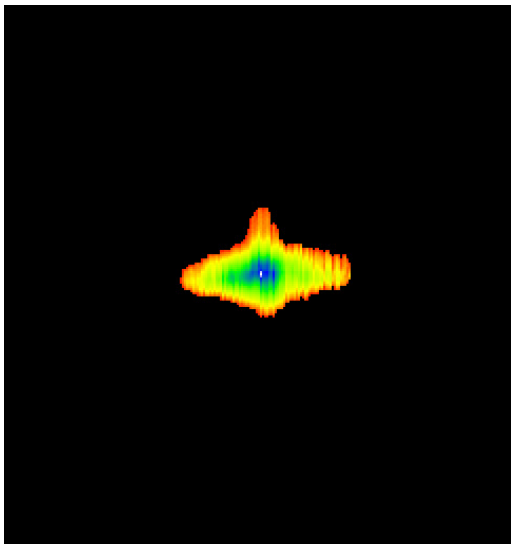

Figure 2.41 Measured FROG trace at the output of the OPA3.

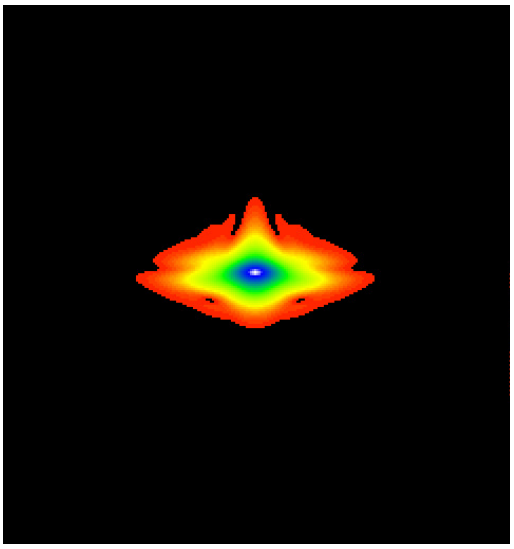

Figure 2.42 Retrieved FROG trace at the output of the OPA3.

When ultrashort pulses propagate through dispersive optical elements, they accumulate chromatic chirp. Their pulse duration is no longer Fourier transform limited. Furthermore, usually the seed signal is obtained through the white light continuum generation, which introduces a positive chirp. Afterwards, in the OPA, this chirp is transferred to the idler pulses, with an opposite sign. Thus, after the OPA, pulses should be recompressed. In the NIR spectral region, it is often done by a set of chirped mirrors or a grating compressor. Unfortunately, there is a lack of chirped mirrors operating in the SWIR and MWIR spectral region and the costs of existing gratings are very high. The most common and a rather simple method to compress pulses in this region is using bulk materials. Logically, that is the method we have chosen for the pulse compression after the OPA3. The summary of GVD of all the optical components in the seed/idler path is provided in Table.2.5.

Table 2.5 Summary of dispersion properties of materials in the path of seed/idler beams.

$\lambda, \mu m$	Material	Material length, mm	$GVD, fs^2/mm$	Total GVD, fs^2
1.65	YAG	15	-6	90
1.65	N-LAK22 + N-SF6	9 + 1.8	-25 + 24	-180
1.65	UFS	6	-40	240
1.65	KTA	6	17	100
1.65	N-BAF10 + N-SF6	5 + 2.5	-17 + 24	-25
1.65	PPLN	7.4	81	600
	Total:			**210**
3	Ge	3	1524	4570
3	KTA	10	-335	-3350
	Total:			**2045**

The sum of all the elements in the system corresponds to 2045 fs^2, which means that this amount of dispersion should be compensated at the output of the OPA. However, it does not take into account the positive chirp introduced into the signal pulses during the white light continuum generation. Unfortunately, we were not able to estimate the introduced chirp into the WLC. The theoretical estimations would require complicated simulations including different processes taking part in the WLC generation. The experimental measurement of pulse duration was also hardly feasible due to very broadband spectrum which complicates the requirements for ultra-broadband phase-matching conditions to perform FROG scans.

The optimal pulse compression was tested by inserting different materials into the 3 μm beam. This more detailed test was performed under lower pump power and tighter focusing conditions of the pump beam. When upgrading to higher power conditions, just the two points closest to the optimum points were checked to verify the validity. The results are provided in Fig.2.43. The shortest pulse duration is obtained when there is no additional material inserted, which means, that the pulse chirp is compensated for when passing through all the optical components in the system. The summary of materials used to post-compress the output of OPA3 and their properties is also provided in Table 2.6. There ϕ_2 is the added second order dispersion, ϕ_3 is the third order dispersion and τ_{pulse} is the pulse duration of compressed pulse with the inserted material at the output of the OPA.

Table 2.6 Summary of dispersion properties of materials used to compress the output of OPA3.

Material	ϕ_2, fs^2	ϕ_3, fs^3	τ_{pulse}, fs
4 mm YAG	-1108	7452	82
1 mm CaF_2	-92	507	69
2 mm ZnSe	340	846	70
5 mm ZnSe	850	1269	70
3 mm Ge	4782	9780	413
Nothing	-	-	62

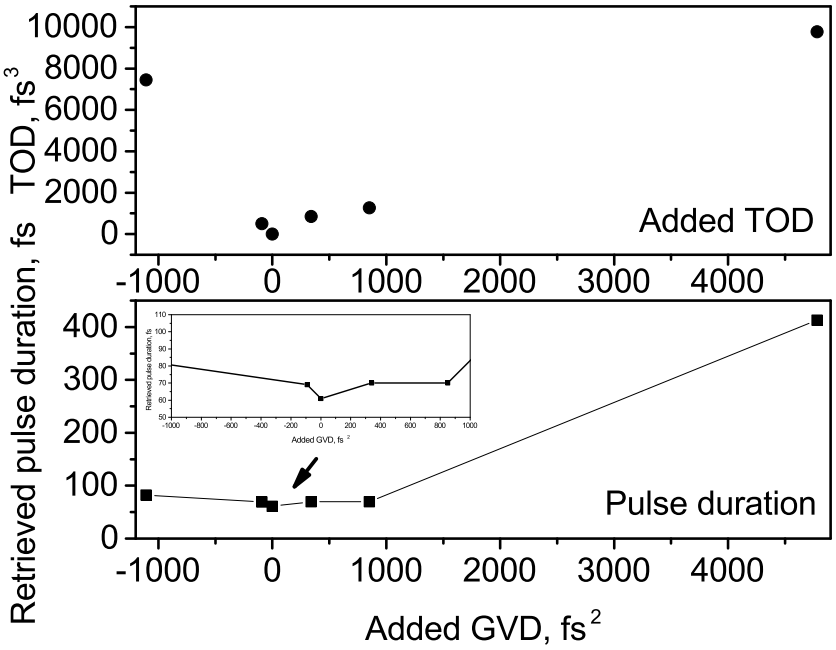

Figure 2.43 Optimization of pulse compression.

After the optimization of the amplification stage for the best compromise between power and duration, pulses of 85 fs (64 fs transform limited) have been obtained, the spectral and temporal characterization is shown in Fig.2.45. No material was used for the post-compression.

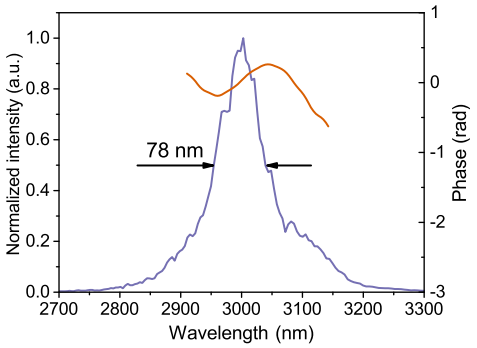

Figure 2.44 Spectral phase and amplified spectrum in the OPA3.

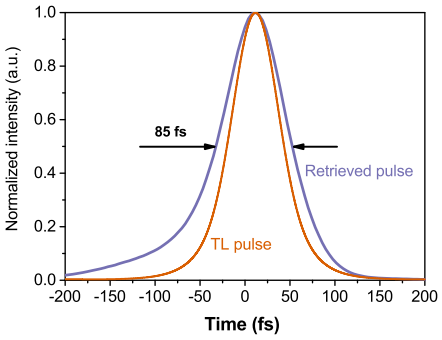

Figure 2.45 Retrieved temporal characteristics. Pulse duration is 85 fs (64 fs transform limited duration).

Summary of the 3 μm source

To sum up, the output of this OPA provided 8 μJ pulses at 3 μm, with a pulse duration of 85 fs. The Fourier transform limit is 64 fs. The summary of the performance of the OPA stages is provided in Table.2.7. This system features the WLC generation in a long media (15 mm YAG), which allows us to achieve direct amplification of the signal in the SWIR region. This leads to a simple scheme to passively stabilize the CEP. Two types of nonlinear crystals are implemented into the set up: bulk KTA and chirped PPLN. The advantage of the cPPLN crystal is the broadband amplification in a collinear configuration, thus generation of angular chirp free idler beam. Afterwards, KTA allows us to achieve high beam intensities without beam distortions or crystal damage in the last amplification stage. The system could be used for different applications, such as HHG in solids, WLC generation or testing new nonlinear crystals (LGT).

Table 2.7 Summary of 3 μm OPA performance.

Stage	**Crystal**	**Output wavelength,** μm	**Output energy**	**Efficiency**	**Gain**
OPA1	6 mm KTA	1.65	60 nJ	30 %	5000
OPA2	7.4 mm cPPLN	s: 1.65 i: 3	s: 2 μJ i: 0.75 μJ	4 %	33
OPA3	10 mm KTA	3	8 μJ	6.3 %	25

Comparing with other parametric sources operating at 3 μm it is worth noting a few systems developed by other groups: Rigaud et al. [119], Thiré et al. [89] and Baudisch et al. [7]. All of them are high average power OPAs operating at 100 – 160 kHz repetition rate.

The output power at 3 μm ranges between 8 and 40 μJ and pulse duration between 40 – 85 fs. All the systems are based on 1 μm pump lasers, however just ours and [119] is pumped with fs pulses generated in Yb doped fiber amplifiers. [89] and [7] are pumped by solid state lasers with the pulse duration respectively about 1.1 ps and 10 ps. In [89] the pump pulse duration still allowed generation of seed signal via supercontinuum generation in YAG crystal. However, in [7] pulses would have been too long to generate WLC, thus the seed was obtained through the DFG stage between the output of the 2-channel Er oscillator. A unique feature of our system is the previously mentioned combination of periodically poled and bulk nonlinear crystals. Other sources were based solely on periodically poled crystals. As it is noted in [124], one should be careful selecting the crystal length for the optimal amplification bandwidth and gain ratio. However, the gain narrowing could be overcome by using aperiodically poled (chirped) crystals. Also, the efficiency is increased by reducing the energy back-conversion from signal and idler to the pump beam. Hoping to achieve an improved performance, we have chosen to implement a cPPLN crystal into our OPA set up. After comparing the overall characteristics of these 3 sources, we could conclude that it was a rather good choice. A short summary is shown in Table.2.8. Despite the [89] system, which has an outstanding overall efficiency and pulse duration, our system has very similar characteristics to the other two. The key feature of improved performance of [89] is the acousto-optic programable dispersive filter used to select the WLC spectrum and shape the amplitude. Despite the fact that we used a uncoated Ge filter, which strongly attenuated seed signal for the OPA3, we still achieved slightly higher overall system efficiency compared to [119] and [7].

The use of KTA crystal in the last stage showed challenges of growing high quality homogeneous crystals. Zones with different efficiency were observed. Other teams developing SWIR/MWIR OPAs faced huge problems in extracting power from these crystals. Fortunately, the quality of the KTA implemented in our OPA stage was rather good and didn't vary more than 10-15 %. However, we were alerted of, and after performing tests confirmed the high non-homogeneity of large aperture crystals dedicated to the high energy experiments described in the next chapter.

Table 2.8 Summary of high average power OPAs at 3 μm.

Reference	Pulse duration, fs	Output energy, μJ	Overall efficiency, %
Archipovaite et al. [120]	85	8	2.8
Rigaud et al. [119]	72	10	2.3
Thiré et al. [89]	38	40	7.2
Baudisch et al. [7]	55	20	2

2.4 Implementation of new nonlinear crystal (LGT) into the SWIR and MWIR OPAs

The experiment described in this section was performed in a collaboration with the Optics and Materials group from Institute Neel, Grenoble, France. The suitability of new nonlinear crystal for performance in different parametric processes was tested. LGT ($La_3Ga_{5.5}Ta_{0.5}4O_{14}$) crystal is well known and used for its piezoelectric properties [127–129], but only recently it was discovered to be an interesting candidate for building MWIR OPAs [16].

During the last decade, the interest in parametric, ultrashort laser sources in the MWIR region has grown, the most common crystals used to generate signal in the region of 2-4 μm, using NIR pump laser, are BBO, BiBO, KTA, KTP, LBO, Mg:$LiNbO_3$ and PPLN. Unfortunately, PPLN has a low damage threshold and the size of crystal aperture is still limited to tens of millimeters, so despite its high d_{eff} the application is constrained. LBO, BBO and BiBO crystals have their transmission limited to 2.5 μm, so they are good for generating light in the SWIR region. For longer wavelengths, KTA and KTP could be used, as they are transparent up to 4–5 μm; the d_{eff} is similar and some efficient laser sources based on these crystals are reported [88, 121]. Nevertheless, new nonlinear crystals with higher damage threshold and extended transmission range supporting broadband phase-matching in the MWIR would boost the development of ultrashort laser sources in this region. Currently, shifting the wavelengths further into the MWIR requires using 2 μm pump laser sources [130, 131]. One of the interesting candidates for NIR pumped MWIR amplifiers is the LGT crystal.

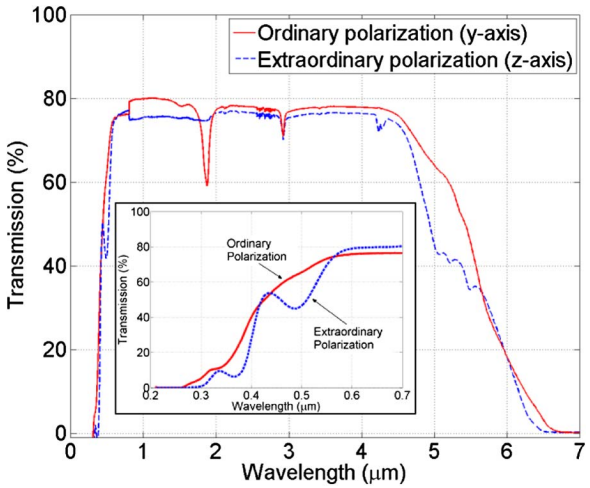

Figure 2.46 Transmission of the LGT crystal is extended into the infrared side and reaches up to 6.5 μm. Figure taken from [16].

.

As the crystal is widely used for its piezoelectric properties, the growing process by Czochralski method is well established and high quality: big aperture crystals could be produced (Fomos-Materials[132]). LGT has an extended transmission into the MWIR spectral side – it is transparent up to 6.5 μm (Fig.2.46), which makes it very interesting to study its implementation into the near-infrared-pumped OPAs. As was shown in the first chapter, LGT also features a high damage threshold of 33 TW/cm^2. Thus, taking into the account the possibility of growing large crystals and combining it with the high damage threshold, LGT seems to have a strong advantage compared to the currently used PPLN crystals, which are transparent up to 5.5 μm and also feature low damage threshold, but are difficult to grow at larger sizes. Thus, the question is whether the LGT crystal is capable of amplifying broadband spectra and what is the efficiency of this process.

In [133], it was shown that a very broad (1.4 – 3 μm) phase-matching could be achieved, if the crystal in type 1 configuration is pumped by 967 nm laser. However, the only laser sources at this wavelength are diode lasers – which either operate in the continuous wave regime or feature output power as low as hundreds of mW – which are not suitable to pump the ultrashort OPAs, our goal here. Even though one might argue that these wavelengths could be accessed by Ti:Sa laser, the efficiency is about two [134] to four [135] times lower compared to 800 nm. Thus other pump wavelengths and phase-matching conditions should be found to exploit the potential of the LGT crystal. Common pump sources for ultrashort OPAs and OPCPAs are Ti:Sa lasers at 800 nm and Yb or Nd doped laser gain medias lasing around 1030 or 1064 nm. The phase-matching curves for both cases are provided

in Fig.2.47 and Fig.2.48. We can see that in the case of 1 µm pump, we could generate relatively narrow (about 250 nm)spectrum at the degeneracy (2 µm region), which is already accessible with higher efficiency in BBO crystals. However, when Ti:Sa laser is used, we could expect to amplify 1.17 µm broadband spectrum in the vicinity of 4 µm. This would allow us to directly access the MWIR region, while pumping with the near infrared laser source.

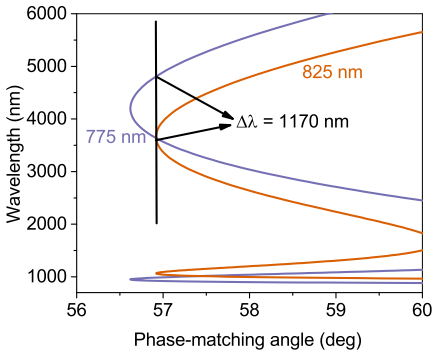

Figure 2.47 Phasematching curve for LGT crystal pumped by 25 fs Ti:Sapphire laser.

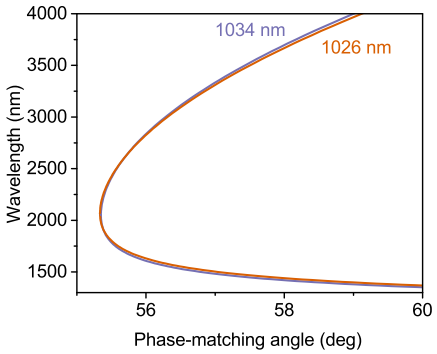

Figure 2.48 Phasematching curve for LGT crystal pumped by 1030 nm laser.

Initially, the experiment was designed to be performed on the Ti:Sapphire laser system "Aurore", featuring the following characteristics: 25 fs pulse duration, 1 kHz repetition rate and pulse energy of 10 mJ. An OPA in the short wave infrared was supposed to be demonstrated. Unfortunately, no parametric processes were detected before the white light generation and only a spectral broadening of the pump was observed (see Fig.2.49). The pump beam was focused to a 800 µm and the intensity was estimated to be 1.6 TW/cm^2, which also shows a high damage threshold of the crystal, which was afterwards confirmed by the LIDT (more information is provided in the first chapter). The absence of parametric amplification could have been caused by a few factors: due to lower repetition rate and much smaller amplification gain compared to the BBO crystal, the detector sensitivity was too low to capture the signal gain.

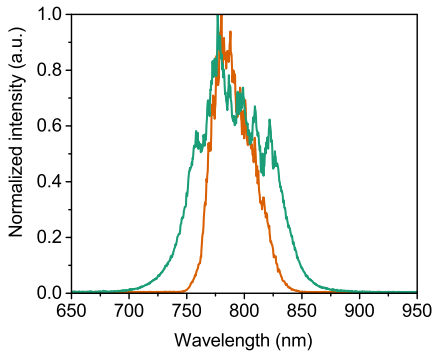

Figure 2.49 Spectral broadening of pump beam in the LGT crystal. Orange - spectrum of Aurore laser, green - broadened spectrum of Aurore.

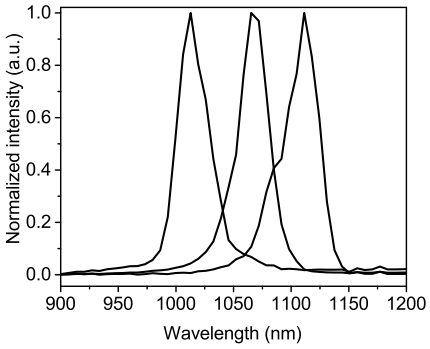

Figure 2.50 Second harmonic generated in LGT crystal. Different spectra generated by changing the phasematching angle.

As the reasons why it was not possible achieve parametric amplification in the LGT sample were not clear, it was decided that we would verify its ability to generate the second harmonic. There is no phase-matching for 800 nm or 1030 nm, the only available laser source suitable for the SHG was the previously described 2 µm OPA. Indeed, it was possible to measure the SH signal (Fig.2.50), which confirms that the crystal features a second order nonlinearity and the cut angle is as indicated and should be suitable for the OPA. Afterwards the LGT crystal was placed in the DFG stage of the 2 µm OPA.

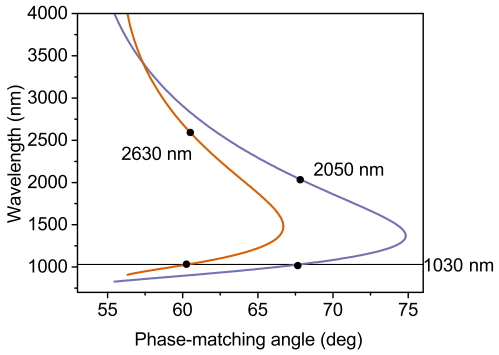

Figure 2.51 Phasematching curves for LGT crystal pumped by broadband pulses at 700 nm. The two curves are for the extreme pump wavelengths 685 and 740 nm.

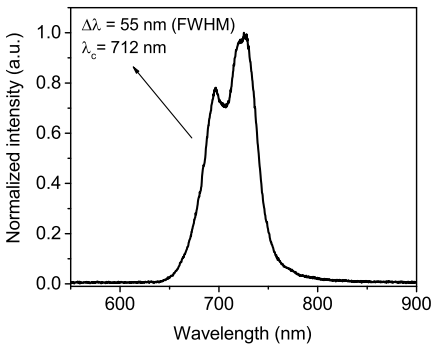

Figure 2.52 Spectrum of pump pulses of the DFG stage.

As it is seen in Fig.2.48, the spectrum of generated idler is not as broad as one might assume from the phase-matching curve in Fig. 2.47. This is because the optimal phase matching conditions could not be fulfilled. The signal wavelength is fixed (fundamental pump at 1030 nm). All the tunability depends on the pump spectrum and phase matching angle, thus, not the broader curved part, but the slope of the phase matching curve was examined. The margins of the accessible part of the phase-matching curve are indicated by black dots in Fig.2.51. Spectrum of the pump is depicted in 2.52. By turning the crystal angle, we can tune the generated DFG spectrum between 2050 and 2630 nm. It was indeed achieved during the experiment (Fig.2.53). To tune the central wavelength from 2050 nm to 2630 nm, the crystal was tilted by 17.5 deg. Pump power was 500 mW and signal at 1030 nm was 14.5 W, the generated idler didn't emerge from the background noise of the power meter (1-2 mW). So the efficiency of this process was very low in comparison with BBO, where the generated idler was 30 mW. The d_{eff} for BBO crystal is 1.97 pm/V, and the d_{eff} of LGT crystal is 0.47 pm/V, thus about 4 times lower than in BBO. When the DFG process is simulated with SNLO, the generated irradiance in BBO crystal is 63 times higher than in the case of LGT. We could expect the idler beam to be 0.5 mW, which is under the detection range of the power meter used. So, even though the LGT crystal seems to be a promising media, the efficiency problem should be further investigated before implementing this crystal into the MWIR OPA systems built for experiments that require high power, intense laser sources.

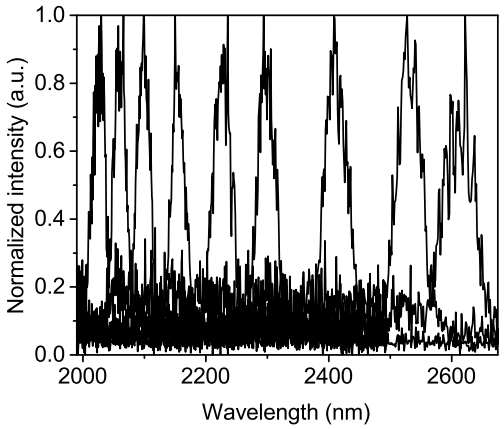

Figure 2.53 Tunable spectra of the idler of the DFG stage, tunability achieved by changing the phasematching angle.

In order to further investigate the performance and applicability of the LGT crystal, it was implemented into the 3 μm OPA scheme. The collinear configuration is more favorable

to amplify broadband signal, thus the LGT crystal was placed in the second stage with the pump beam blocked for the first stage. The WLC is being amplified. The amplified spectrum is shown in Fig.2.54 and the corresponding idler in Fig.2.55. As it is seen from Fig.2.56 the phase-matching curve is rather steep for the 1030 nm pump. Thus a broadband spectrum amplification should not be expected. Pump energy is 80 µJ and the power of the amplified signal is yet again under the detection range of the power meter.

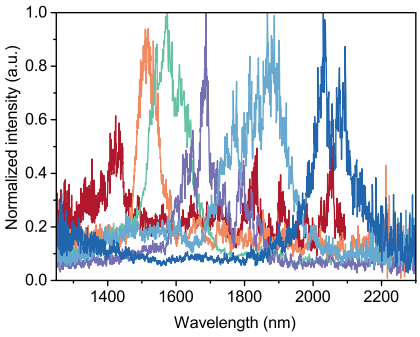

Figure 2.54 Amplified signal with the removed WLC signal from the background, tunability achieved by changing the phase-matching angle.

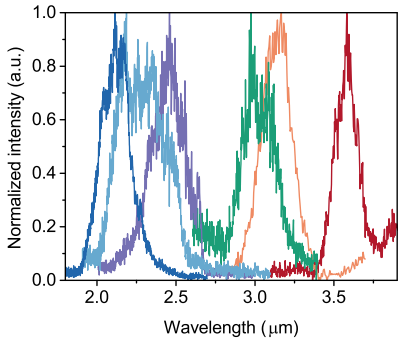

Figure 2.55 Spectrum of idler pulses corresponding the signal in Fig.2.54,tunability achieved by changing the phasematching angle.

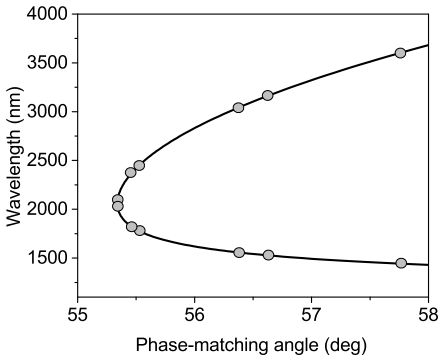

Figure 2.56 Phasematching curves for LGT crystal pumped by Yb:FCPA. Dots mark the experimentally measured wavelengths.

To sum up, three parametric processes (second harmonic generation, difference frequency generation and parametric amplification) in a LGT crystal were demonstrated in a high power Yb:FCPA pumped 2 and 3 µm OPAs. The exploited configurations were not the optimal for generating the ultra-broadband spectra, but the ultra-broadband phase-matching was not

accessible with the available wavelengths. The amplification efficiency was very low in comparison with the conventionally used BBO and PPLN crystals in these OPAs. This leads to the conclusion that the LGT crystal is not yet suitable for implementation into high average power, ultrashort mid-wavelength infrared OPAs. As just one crystal sample was available for the test, a further investigation with different crystal samples should be performed before drawing the final conclusions.

Even though the LGT crystal does not seem to be applicable for high average power OPAs, it might be an interesting candidate for high energy systems. Its high damage threshold and its capability to grow large aperture and high quality crystals could compensate for the lower d_{eff}. One of the limiting factors for power scaling in PW systems is the damage threshold of the crystal. In order to reduce the pump intensity on the crystal, the beam size should be increased. And here the crystal size becomes a limiting factor. At the moment, just DKDP and KDP are the reliable and commercially available crystals with apertures of tens of centimeters. LGT crystal aperture could reach 10 - 15 cm, almost 10 times larger than BBO, whose size is limited to few cm. Thus, it could be interesting to test the LGT in a high energy OPA.

Chapter 3

High energy parametric sources in SWIR and MWIR

The experiments described in this chapter were conducted in a collaboration with Andrius Baltuška group and took place in Photonics institute in Vienna Technical University (TU Wien). The laser source in TU Wien is also based on Yb amplifiers, but instead of using fiber technology, it is based on Yb:CaF_2 bulk crystals. In comparison to Solstice, the laser source at CELIA, the Yb:CaF_2 regenerative amplifier at TU Wien features a lower repetition rate of 500 Hz (compared to 100 kHz); much higher energy pulses with 14 mJ (compared to 400 µJ), and a pulse duration slightly shorter with 220 fs (compared to 350 fs) of the Yb:FCPA.

3.1 Yb:CaF_2 Pump laser

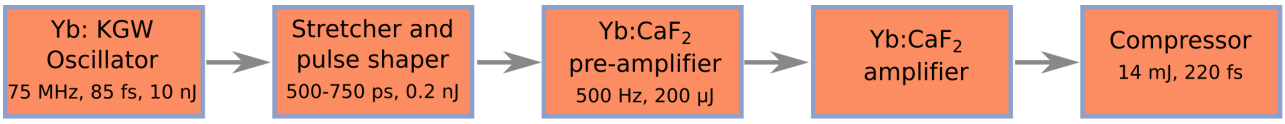

Figure 3.1 Yb:CaF_2 pump laser scheme.

The pump laser for the following experiments was a femtosecond regenerative Yb:CaF_2 amplifier. The system consists of Yb:KGW oscillator (Pharos, Light Conversion), regenerative pre-amplifier and the main regenerative amplifier. The oscillator works at a 75 MHz repetition rate, the pulse energy is 10 nJ and pulse duration 80 fs. Before sending the signal into the pre-amplifer, pulses are stretched up to 500-750 ps and the spectrum is reshaped in order to avoid crystal damage and compensate for the gain narrowing occurring during the

amplification process. The transmission of the stretcher and pulse shaper is about 2 %, thus the seed for the pre-amplifier is 0.2 nJ. The pre-amplifier is operating at 500 Hz and amplifies the signal up to 200 µJ. Then, the signal is sent into the main amplifier, where it is amplified up to 15.5 mJ. The compressor's efficiency is over 90 %, thus at the output of the laser we have pulses with the energy of 14 mJ. The pulse duration of compressed pulses is 220 fs. (See the spectrum in Fig.3.2 and temporal pulse profile in Fig.3.3). This laser source is either used to pump the tunable OPA system, or is post-compressed in a hollow core fiber and used for strong field experiments, such as high harmonic generation in gas (see Section 4.3).

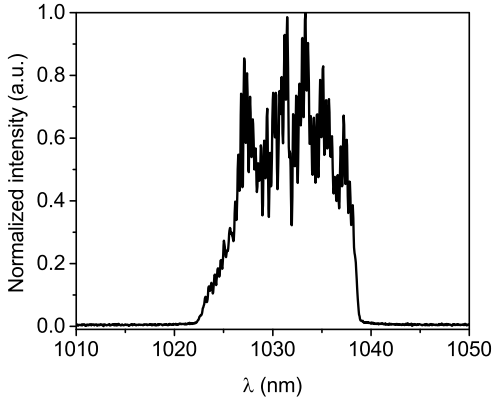

Figure 3.2 Spectrum out of the Yb:CaF_2 amplifier at 14 mJ.

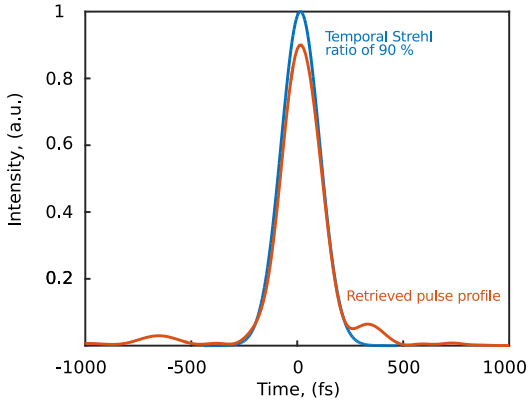

Figure 3.3 Temporal pulse profile.

In Fig.3.3 we show a temporal pulse profile with 220 fs pulse duration and Gaussian pulse profile with the same pulse duration and integrated pulse energy as the measured pulse. The Frog trace is also depicted at the inset. We can also see that a part of pulse energy is in the wings of the pulse. After comparing the integrated measured pulse profile with the corresponding Gaussian profile, we could estimate that 90 % of the pulse energy is in the main pulse. Energy losses in the wings reduce the pulse peak power, which after the energy corrections is 57 GW.

The repetition rate of the regenerative amplifier could be adjusted and increased up to 2 kHz. However, the group has experienced that the stability of the laser is improved if operating at 500 Hz. Amplifier operating at lower repetition rate is further from the energy bifurcation regime observed in [136, 137]. During the experimental campaign of HHG driven by post-compressed Yb:CaF_2 pulses, we have increased the repetition rate to 2 kHz and reached an output power of 28 W, while keeping the same level of pulse energy. Unfortunately, due to increased thermal effects and damage probability we could not use it

for our experiment (see more on challenges faced in the high power regime in Subsection 4.3).

3.2 1.8 μm and 2.4 μm OPAs

State of the art of high energy SWIR OPAs

Table 3.1 State of the art of 2 μm OPAs.

Ref.	λ, μm	Energy, mJ	Rep. rate, kHz	Pulse duration, fs	Nonlinear crystal	Pump laser	CEP stable?
[69]	2.1	1.2	3	15	MgO:PPLN	Yb:YAG	Yes
[114]	1.8	2.5	1	–	BBO	Ti:Sa (TOPAS)	NA
[88]	3.9	25	20 Hz	85	KTP KTA	Nd:YAG	No
[71]	2.4	1.2	0.5	115	KTA	$Yb:CaF_2$	Yes

Systems depicted in the Table.3.1 stand out from all the other SWIR OPAs from the Table 2.2 due to their high energy output pulses. The high energy here is defined as pulse energy higher than 1 mJ. These four systems are very different, starting from the pump lasers to the nonlinear crystals used. The system in [69] was pumped by a thin disk Yb:YAG laser with the pulse duration of 1.6 ps. The other two systems are based on fs pump lasers – 220 fs Yb:CaF_2 in [71] and Ti:Sa in [114], the latter is a commercially available TOPAS. Also, the systems were based on different crystals: PPLN, LN, KTA and BBO. As it was already mentioned in the previous chapter, periodically poled crystals have a rather low damage threshold, thus, even though they provide broadband and efficient amplification in the first OPA stages, for the power amplifier a bulk crystal is necessary to handle the intensity. This was the case in [69], the larger aperture PPLN was not available for the last amplification stage, thus a bulk LN crystal was used. KTA crystals compared to BBO ones have an extended transmission range into the infrared. Thus the wavelength tuning range is also broader and could reach up to 4 μm [88], while BBO is limited at 2.5 μm. The source described in [88] stands out from other MWIR OPAs. This OPCPA is pumped by flash-lamp-pumped Nd:YAG laser system and is operating at lower repetition rate – 20 Hz, but the pulse energy of generated MWIR signal is very high – 25 mJ. Also this source is operating at longer wavelengths when the spectrum is centered at 3.9 μm.

The tunable OPA centered at 1.8 μm and 2.4 μm

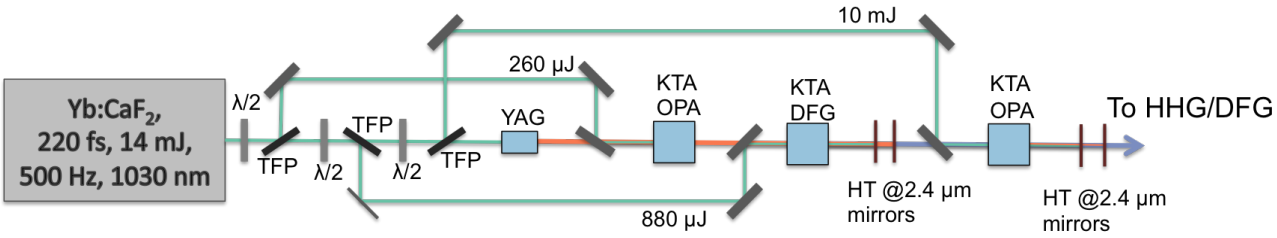

Figure 3.4 The three-stage OPA set up.

The set up of the three-stage tunable OPA is depicted in Fig.3.4. The system is similar to the one described in the previous chapter, but here all the amplification stages are in collinear configuration and all the stages are based on KTA crystals. Also, the availability of dual-band high reflectivity dielectric mirrors in the Mid-IR allows it to reach high efficiency and use both signal and idler beams after the last amplification stage.
The signal to seed the parametric amplifiers is generated via white light supercontinuum generation in a 8 mm YAG block from a small fraction of laser pulse energy. The generated WLC covers the wavelength range up to 2 μm (Fig.3.5).

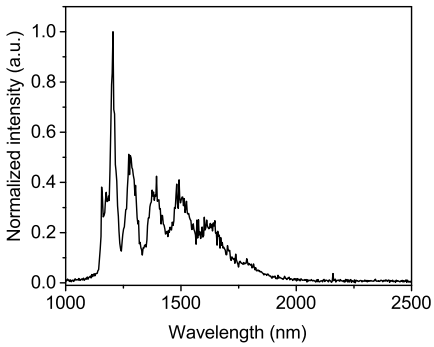

Figure 3.5 White light continuum generated in 8 mm YAG rod.

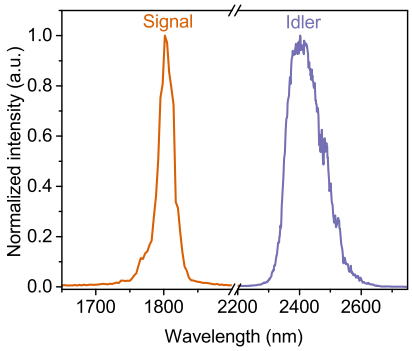

Figure 3.6 Signal centered at 1.8 μm and idler at 2.4 μm at the output of the KTA-OPA.

The first two stages of KTA-OPA are identical: the WLC spectrum around 1.8 μm is collinearly amplified in the 5 mm crystals. Afterwards, the idler beam at 2.4 μm is selected by using a pair of dielectric mirrors and amplified in the third, 4 mm length KTA crystal. In the last stage a large aperture KTA as described in Appendix 1 was implemented. The overall conversion efficiency from the pump laser to the signal and idler output of the OPA is 25%. The total energy of both signal and idler beams is 3 mJ; 1.7 mJ (peak power 10 GW) for the

signal and 1.3 mJ (peak power 10 GW) in the idler beam. The pulse duration right after the OPA of the signal is 165 fs and for idler is 123 fs, (see temporal pulse profiles in Fig.3.8). The corresponding transform limit durations for the generated spectral bandwidth are 150 fs and 60 fs, which corresponds to 26 and 8 optical cycles. Due to the narrow phase-matching conditions (Fig.3.7), the signal spectrum is narrow (30 nm), which leads to multiple-cycle pulse duration. In order to increase the amplification bandwidth, a non-collinear scheme should be implemented, but in that case the generated idler beam would be angularly dispersed. As both beams are used after the OPA, the angular dispersion together with the pulse front tilt are to be avoided. In this case as it would impact the beam focusability, and so would also limit the intensity on the target. The summary of parameters of each of the OPA stages are provided in Table.3.2.

Table 3.2 Summary of the KTA-OPA performance.

Stage	**KTA Crystal**	**Output wavelength**	**Pump energy**	**Output energy**	**Efficiency**
OPA 1	5 mm	1.8 µm	260 µJ	8 µJ	3 %
OPA 2	5 mm	2.4 µm	440 µJ	80 µJ	9 %
OPA 3 signal	4 mm	1.8 µm	10 mJ	1.7 mJ	14 %
OPA 3 idler	4 mm	2.4 µm	10 mJ	1.3 mJ	10%

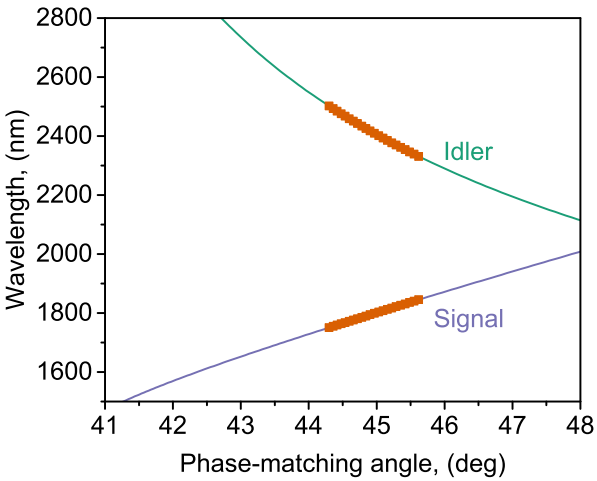

Figure 3.7 Phase-matching curve for collinear KTA-OPA. The region of interest is marked in orange.

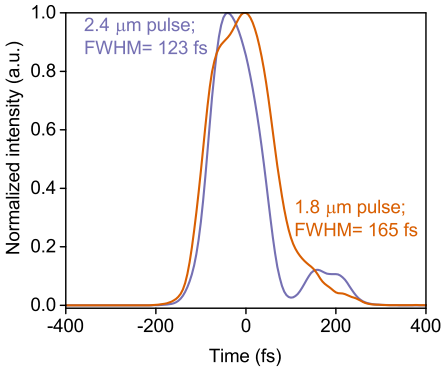

Figure 3.8 Retrieved from FROG temporal pulse profiles of the 165 fs signal and 123 fs idler at the output of the KTA-OPA.

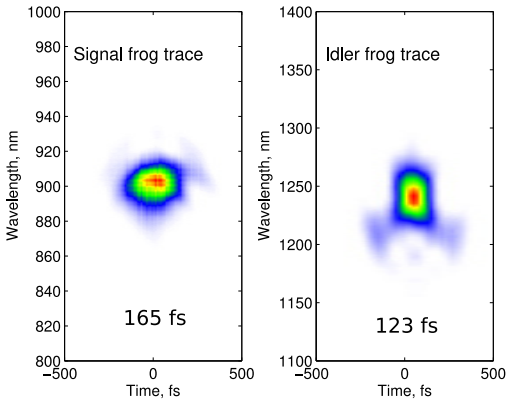

Figure 3.9 Retrieved FROG traces of signal and idler beams.

3.3 DFG in AGS

Sources in the mid-wavelength and long-wavelength infrared

Laser sources in the mid-wavelength infrared (3-8 μm) and long-wavelength infrared (8-15 μm) spectral region have a large variety of applications in spectroscopy where many molecules and their functional groups have their vibrational and rotational resonances in this spectral region, such as acetone (8.2 μm), ozone (9.2 μm), ethanol (10 μm) [7]. This wavelength region is covered by semiconductor [4], quantum cascade lasers [138] and optical parametric oscillators [139]. However, only travelling wave parametric amplifiers allow the generation of energetic ultrashort pulses in the mJ level range [11]. The MWIR pulse generation relies on the availability of transparent nonlinear crystals, typically non-oxide semiconductors [140]. The most common way of generating intense femtosecond pulses in this region is either directly via intra-pulse difference frequency generation starting from a single broadband NIR pulse [141, 142] or via cascaded two-stage parametric down-conversion [143–145]. In [141], an intrapulse DFG system based on LGS crystal is pumped by a post compressed Yb:YAG thin disk oscillator, generating 103 mW (1 nJ), and 66 fs pulses covering the spectrum range from 6.5 μm to 16.8 μm. An intrapulse mixing of and output of 2 μm OPA in AGS crystal provided 2 μJ (2 mW) 85 fs pulse [142]. Previously reported optical parametric amplification (OPA) systems followed by difference frequency generation (DFG) between signal and idler beams are mostly based on Ti:Sapphire laser pump sources [143]. The MWIR nonlinear crystal is directly pumped by the NIR laser [144, 145], but then the wavelength range of generated pulses is limited to 5-7 μm. More recently, optical

chirped pulse amplification (OPCPA) in the 6-7μm range in a ZGP crystal pumped by 2 μm picosecond pulses from a holmium CPA [131, 130, 75] was explored, however it relies on complex and not yet mature holmium laser technology. MWIR pulse energy in [130] was 40 μJ and in [131] – 200 μJ. However, in [131, 130, 75] systems, shorter wavelengths are reported (spectra centered at 5–7 μm). With our system, we achieve comparable pulse energy with the pulse spectrum centered at 8.5 μm.

MWIR DFG driven by signal and idler waves of SWIR OPA

The signal and idler beams of the OPA are split in an interferometer composed of dichroic beam splitters. Then, the two pulses are mixed in a 5 mm AGS crystal resulting in the generation of the broadband mid-IR pulse tunable in the 5-11 μm range. The divergence and beam sizes of the two beams are adjusted by setting up a pair of telescopes, the beam sizes at the AGS crystal are set to be 9 mm. The intensity of the signal beam is 16 GW/cm^2 and for the idler beam 13 GW/cm^2. The DFG stage configuration is close to collinear. A small angle of 0.2 deg is kept in order to ease the separation of the DFG signal from the signal and idler beams. However, the angle is too small to induce an angular chirp.

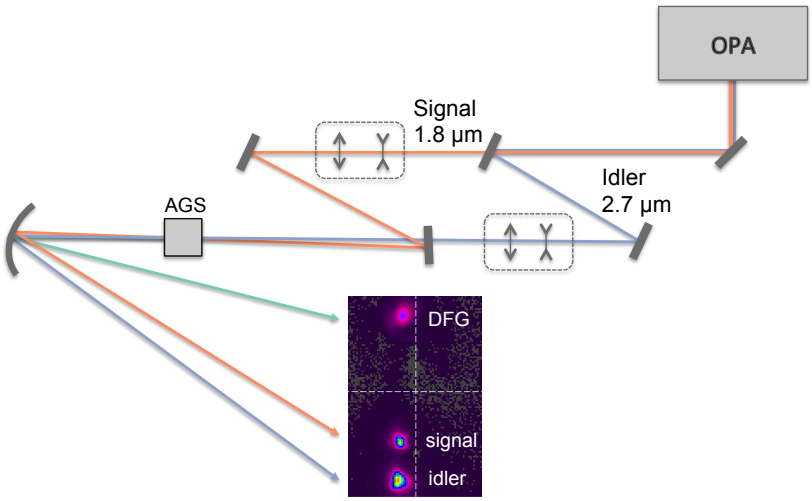

Figure 3.10 Signal and idler beams are mixed in the AGS crystal to generate DFG signal in the Mid-IR.

76 % of total OPA output is delivered to the DFG stage resulting in 2.3 mJ of pump and signal input. The maximum recorded DFG pulse output energy of 0.15 mJ is obtained at 8.5 μm wavelength, where the group velocity mismatch between the three waves is minimal and

the signal supposedly not affected by the water absorption in the atmosphere. The conversion efficiency in this AGS DFG stage is 6.5 %. In Fig.3.11 we have plotted the broadest spectrum obtained after 1 m of free propagation.

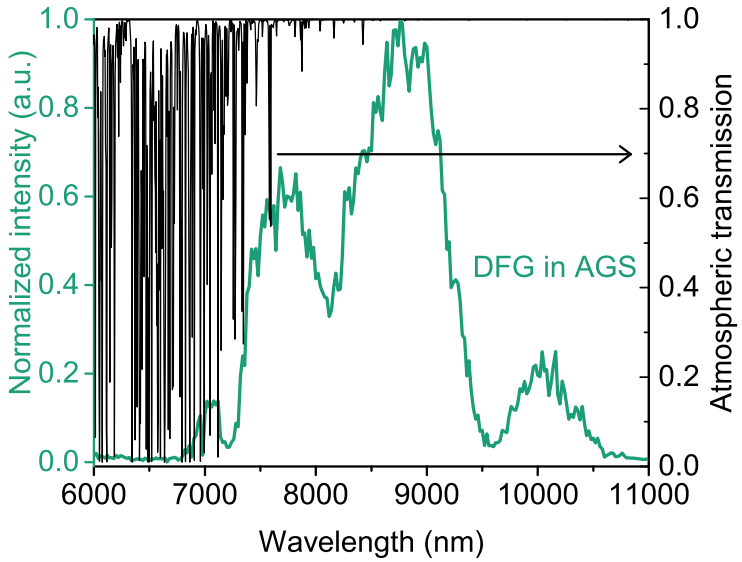

Figure 3.11 Spectrum centered around 8.5 µm. Black line is the transmission through one meter of atmosphere (transmission data taken from Hitran database [17].

The generated DFG beam is separated from the 2.4 µm and 1.8 µm beams via spatial filtering in the Fourier plane. All three beams, after the DFG stage, are focused with a spherical mirror with the ROC of -1000 mm. The image of the beam's distribution in the focus is shown in Fig.3.12. The DFG signal is propagating with a significantly larger angle compared with signal and idler beams. The ratio between the angles of signal-idler and signal-DFG is $\approx k_{\text{idler}}/k_{\text{DFG}} = 3.3$, which allows a simple DFG signal selection by blocking the other two beams with a hard aperture or a beam block. The set up is simple, compact and allows us to cross signal and idler beams in the crystal at small angles. Otherwise the noncollinear beam separation would require impractically long distances for the beams to separate or large noncollinearity angles that would limit the pulse front overlap on the crystal and introduce the angular chirp on the generated DFG signal. Using dichroic mirrors or high-pass filters is also challenging because transparent materials in this spectral range are typically highly nonlinear semiconductors, which might exhibit a low damage threshold or introduce beam distortions on the generated infrared signal, especially at the high intensities, which were used in this experiment.

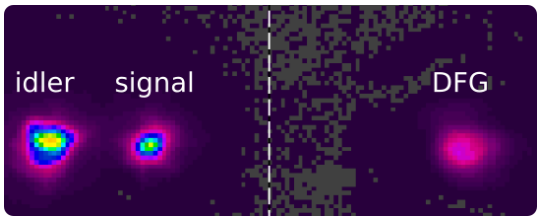

Figure 3.12 The idler, signal and DFG beam profiles (from left to right) at the focus.

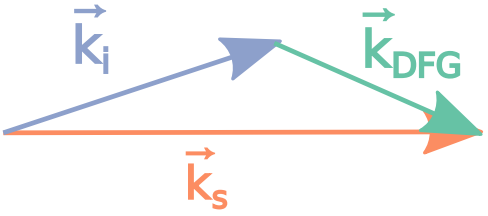

Figure 3.13 k vectors representing the DFG process in AGS crystal.

Tunability

The central wavelength of the DFG pulse is continuously tunable in the 5-11 µm range by adjusting the phase matching angle θ_{pm} and the central wavelengths of the signal and idler waves respectively. The tunability is possible as long as the relation between the OPA wavelengths and the DFG wavelength stage is defined as following:

$$\omega_L = \omega_s + \omega i \tag{3.1}$$

$$\omega_s = \omega_{DFG} + \omega i \tag{3.2}$$

Here ω_L is the pump laser frequency and ω_{DFG} is the diference frequency between signal and idler of the OPA pumped with the pump laser of a frequency ω_L. For a constant laser pump wavelength, a pair of signal and idler beams is generated. Later the same wave pair is mixed in the AGS crystal to generate the DFG signal. Fig.3.14 shows the signal-idler wavelength combinations and the corresponding DFG wavelength. Fig.3.15 shows the phase-matching curve for the DFG process. The phase-matching curve is flat at around 9 µm, allowing the generation of a broadband DFG signal. Luckily enough, this region corresponds to an atmosphere transparency window. The increase of the spectral bandwidth is also illustrated by the calculated gain curves as shown in Fig.3.16.

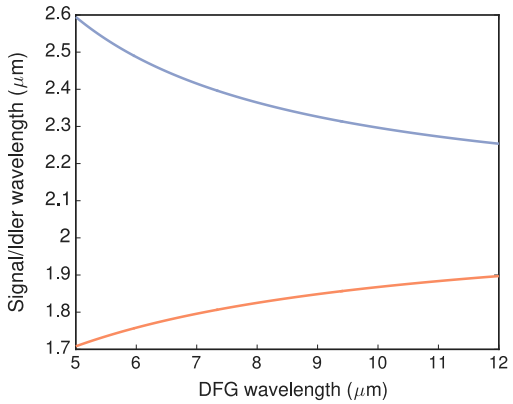

Figure 3.14 Signal and idler wavelengths for a corresponding DFG wavelength generation.

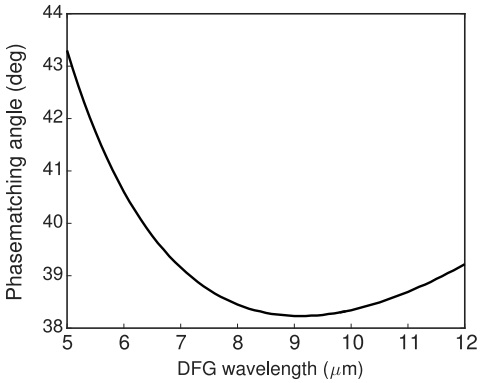

Figure 3.15 DFG phasematching curve around 9 μm.

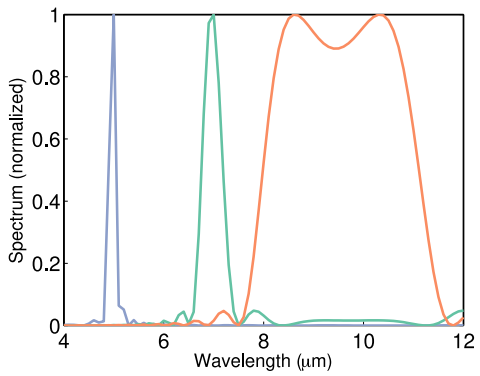

Figure 3.16 Gain curves simulated for the DFG signal centered at 5 μm, 7 μm and 9 μm.

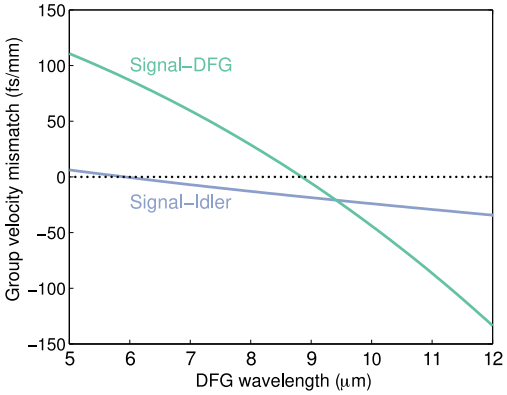

Figure 3.17 GVM in the region of 9 μm.

The group velocity mismatch (GVM) is another parameter in favor of generating wavelengths in the long wavelength infrared spectral range in the AGS crystal. The GVM is low in this region (see Fig.3.17), which allows us to use longer crystals and achieve higher efficiency, while keeping the generated DFG signal short.

Fig.3.18 illustrates the tunability of DFG central wavelength. Strong absorption lines around 6 μm due to water absorption in the atmosphere are observed. The widest spectrum is achieved when the DFG is generated around 8.5 μm (Fig.3.11). There we also show the transmission spectrum through 1 m of air. The left part of the measured MWIR spectrum falls under the strong absorption region. However, the spectrum does not seem to be affected by absorption. Comparing Fig.3.11 and Fig.3.18 we could see that indeed the signal noise in

Fig.3.11 is rather constant and does not show sharp and deep absorption lines as in Fig.3.18. As aforementioned, the broadest spectrum is around 8.5 µm due to the reduced group velocity mismatch between the DFG and the signal and idler pulses in this spectral range and the favorable phase-matching conditions.

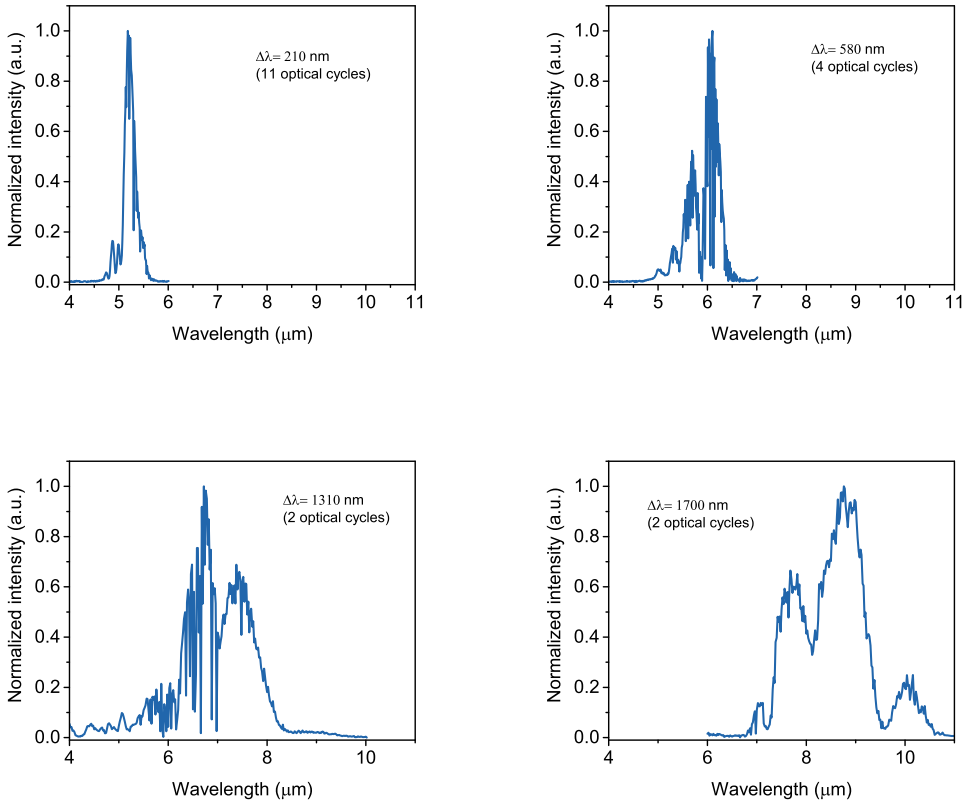

Figure 3.18 DFG spectra tuned to different central wavelengths.

Future applications

This source readily allows reaching sufficiently high intensities to perform strong field experiments with modest focusing conditions. For example, when focused into a $\approx 100\,\mu m$ spot using a $f = 10\,cm$ lens and $d = 10\,mm$ input beam diameter (NA=0.05) one can achieve an intensity of $> 10^{13}\,W/cm^2$. The DFG pulse duration is estimated to not to be longer than pump pulse (165 fs). Thus, this MWIR source is a promising tool for HOH generation in solids (for instance ZnSe or ZnO) in order to study the band structure. Also with the longer driver we expect to reach higher harmonic cut off energies as predicted by the $I \times \lambda^2$ law.

Comparison with Ti:Sapphire pump laser

Most common pump sources for ultrashort OPAs are Ti:Sapphire lasers, emitting at 800 nm, and Yb or Nd based lasers, emitting around 1 μm. Even though Ti:Sa lasers are well developed and reliable sources we use every day, they have low wall-plug efficiency. On the other hand, DPSSL, such as $Yb:CaF_2$, are quickly developing and capable of delivering multi-mJ pulses at repetition rates of multi-kHz. $Yb:CaF_2$ lasers are pumped with diode lasers, they feature lower quantum defect, and also exhibit higher wall-plug efficiency. However, most of the MWIR parametric sources are based on Ti:Sapphire pumped SWIR OPAs and DFG mixing. It is interesting to compare the performance of difference frequency mixing in the MWIR spectral region in AGS crystal, when system is pumped by 800 nm and 1030 nm laser.

The DFG signal in the MWIR is generated between the signal and idler beams of the SWIR OPAs. The corresponding signal and idler wavelengths of SWIR OPAs pumped by 1030 nm and 800 nm to generate DFG signal in MWIR are depicted in Fig.3.19 as a function of DFG wavelength. Here we could see, that signal and idler beams generated by 800 nm pump have shorter wavelengths. MWIR crystals feature high to very high non-linear refractive index. Additionally, the critical power varies inversely proportional to the index and scaling as λ^2. Thus, longer driving wavelengths are to be preferred to reach higher intensities. Furthermore, for AGS with a bandgap energy of 2.73 eV, in the case of Ti:Sa pump, signal wavelengths lie close to the three-photon absorption limit, while signal generated by 1030 nm pump is closer to a four-photon absorption, where the multi-photon absorption probability is much lower.

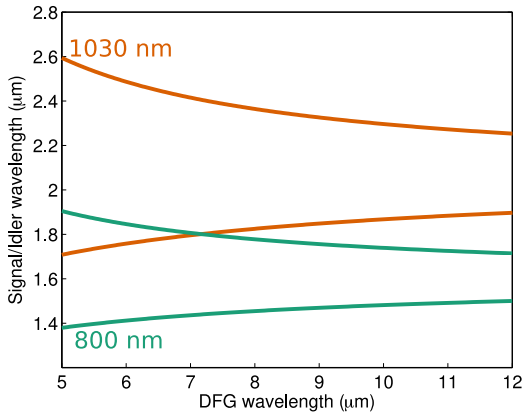

Figure 3.19 Signal and idler wavelengths for a corresponding DFG wavelength generation when system is pumped by 800 nm and 1030 nm lasers.

The phase-matching curves for both pumps in the AGS crystal are depicted in Fig.3.20. The phase-matching curve features a steeper slope for 800 nm, which limits the generation of broadband DFG signal. So, the phase-matching conditions are more favorable for the 1030 nm pump. It is also confirmed by the amplification gain curves (Fig.3.21). DFG pulses at 9 μm generated by mixing the output of the Ti:Sapphire pumped OPA at 1.469 μm and 1.756 μm are expected to be 2.5 times narrower (Fig. 3.21) for the same crystal length (5 mm) as compared to the case of 1030 nm laser pumped OPA (1.848 μm and 2.326 μm). Even though, a broadband DFG signal could be expected at longer wavelengths (11-12 μm), for 800 nm pumping the AGS crystal is not transparent in that spectral region.

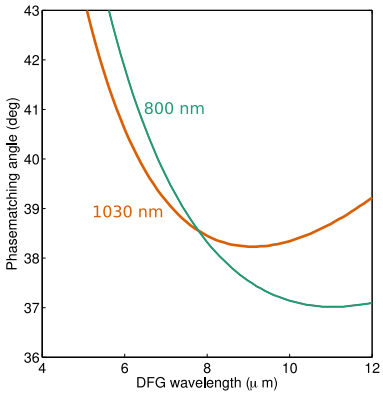

Figure 3.20 The phase-matching curves for the DFG in AGS crystal pumped by 800 nm and 1030 nm laser.

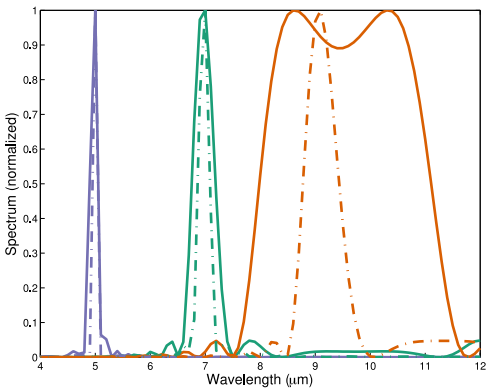

Figure 3.21 The gain curves for the DFG signal centered at 5 μm, 7 μm and 9 μm when system is pumped by 800 nm (dashed) and 1030 nm (solid) laser.

As aforementioned, GVM is an important parameter when ultrashort pulse generation is considered. Lower GVM allows using longer crystals, leading to the potential of decreasing the beam intensity to achieve the same efficiency as in a short crystal, avoiding beam distortion due to induced nonlinear processes. The GVM between signal and idler and between signal and DFG signal for both pumps is shown in Fig.3.22. At the optimal phase matching conditions for 1030 nm pump we also have the lowest GVM.

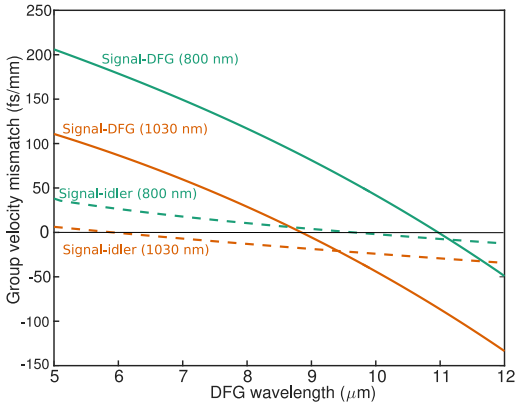

Figure 3.22 The GVM for 800 nm and 1030 nm pump lasers.

To sum up, 1030 nm pump lasers show advantages to generate broadband ultrashort pulses in MWIR spectral region in AGS crystals. Difference frequency mixing features broader phase-matching conditions and lower group velocity mismatch. Furthermore, the

critical power for the parasitic processes of higher nonlinearities would be higher; the crystal could stand more intense pump beams before the beam distortion would appear. Finally, the efficiency of our system is about 5 times higher than commercially available TOPAS [62].

Chapter 4

Experiments

The experiments described in this chapter took place in CELIA laboratory at University of Bordeaux and Photonics institute in Vienna Technical University (TU Wien). Experiments presented here are the applications of parametric sources described in the previous chapter. High repetition rate 3 μm OPA was used to generate HHG in solid and high energy SWIR OPA at 1.8 μm and 2.4 μm was used for HHG in gas, also HHG was driven by a post-compressed 1 μm laser.

4.1 HHG in ZnSe driven by high repetition rate MWIR OPA

As it will be shown later in this chapter, even high energy SWIR OPAs are not sufficiently reliable HHG drivers to efficiently generated harmonics in gas. Experiments of HHG in gas are even more complicated, when drivers working at higher repetition rates with a lower pulse energy are used. On the other hand, HHG in solids require lower intensities, so high repetition rate SWIR and MWIR OPAs are attractive sources to drive these experiments. To generate HHG in ZnSe, we used the Yb:FCPA pumped 3 μm OPA described in Chapter 2.

The 3 μm beam at the output of the high repetition rate OPA, the amplified signal is collimated to a beam size of 2 mm. It is then focused with a -200 mm ROC silver mirror and the beam size in the focus is evaluated to be around 200 μm (FWHM). The beam intensity in this case is 0.3 TW/cm^2 and it is intense enough to generate high order harmonics in ZnSe sample (see Fig.4.4).

ZnSe is a semiconductor with the bandgap of 2.7 eV. The material features high transparency – 0.55-20 μm, high nonlinear index $d_{14} = 20pm/V$, high damage threshold and good mechanical properties [146]. Even though the crystal does not feature high birefringence, random phase-matching could be obtained. It has been successfully applied to the second harmonic generation with CO_2 lasers [147] and was suggested as an alternative for single-crystal ZnSe in the autocorrelators [148].

We have also benefited from the random quasi-phasematched second harmonic generation in ZnSe. As ZnSe features high d_{eff}, it is very convenient to use it for the SHG in order to monitor the amplification in the last amplification stage. The available spectrometer to measure signals at 3 μm was Mozza (Fastlite), which is a scanning spectrometer, thus it takes time to record the spectrum, as well as the adjustment and optimization of the stage, which becomes more complicated in real time conditions. In order to make the optimization process easier, the second harmonic signal is generated and monitored with the Nirquest256 (Ocean Optics). The second harmonic is generated via random phase-matching. Micro-crystals are randomly oriented in the polycrystalline sample, thus the orientation of the crystal does not play a role for the SHG process. It is seen in Fig.4.1 that SHG spectrum generated in 5 mm ZnSe is narrower than in 400 μm AGS crystal. The efficiency of random quasi phase-matching is 2-3 orders of magnitude less efficient compared with the quasi phase-matching [149], here the spectrum of the detuned OPA2 is shown, which is broad, but also features relatively low energy (400 nJ), thus just the intense central part of the spectrum is efficiently converted into the SH signal. However, the ultra-broadband amplification bandwidth and insensitivity of the crystal angle makes the random-phase-matching very attractive for the tuning of central wavelength as there is no need to adjust the phase-matching angle of the doubling crystal.

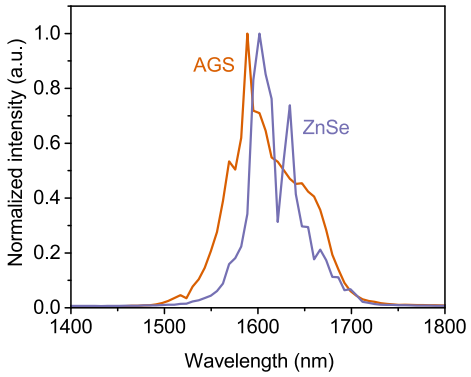

Figure 4.1 Second harmonic generation in 5 mm ZnSe and 400 µm of AGS.

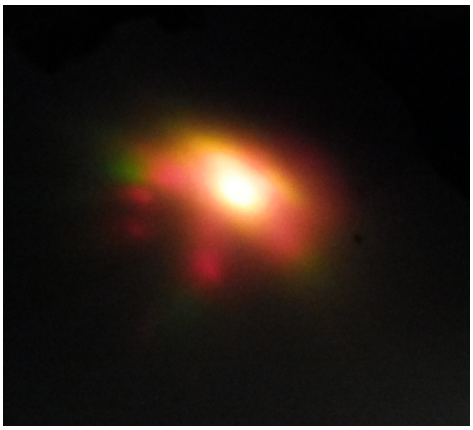

Figure 4.2 Dotted pattern is observed at the output of the ZnSe.

More recently, the diffraction patterns of second harmonic and sum frequency generation with femtosecond pulses were studied in [150]. There, a dotted pattern for generated wavelengths was observed. We here obtained similar results as shown (Fig.4.2).

The critical power for the filamentation in ZnSe is 40 MW and within the experimental conditions the peak power of the 3 µm pulses is 96 MW. When focusing the beam into 1 mm ZnSe polycrystalline sample, we observe HOH generation, spectral broadening and polychromatic dotted pattern. Compared to the input spectrum, the output is 2.5 times broader (see Fig.4.3). The high order harmonics are generated up to the 6^{th} harmonic and the spectrum has been recorded (see Fig.4.4).

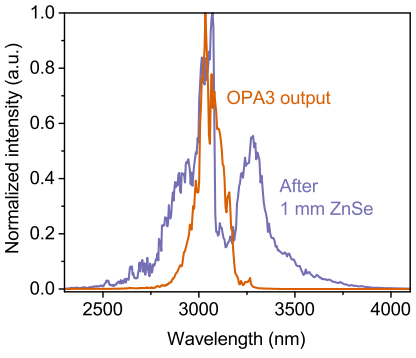

Figure 4.3 The output of OPA3 is broadened 2.5 times.

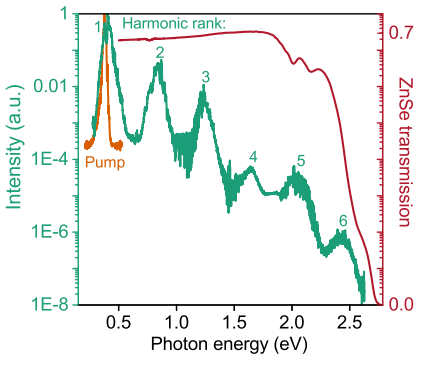

Figure 4.4 Spectral broadening and HOH generation in 1 mm ZnSe.

Similar experiments were done in [75, 151], and in both cases high order harmonics within the transmission range of the ZnSe crystal were generated. In[75] HOH were driven by 5.2 and 3.5 μm wavelengths, which are seed and idler beams from a Ho:YAG driven OPA. Up to 6^{th} (from 3.5 μm) and 9^{th} (from 5.2 μm) harmonics were observed. Up to 7^{th} harmonic was observed in [151] with the driving source at 3.9 μm. Those experiments were conducted with a lower repetition rate of 1 kHz, thus obtaining comparable results shows that the sample is not impacted by the thermal processes induced by the higher average power. So one could benefit from enhanced signal to noise ratio and if statistical data is needed, the acquisition speed is increased by 100 times.

4.2 HHG in gases, driven by SWIR parametric source

Introduction to HHG in gas

During the last few years or even over the last decade, intense, ultrashort laser pulses in the short-wavelength infrared region attracted a lot of attention in the scientific community. The expected increase of the energy cut off in high harmonic generation experiments have attracted many groups. The classical pump source used to generate HHG is Ti:Sapphire laser [152–155], but according to the three step model [1], the energy cut off of generated high harmonics scales as $I \times \lambda^2$. This favors longer driving wavelengths in order to generate more energetic XUV photons, and potentially shorter attosecond, soft X-ray pulses. It was successfully confirmed in [156, 157]. However, all the experiments were performed at rather low repetition rates, the OPAs were usually pumped by the Ti:Sapphire laser systems, which are limited to few kHz. Higher repetition rates could be reached with thin disk laser, innoslab or fiber laser technologies. Indeed, these three competing technologies were applied for HHG generation and show interesting results for building compact EUV sources. High harmonics with a photon flux of more than 5×10^7 photons/s on the 19th harmonic (23 eV) were generated by postcompressed thin disk oscillator [37]. HHG can be also generated in a intracavity of a thin disk oscillator providing 108 eV pulses at 78 MHz repetition rate [158] or 20 eV pulses at 17.4 MHz [159]. A thin disk based regenerative amplifier with an unprecedented average power was presented in [160], the system provides 540 W at repetition rates of 10-100 kHz, thus the pulse energy 5-50 mJ. After the upgrade of the pump, authors expect to increase laser power to more than 1 kW. As a promissing driving source for HHG Yb:YAG innoslab MOPA with a 620 W output at 20 MHz was presented in [161], furthermore, by cascading two amplifiers, average power is increased to 1.1 kW. Up to the 17th order HH driven by postcompressed pulses in a photonic crystal fiber were generated in

[162], HHG was driven by 20 W of 35 fs pulses. Femtosecond fiber lasers have also shown their capabilities for strong field experiments by demonstrating coherent XUV emission at unprecedented adjustable repetition rates reaching up to the MHz level [33]. Since then, femtosecond fiber laser performances have continuously increased to reach, for example, peak powers of 46 GW with an energy of 12 mJ [34] and durations reduced down to 2 cycles [35].

We intend to take advantage of the unique properties of high power pump systems to extend their capabilities to longer wavelengths, by pumping few cycle optical parametric amplifiers and generating intense fields in the MWIR infrared. However, the efficiency of MWIR OPAs is rather low and the highest reported values are around 7% [71, 89] and in the case of high repetition rate sources, the pulse energy is about few tens of μJ [89, 120, 119, 122, 46]. Another drawback for efficient HHG generation driven by MWIR lasers is the process efficiency scaling as $\lambda^{-5.5}$, which makes the HHG driven by high repetition rate MWIR drivers a challenging task. However, high energy, lower repetition rate systems are successfully driving HHG experiments [51, 50].

According to the three step model [1] the cut off law reads:

$$\begin{aligned} E_{cutoff} &= I_p + 3.17U_p \\ U_p &= 9.33 \times I\lambda^2 \end{aligned} \tag{4.1}$$

Where U_p is the ponderomotive energy (eV), I_p – the ionization potential (IP) (eV), I – the laser intensity ($10^{-14} \times W/cm^2$) and λ the driving laser's wavelength in μm. In order to extend the cut off energies either the intensity of the driving laser beam on the target, or the wavelength, or both could be increased. Howewer, laser intensity is limited by ionization saturation, thus the most promising way to generate high energy photons would be to increase the wavelength of the driving source. This was demonstrated experimentally in [51]. Here, while shifting the driving wavelength from 0.8 μm to 2 μm the energy is increased from 50 eV to 175 eV. This shows the high importance of ultrashort intense laser sources in the MWIR region.

The energy cut off with the Ti:Sa lasers was also extended by using ultrashort pulses – 5-7 fs, but this pulse duration is already approaching the few-optical cycle regime (optical cycle at 800 nm is 2.7 fs) and there is not a lot of space for improvement [163]. Thus, in [163] authors present results of HHG cut off extension when a longer driving wavelength is

used. In fact, they demonstrate a tunable driving source (1.1 μm – 1.5 μm), which also allows the tuning of the harmonic peaks. As the harmonic peak depends on the central wavelength of the driving source: $\hbar\omega_q = q\hbar\omega$ and $\lambda_q = \frac{\lambda_{IR}}{q}$, this feature could be used to match the resonance wavelength of materials studied in surface science and material spectroscopy. This was earlier proposed in [164] at 800 nm driving wavelengths. Tunable OPAs are therefore a very attractive tool for experiments requiring tunable XUV radiation.

Another cut off extension experiment is presented in [165], where the extension is again achieved by driving with longer wavelengths. HHG in Argon is driven by 0.8 μm, 1.3 μm, 2 μm and 3.6 μm laser sources, and cut off energies of 50 eV, 130 eV, 300 eV and 1 keV are estimated from the cut off law. The source was not yet suitable for HHG driven by 3.6 μm, but 2 μm yields slightly better results as shown in [51], where the cut off at 2 μm was 220 eV.

Even though many groups suggest the use of longer wavelengths as the most promising way to reach high-energy photons, the carbon K edge was reached by driving harmonics with Ti:Sapphire source [49]. Here, a quasi-phase-matching method was used and the phase matching took place in a periodically modulated hollow core fiber. Furthermore, the enhancement is achieved when the ionization level of atoms reaches 70-90%, which is far beyond the previously reported ionization level at which the cut off limit was enhanced by phase-matching.

A single attosecond pulse generation requires few (approaching single cycle) optical cycle driving pulses, which are difficult to achieve and usually require additional spectral broadening and post-compression, for example in hollow core fibers [166, 167]. Otherwise, an attosecond pulse train is generated and other techniques such as amplitude or polarization gating [168] have to be used to select one pulse of the train. This is definitely valid for shorter – near infrared driving wavelengths, but when reaching further into the mid-wavelength infrared, the phase-matching window reduces and even multi-cycle pulses generate single attosecond pulse [157]. For shorter wavelengths the phase matching window could be reduced by adjusting pressure and laser intensity on the target so that the pulse train contains fewer pulses, but for longer wavelengths it reduces to one pulse. These results are very promising and thus simplify and open new possibilities for classical MWIR OPA sources, which usually contain 5-10 optical cycles [88, 122, 169, 89, 120, 119] as an attractive and rather simple source for high-energy short attosecond pulses.

Two HHG experiments were conducted during the experimental campaigns in TU Wien. Firstly, HHG was driven by a parametric source in SWIR. Energy from the driving pulses was up to only a few mJ. Then, an efficient HHG source at 150 eV was driven by post-compressed $Yb:CaF_2$ laser pulses with the pulse energy of 10 mJ. Thus, two different drivers were implemented with two different experimental goals. Initially, short wave and MWIR driven HHG aimed at setting the minimal requirements for the driver at 3 µm, which was not set, as even sub-mJ pulses were not sufficient to detect the HH signal at 3 µm. The 1 µm driven HHG aimed at constructing an efficient and robust UV source at 150 eV to use for ultrafast demagnetization experiments.

Experimental set up

High harmonic generation was driven by the previously described KTA-OPA (see page 82) set up with three different wavelengths: 1.5 µm, 1.8 µm and 2.4 µm. The initially targeted 3µm was also tested, but no HHG signal could be recorded, probably due to insufficient intensity on the target. The four different wavelengths were obtained by tuning the phase-matching conditions of all OPA stages and the experiment was performed with either signal or the idler pairs: 1.5 µm and 3 µm; 1.8 µm and 2.4 µm.

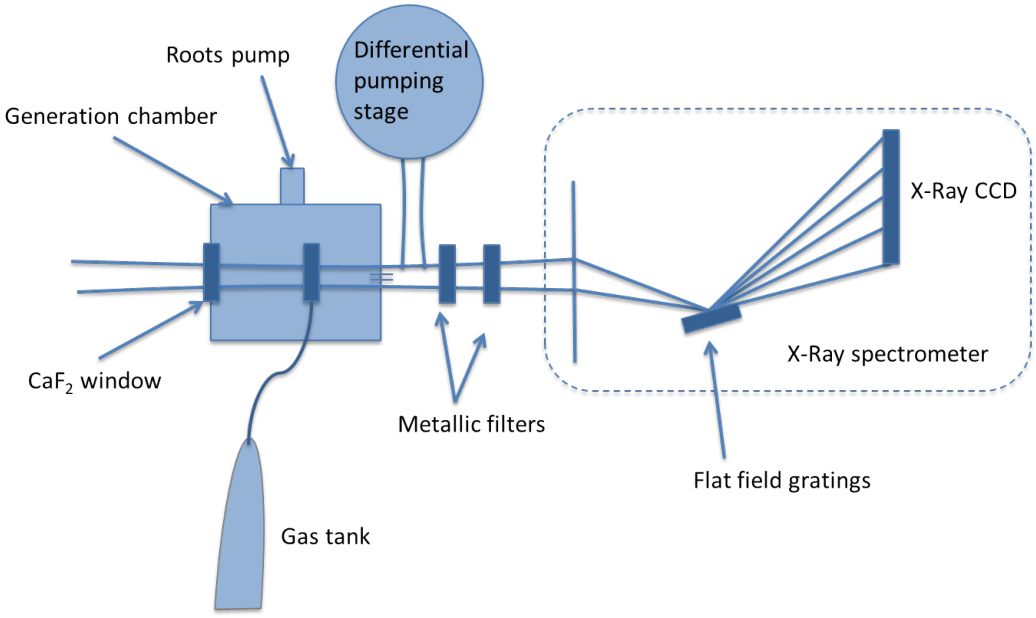

Figure 4.5 The experimental set up of OPA driven HHG.

The experimental set up is depicted in Fig.4.5. The focusing pump beam is sent to the generation chamber through a 4 mm CaF_2 window. 1.8 μm beam is focused with a 200 mm lens and 2.4 μm is focused with 120 mm lens. The beam is focused into the cell target, which was made by drilling a hole with the laser beam into a 2 mm nickel tube. After the differential pumping stage, the fundamental wavelength is absorbed by a set of metallic filters, for different possible combinations see Table.4.1. The summary of the filter's transmission is provided later in Fig.4.12. Then the selected harmonic beam is sent into the X-Ray spectrometer. The spectrometers entrance slit size is 50 μm. The spectrometer is designed in a way that the grating is fixed and the CCD camera is manually moved in order to record the diffracted signal. Firstly, the signal amplitude is optimized at zero order CCD position, and when the best high harmonic generation conditions are obtained, the CCD is shifted to the position where the first order of generated signal is expected (51-156 eV). The grating used was Hitachi High-Technologies 30-240 eV (g=1200/mm).

Table 4.1 Filter sets in wheel No.1 and wheel No.2.

Filter wheel No.	Filter No.	Filter thickness	Filter material
1	F1	500 nm	Aluminum
	F2	200 nm	Zirconium
	F3	300 nm	Titanium
2	F1	150 nm	Zirconium
	F2	100 nm	Titanium
	F3		Glass

Experimental results: HHG driven by 1.8 μm and 2.4 μm pulses

The initial goal of the experiment was to generate the high harmonics driven by 3 μm laser pulses, and measure the minimum requirements for the laser to generate the detectable harmonics signal. The generation of high order harmonics driven by longer wavelengths is challenging because the single atom response scales as $\lambda^{-5.5}$, thus generating high harmonics potentially reaching the keVs. We started with a configuration allowing the generation of lower energy harmonics that are easier to detect (higher grating efficiency). Here we used lower IP gas and shorter driving wavelengths. Current configuration of the X-Ray spectrometer limits us to the harmonic spectrum spreading up to 240 eV. The available media with low ionization potential in the laboratory were argon and acetylene. The energy cut off and required intensity of the driving laser beams in a few commonly used gases (argon, helium and neon) were calculated in [48]. By driving HHG in helium with 3 μm source we

could expect to reach keV energies, the required intensity on the target in this case is 3.7 $\times 10^{14}\,\mathrm{W/cm^2}$. Unfortunately, our OPA was not powerful enough to reach such intensities. Also, argon is a good candidate for our experiment as the expected energy cut off is very close to the edge of the used diffraction grating. Furthermore, the required beam intensity to reach full phase-matching conditions is about 3 times smaller than for helium.

Theoretically, the 3 μm beam should be focused to an intensity of 1.15 $\times 10^{14}\,\mathrm{W/cm^2}$ [48]. Indeed, in the experiment, the intensity of the focused 3 μm beam was estimated to be 1.5 $\times 10^{14}\,\mathrm{W/cm^2}$, which should be sufficient to generate harmonics in argon. We have observed nonlinear processes up to the 5^{th} order as well as filamentation. Unfortunately no HHG signal was recorded. One of the reasons why no signal was recorded could be that the laser intensity on target was over-estimated. Here we assume that the beam and pulse profiles are Gaussian, a biased assumption, as it has already been seen that the temporal pump pulse profile shape has wings. Pulse and beam distortions would decrease the focusability, and thus the maximum intensity on the target. Also, the limits of the driving laser were reached and no upgrade was feasible in the short period of time. Furthermore, due to the vacuum chamber size, it was not possible to use tighter focusing conditions to increase the laser intensity on the target. The direction of the experiment was moved to the high harmonics generation driven by shorter wavelengths: 1.8 μm and 2.4 μm. After successfully generating high harmonics with 1.8 μm and 2.4 μm source we were able to confirm the hypothesis of over-estimated laser intensity at the target. We can retrieve the experimental intensity value from the experimentally measured energy cut off as given in the Table 4.4.

Table 4.2 Intensity required to reach critical ionization levels for full HHG phase-matching at different wavelengths in Ar, He and Ne gases [48].

Wavelength, μm	Intensity $10^{14}\,\mathrm{W/cm^2}$ Argon	Intensity $10^{14}\,\mathrm{W/cm^2}$ Neon	Intensity $10^{14}\,\mathrm{W/cm^2}$ Helium	Intensity $10^{14}\,\mathrm{W/cm^2}$ Acetylene
0.8	2	4.6	6.4	1.5
1.03	1.8	4	5.8	-
1.5	1.5	3.5	4.9	-
1.8	1.4	3.3	4.55	-
2.4	1.25	2.9	4	-
3	1.15	2.6	3.7	-

1.8 μm and 2.4 μm wavelengths for further experiments were chosen because 2.4 μm is the closest wavelength to 3 μm, which is not affected by water absorption in the atmosphere (see Fig.4.6). Then even though the required intensity for HHG is higher (Table.4.2), the

efficiency of the process is also increased by a factor of 3.5. Furthermore, the energy of the available amplified signal increases about two times from 0.26 mJ at 3 μm to 0.51 mJ at 2.4 μm.

Table 4.3 The expected energy cut offs at full HHG phase-matching conditions as a function of driving wavelengths in Ar, He and Ne gases. [48]

Wavelength, μm	E_{CutOff}, eV Argon	E_{CutOff}, eV Neon	E_{CutOff}, eV Helium
1.03	77	165	230
1.5	125	280	370
1.8	160	360	480
2.4	240	540	750
3	330	785	1000

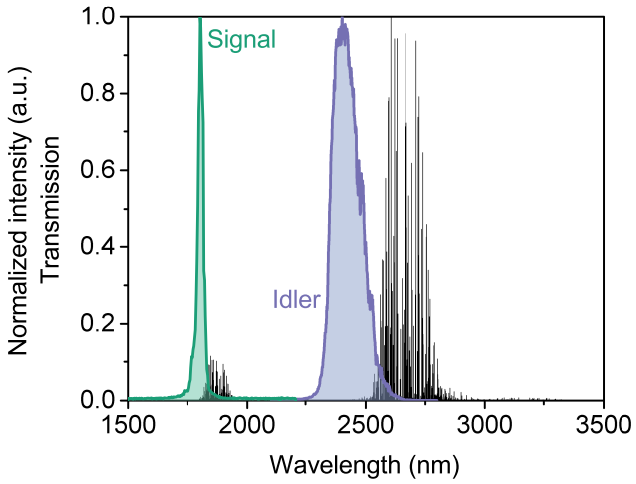

Figure 4.6 Water absorption in the atmosphere and signal and idler spectra.

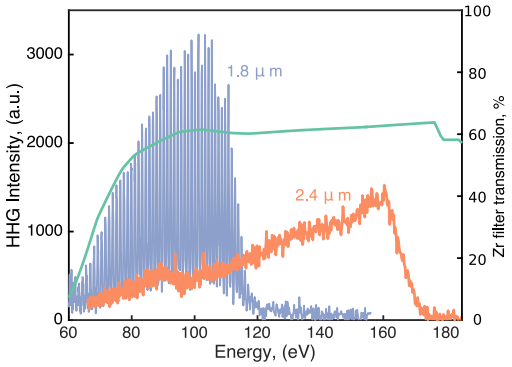

Figure 4.7 Spectra of HHG in Ar driven by 1.8 µm and 2.4 µm .

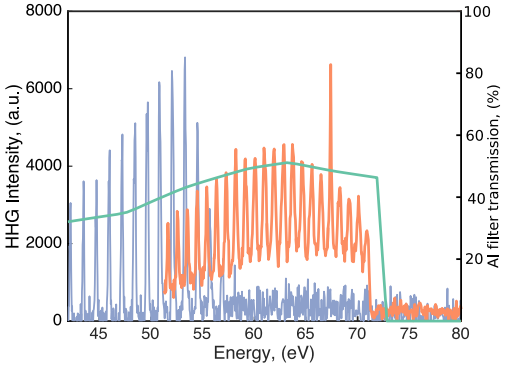

Figure 4.8 Spectra of HHG in C_2H_2 driven by 1.8 µm and 2.4 µm.

The spectra of HHG in Ar is shown in Fig.4.7. The collimated 1.8 µm beam is sent through a 4 mm aperture iris inserted before the 200 mm focusing lens in order to control the beam size, and consequently the intensity on the target. The beam intensity on the target is estimated at $2.6\times10^{14}\,\mathrm{W/cm^2}$, which is almost two times higher than necessary to reach harmonic generation in argon. The cut off for 1.8 µm is 110 eV, which is smaller compared to the expected energies of 160 eV. The 2.4 µm beam is focused with a 120 mm lens and the intensity on the target was estimated to $1.6\times10^{15}\,\mathrm{W/cm^2}$, which is more than 10 times higher than required. After measuring the high harmonics spectra (thus knowing the experimental energy cut off), we could calculate the actual intensity on the target. Theoretically estimated and calculated from the experimental cut off beam intensities in the target are summarized in Table. 4.4.

Table 4.4 Summary of beam intensities at the target.

1.8 µm			
Gas	**Theoretically estimated intensity,** W/cm^2	**Intensity extracted from the cut off,** W/cm^2	Ratio
Argon	2.6×10^{14}	9.8×10^{13}	2.6
Acetylene	1×10^{15}	4.3×10^{13}	23
2.4 µm			
Gas	**Theoretically estimated intensity,** W/cm^2	**Intensity extracted from the cut off,** W/cm^2	Ratio
Argon	1.6×10^{15}	8.4×10^{13}	19
Acetylene	1.3×10^{15}	3.4×10^{13}	38

We see that the intensity is over-estimated, mainly due to the fact that we do not take into account potential temporal pulse and beam profile distortions. The ratio between the estimated and recalculated values varies from 2.6 to 38 times. Furthermore, the retrieved values are lower than the laser intensity needed to reach critical ionization level, thus achieving full phase-matching conditions. Indeed, the measured cut off for 2.4 μm is 160 eV, which is smaller compared to the theoretical energies of 240 eV. Another reason affecting the HHG signal energy cut off could be the medium length. The optimum absorption limited medium length needed to reach 90 % of the macroscopic harmonic signal for driving wavelengths around 2 μm is around 7-8 mm [48], while during our experiments, we used a 2 mm cell. Increasing the target cell size might increase the signal level and allow measuring cut off XUV photons.

Another media, in which the harmonics were generated was acetylene. As the ionization potential is lower than in argon, the XUV energy cut off is also lower and as it is shown in Fig.4.7) the achieved energy cut offs are 57 eV for 1.8 μm and 71 eV for 2.4 μm at intensities of $1\times10^{15}\,\mathrm{W/cm^2}$ for 1.8 μm and $1.3\times10^{15}\,\mathrm{W/cm^2}$ for 2.4 μm. The saturation intensity for 800 nm driver is $1.5\times10^{14}\,\mathrm{W/cm^2}$ [170], unfortunately no data of saturation intensity dependent on the wavelength scaling were found in literature.

The power of driving pulses was changed by changing the opening of the iris. It should be noted that changing the iris diameter changes not just the power, but also the focusing conditions on the target as the beam size on the focusing lens is changing. Thus the intensity on the target is changed by varying two parameters: pulse energy and beam size. However, it was the only available method, as the classical attenuator consisting of $\lambda/2$ plate and a polarizer is not yet available at these wavelengths or is available only with the cost of high losses.

Conclusions

We have generated high harmonics in argon and acetylene, while driving the HHG with a SWIR OPA. Driving wavelengths were 1.8 μm and 2.4 μm. The maximum energy cut off in argon was 110 eV and 160 eV for 1.8 μm and 2.4 μm respectively, and 52 eV and 70 eV for acetylene. From the energy cut off we were able to estimate the beam intensity at the focus, which is summarized in the Table. 4.4. We could not record any HHG spectrum, when driving with the 3 μm source, even though the estimated conditions should have been sufficient for the HHG. However, as it is seen from the Table. 4.4, the laser intensity at the target is over-estimated by a factor between 2.6 and 38 times. This leads to the conclusion that

laser intensity of the 3 μm driver was not sufficient for high harmonic generation experiment.

4.3 HHG of postcompressed of the Yb:CaF_2 laser pulses in a hollow core fiber

Introduction to HHG driven post-compressed NIR laser pulses

High power systems have an advantage for pump-probe or other experiments, which need scanning or acquiring statistical data. Increasing the repetition rate from conventional 1 kHz of Ti:Sapphire driven HHG to 100 kHz decreases the acquisition time by 100 times, which might be crucial to conduct reliable experiments as it also reduces the high demands for long term stability and other environmental factors such as metro system running under the laboratory building. However, if one is considering using the high power laser pumped OPAs to drive the high harmonic generation, the state of the art sources are not yet there to deliver harmonics signal in the extreme ultraviolet (EUV) or X-Rays spectral region. Extreme Light Infrastructure (ELI) facilities are acquiring a state of the art source with the central wavelength at 3.1 μm, pulse energy of 150 μJ (15W at 100 kHz) and pulse duration of less than 4 optical cycles [57]. The maximum XUV photon energy, achievable with this system is being determined at the time this manuscript is being written.

Successful HHG experiments driven by high energy OPAs show higher cut off energies, even though they rarely report the efficiency of HHG or the photon flux in the harmonic beam. These sources also show the possibility of reaching kEvs [51] or the ability to tune the harmonic signal by tuning the OPA central wavelength, while aiming at a certain resonance or absorption line [40, 163] which is an advantage over laser-driven HHG.

On the other hand, efficient HHG sources at lower energies are delivering harmonic signals up to 800 μW [40]. Indeed, already commercially available HHG sources [53, 54] are based on post-compression in hollow core fibers: Ti:Sa lasers by KMLabs and Yb:FCPA by Active fiber. KMLabs provides harmonic beams up to 185 eV at repetition rate of 3 kHz and 40 eV at 50 kHz. Photon flux for those sources are $> 10^8$ ph/sec and $> 10^{12}$ ph/sec 1% BW respectively. Active fiber systems provide lower energy, but higher flux systems at the repetition rate tunable up to 10 MHz. Photon flux of $> 10^{14}$ ph/sec at 21 eV and $> 10^{11}$ ph/sec at 68 eV are available. Thus, being commercialized, these sources are proved to be stable, reliable and compact, which ensures that they are user-friendly and applicable for

experiments. Furthermore, the FCPA technology acquired by Active Fiber Systems for Yb doped fiber lasers was successfully transferred to Tm:FCPA and one might expect Tm:FCPA driven efficient HHG sources at higher harmonic energies.

In this section of the chapter, an efficient XUV source at 155 eV based on post-compressed Yb:CaF_2 driver will be presented. Compared to the SWIR OPA, this set up is more efficient and robust. The overall OPA efficiency does not exceed 20 %, thus limiting the pump-to-HHG efficiency. Furthermore, in the post-compression set up, the only sensitive point is the injection into the hollow core fiber. In the 3 stage OPA set up a precise temporal and spatial overlap should be assured in all 3 nonlinear crystals. The aim of this experiment is to provide an everyday operating source for ultrafast demagnetization experiment. Signal at 155 eV is required for the terbium sample. Since 155 eV are reachable by post-compressed 1 µm drivers, they have more advantages over the SWIR drivers.

Experimental set up

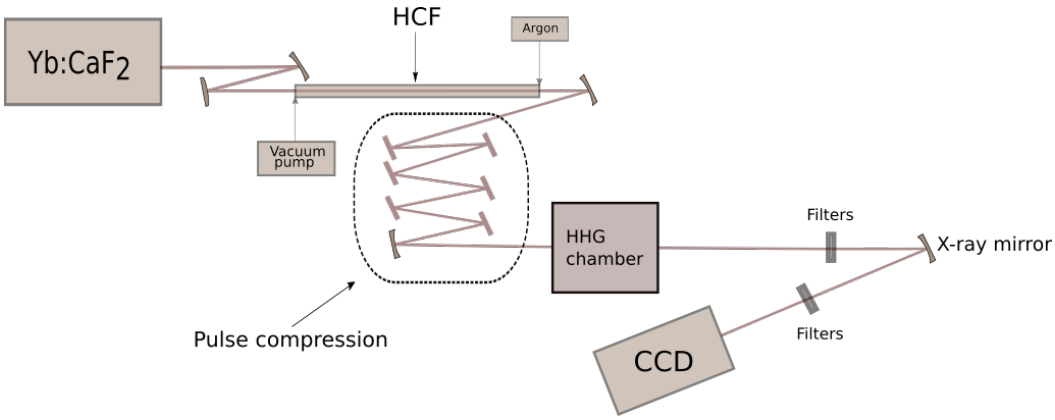

Figure 4.9 Experimental set up of HHG driven by post-compressed Yb:CaF_2.

Here, the output of the Yb:CaF_2 laser is post-compressed in a hollow core fiber (Few cycle inc.) filled with 550 mBar of argon. The experimental set up (see Fig.4.9) is almost identical to the ones described in [171] and [94]. The core diameter of the fiber was 750 µm and the length is 3 m. A picture of the fiber installation is shown in Fig. 4.10. The fiber is perfectly stretched along the beam propagating axis and its ends are glued into the end caps. Depending on the input power either metallic (low average power) or ceramic (high average power) end caps are used. Then these end caps are clamped to the holders, the clamping is done with three screws, which assures the possibility of optimizing fiber's alignment along the optical axis, and the tension along the fiber is also adjusted. Also, the fiber is under vacuum with a pressure gradient. Gas pressure is applied at the exit side and vacuum is constantly pumped at the entrance, in this way we have the lowest amount of gas at the input side, where the beam intensity is the highest. Such a gradient allows us to reduce ionization and self-focusing.

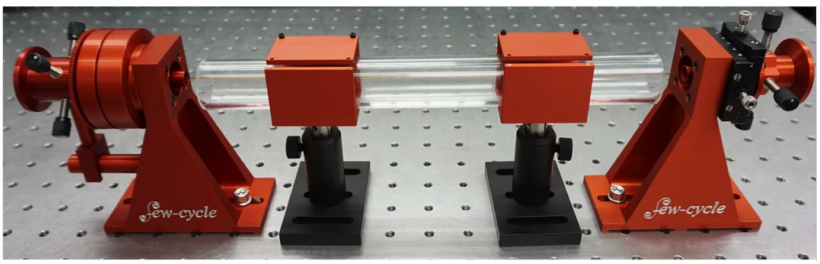

Figure 4.10 Experimental set up of the hollow core fiber for the pulse post-compression. (Picture from few-cycle.com.)

The transmission of the fiber is about 80% and up to 11 mJ of pulse energy was measured at the output. Afterwards the beam is collimated and compressed with a set of chirped mirrors (Ultrafast innovations) with the dispersion of 150 fs^2. Here, 6 bounces on the mirrors were used and the pulses were compressed down to 20 fs. The input and output spectra and temporal pulse profiles of the post-compression set up are shown in Fig. 4.11.

Then the post-compressed pulses are sent to the high harmonic generation chamber. The beam is focused with a -2000 mm ROC mirror and the beam diameter at the target is 185 µm. The cell targets of two sizes were used: 6 mm and 12 mm. After the HHG is generated, the fundamental beam is blocked with a set of filters (Table.4.1) and the HHG beam is re-imaged on the CCD camera. For the HHG imaging, a multilayer X-ray mirror (Ultrafast innovations) with the ROC of -3000 mm was used. The mirror also works as a selective filter, as it reflects a bandwidth of 5 eV at 155 eV, with 6 % efficiency. This specific wavelength was selected with the consideration of further ultrafast demagnetization experiments in a terbium sample. As the goal of the experiment here is to generate the highest flux at the selected wavelength range and use the full UV beam for the pump-probe experiment afterwards, the UV signal was directly measured with the CCD, excluding the previously used spectrometer-configuration. In this way, having the image of the full beam profile, we can estimate the flux and efficiency of the HHG.

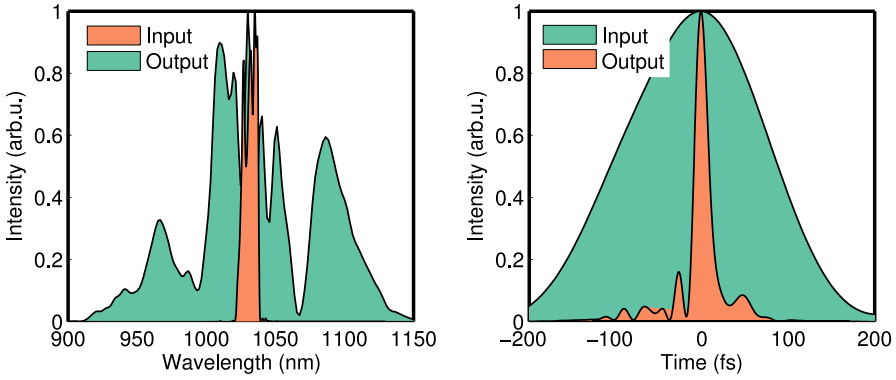

Figure 4.11 Spectral and temporal pulse profile of input and post-compressed CaF_2 laser pulses.

The transmission of the available filters is shown in Fig.4.12. Clearly, the aluminum filter is not suitable to use for harmonics generated at 155 eV, nevertheless it is useful for the alignment and initial optimization of the system, when the harmonics are generated in argon. So there are three filters left which transmit photons with the energy of 155 eV; the

highest transmission of 38 % is for a zirconium filter. It is 1.8 times higher than in silver and 6.3 times higher than in titanium, where the transmissions are 21% and 6% respectively [172]. The zirconium filter also has the highest absorption coefficient at 1030 nm ($1.6 \cdot 10^6$ cm^{-1})[173], which allows us to use thinner material to block the fundamental light and at the same time to increase the transmission of high harmonics at 155 eV. Even though the two zirconium filters would have been more efficient, the endurance and quality of the Ti filter was higher, and used as a first IR filter. The combination of 300 nm titanium and 200 nm zirconium filters were finally used for the following experiment.

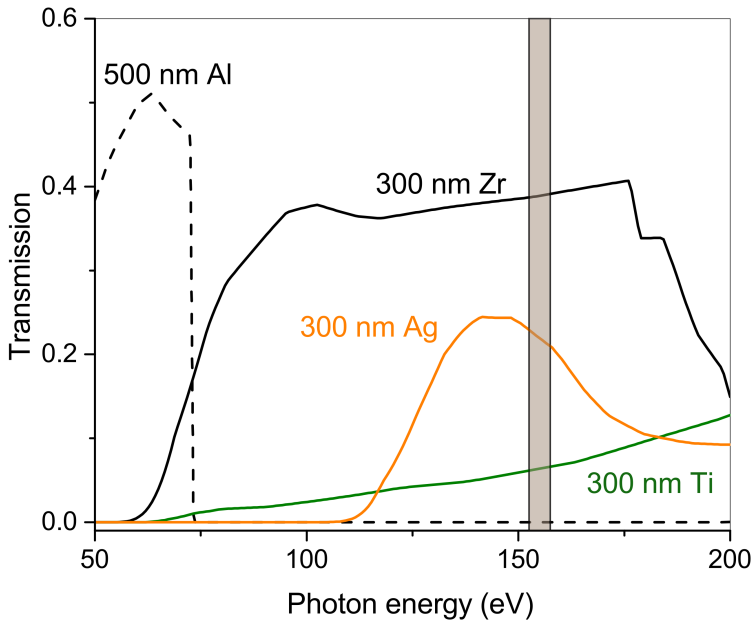

Figure 4.12 Transmission of the XUV filters.

HHG

The high order harmonics were generated in helium and neon, as well as in argon. The spectra of harmonics in all the three gases are shown in Fig.4.13 and 4.14. Due to the high transmission of aluminum filters at lower photon energies, it is convenient to use the signal to pre-align the system: check the transmission through the filter wheels, the harmonics position on the camera, etc. However it cannot be used for the ultrafast demagnetization experiment at 155 eV.

The signal level measured with the spectrometer at 155 eV is about 5 times higher in He

than in Ne. The same factor is obtained, when the full harmonics profile is measured with the CCD camera and the signal is integrated for the camera photon counts at the $1/e^2$ signal level. This was done in a 6 mm cell target. The expected cut off for HHG in Ne driven by a 1.03 µm laser pulses with 8 optical cycles (27 fs) is 165 eV, furthermore, the cut off could be increased due to decreased ionization levels for shorter laser pulses by approximately 15 % if the pulse duration is shortened to 3 cycles (10 fs) [48]. As the pulse duration of our driving pulses is about 27 fs, we would expect to have a cut off near the 165 eV region. However, the full phase-matching was not exploited and the measured harmonics spectrum only reached 142 eV.

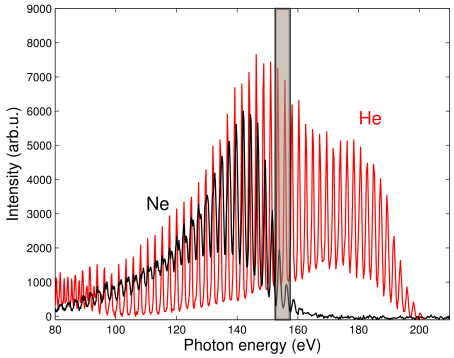

Figure 4.13 HHG in He and Ne.

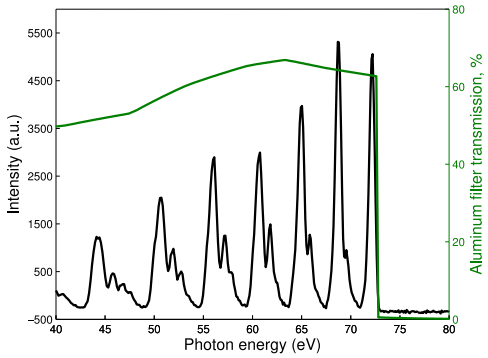

Figure 4.14 HHG in Ar.

As helium was identified as a better media for generating the harmonics signal at 155 eV, the following signal optimization was done using this gas. The 6 mm cell was changed for a 12 mm cell target. With the same laser parameters as the 6 mm target cell, the HHG signal improved by about 3 times, from 815 photons/s to 2325 photons/s. The HHG signal in Ne dropped by 4.5 times. The reduced HHG signal is because the absorption limited medium length for Ne is about 1 mm, while it is around 11 mm in He [48]. This also explains the improved HHG conditions in He, as the cell size is close to optimal for fulfilling the full macroscopic phase-matching conditions.

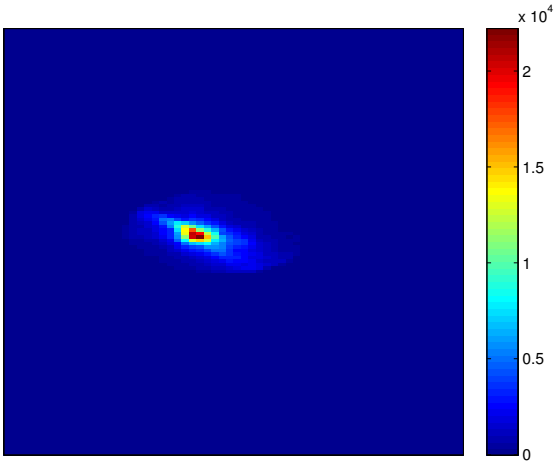

Figure 4.15 Beam profile of high harmonics generated in 12 mm cell target in Helium, integrated signal: 21860 photons/s.

The highest measured CCD count rate was 9.4 $\cdot 10^5$ counts/s (see Fig.4.3), which corresponds to 21860 photons/s. According to the device's data sheet, one photon induces 43 counts. The efficiency of the camera at 155 eV is 20 %. Thus the pulse energy of the XUV pulse at the target could be estimated at 3 pJ and the average power is 1.5 nW with the efficiency of the system at $3 \cdot 10^{-10}$.

Conclusions and system placing within the state of the art sources

A series of experiments on HHG driven by 1 μm lasers were developed by groups in Jena and Bordeaux, where the high harmonics were efficiently generated at longer wavelengths: around 20 eV [40, 52], 30 eV[174, 175, 33], 45 eV [176] and 60 eV [177]. The summary of a few selected systems is provided in table 4.5. All the systems except[177], where HHG is driven by OPA, are based on FCPA drivers. In [175, 40, 178] HHG are generated with the post-compressed pulses in a hollow core fiber. Starting from 300 fs the pulse duration is reduced to below 100 fs increasing the intensity, and accordingly limiting the impact of ionization on phase-matching [175]. In [33, 40, 176] SHG beams are used to drive the HHG. The efficiency of harmonic generation could reach 10^{-5}, 10^{-7}, however, after filtering the fundamental beam, there is also a significant amount of losses for the harmonics signal [52]. Attosecond physics demands a broadband spectrum isolated attosecond pulse (IAP) generation, while for imaging applications, resolution is limited by the spectral bandwidth, thus a narrowband source is preferable [178].

Table 4.5 Summary of 1 μm driven HHG

Ref.	Laser source	Pump Pulse Energy	Pulse duration	Media	Generated harmonics	Power/ Flux	Efficiency
[175]	C-FCPA	130-150 μJ	30 fs	Xenon	30 eV	143 μW	1.8×10^{-6}
[177]	OPA	14 μJ	6.6 fs	Argon	IAS 62-72 eV	5.8×10^{9} ph/s (62 nW)	4×10^{-8}
[40]	SHG C-FCPA	0.55 mJ	85 fs	Krypton	21.7 eV	832 μW	7.5×10^{-5}
[178]	C-FCPA	0.55 mJ	33 fs	Argon	68.6 eV		
[33]	SHG FCPA	28 - 100 μJ	270 fs	Krypton Argon Xenon	18-37 eV		
[176]	SHG FCPA	10 μJ	130 fs	Argon	46 eV		10^{-7}
[41]	$\boldsymbol{C-Yb:CaF_2}$	**10 mJ**	**20 fs**	**Helium**	**155 eV**	**1.5 nW**	$\mathbf{3\times10^{-10}}$

As one could see from Table 4.5, the last system stands out with the pulse energy much higher (150 eV) compared to the others (20 - 70 eV), while the overall systems efficiency is at the same order of magnitude of 10^{-5}. This source is ready to be used for ultrafast demagnetization experiments.

Challenges with the increased repetition rate

After the performance of the system has been well optimized, the only relatively easy way to increase the high harmonics flux is to increase the repetition rate of the pump laser. The Yb:CaF_2 amplifier is able to reach repetition rates up to 2 kHz. After increasing the repetition rate up to 2 kHz, the power of the laser output was 28 W and after passing through the hollow core fiber, 20 W could have been used to generate the high harmonic signal.

However, the whole experimental set up should be compatible with the increased thermal load. We have identified two weak points of our system: the hollow core fiber and the XUV filters. The endcaps which were at the time installed on the fiber were not suitable for high power operation, limiting their system's reliability. The XUV filters already allowed some leakage of the fundamental light, thus the probability of damaging the filters under long term use was already there and increasing the average power would significantly enhance the absorption of the fundamental beam.

In order to verify the damage threshold and durability several tests were performed. The CCD camera was removed and a CaF_2 window placed at the exit of the chamber in order

to avoid the damage of the CCD. Also, only the filters in the first filter wheel were tested in order to protect the XUV mirror. The light that passes through in the case of damage was monitored on the sensitive NIR detector card (Thorlabs VCR5). The output power of the laser was increased by 2 W steps and the filter was under the exposure for 2-3 min and passed to 5 min at high power levels. The damage threshold for the 300 nm zirconium filter was at 18 W of the laser output power and after an exposure of a few minutes, the filter was completely burned (Fig.4.16). The 500 nm aluminum, 300 nm titanium and 500 nm silver filters didn't exhibit any additional damages on the top of the older leakage holes already present in the filters before the high repetition rate tests. Unfortunately, the zirconium filters were the most suitable filters for the experiment, considering the compromise between the quality and the transmission of the generated harmonics.

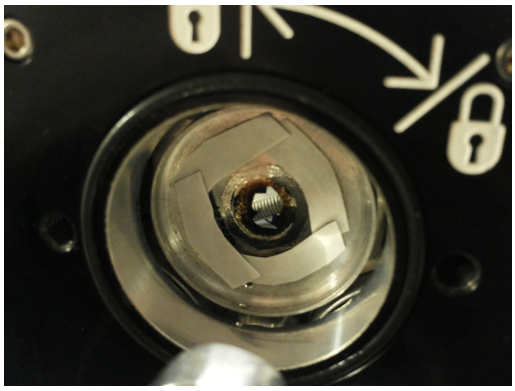

Figure 4.16 300 nm Zr filter damaged at 18 W of laser output power.

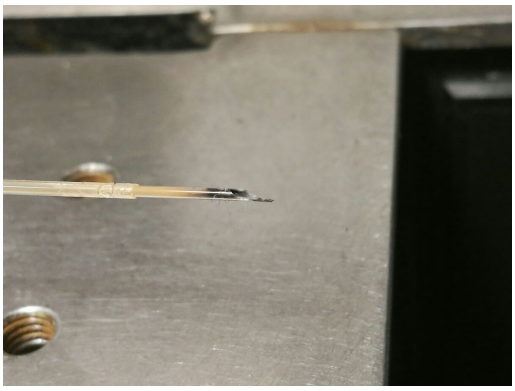

Figure 4.17 The input of the damaged fiber.

As the laser's beam pointing slowly drifts during the operation time, a constant adjustment of the beam coupling into the fiber is needed. After a day of the experiment, damage of the input side of the HCF was observed (Fig.4.17). Nevertheless, after changing a metallic endcap to a ceramic one, the issue was solved and the system worked as reliably as it did at lower repetition rate. Furthermore, a feedback loop correcting the beam pointing stabilization was installed on one of the injection to the HCF mirrors.

Even though the system seemed to be stable enough to operate at the high repetition rates, the issue with the damage of the zirconium filters prevented us from measuring the HHG flux in the current configuration, as the damage of the CCD camera would be costly and delay the other planned experiments on the system.

4.4 Conclusions

Three HHG experiments were described in this chapter. Firstly, the driving source was a 3 µm OPA working at a 100 kHz. As the pulse energy was relatively low (8 µJ), high harmonic generation was only achievable in solids. HHG up to the 6^{th} order was generated in 1 mm ZnSe.

Then experiments of HHG in gas were conducted. Firstly HHG was driven by SWIR OPA generating pulses at 1.8 µm and 2.4 µm. We have generated high harmonics in argon and acetylene, the summary of results is provided in Table. 4.6.

Table 4.6 Summary of SWIR OPA driven HHG.

	1.8 µm			2.4 µm		
Gas	**Pump Energy, mJ**	**Retrieved Intensity,** $W/cm^2 \cdot 10^{13}$	**Cut off, eV**	**Pump Energy, mJ**	**Retrieved Intensity,** $W/cm^2 \cdot 10^{13}$	**Cut off, eV**
Argon	0.8	9.8	110	0.6	8.4	160
Acetylene	0.7	4.3	53	0.7	3.4	70

Later, HHG was driven by post-compressed 1 µm pulses. The goal of the experiment was to efficiently generate XUV signal at 155 eV. We succeeded in generating harmonics with the average power of 1.5 nW and efficiency of $3 \cdot 10^{10}$.

Summary and conclusions

During the PhD, parametric processes for generating SWIR and MWIR ultrashort pulses in two different configurations – high repetition rate and high energy – were investigated. In both systems, the seed for the OPAs is obtained via supercontinuum generation. It is crucial to generate stable and sufficiently intense seed signals. Earlier, most of the conventional WLC based OPAs in the SWIR or MWIR were based on WLC generation in the visible. We simplified the scheme and directly amplified the WLC in SWIR. To achieve the optimal broadening into the red side, we tested different conditions. It turned out that a longer medium length and looser focusing conditions provided the broadest WLC spectrum, reaching up to 2.2 – 2.4 µm. Both systems were mainly based on KTA crystals, with the exception on the high power OPA DFG stage, where a chirped PPLN was used.

The high power Yb:FCPA pumped 3 µm OPA delivered 85 fs pulses with the energy of 8 µJ, the overall efficiency of the system from pump to 3 µm was about 3 %. High energy Yb:CaF_2 pumped 2.4 µm OPA delivered 123 fs pulses at 2.4 µm and 165 fs pulses at 1.8 µm, with the corresponding pulse energies of 1.3 mJ and 1.7 mJ, the overall efficiency of the system from pump to 2.4 µm was about 9 %. The higher efficiency of the high energy system at 2.4 µm could be due to the proximity of the degenerate conditions and minimal losses in the system.

Another goal of the thesis was to use these parametric sources for strong field experiments. The lower energy, but high average power OPA was used for the high harmonic and supercontinuum generation in solids. HHG was generated in ZnSe and WLC in YAG samples. Unfortunately, the pulse energy was too low to generate harmonics in gas. But this was achieved with the high energy system. Here, the experiment was split into two parts: HHG in gas driven by SWIR OPA and HHG driven by post-compressed Yb:CaF_2 laser pulses.

In the case of SWIR OPA driven HHG, the initial goal was to set the minimum requirements for HHG driven by 3 µm OPA. However, the beam intensity was too low to observe a

signal in these conditions. Thus, high harmonics were generated with shorter wavelengths. And even then power scaling was not possible due to very strict phase-matching conditions. Pulse energies were also lower than required to ensure sufficient intensity at the target in order to fully exploit the phase-matching.

The second part of the experiment was to provide a reliable source for ultrafast demagnetization experiments. The sample for the experiments was terbium, requiring XUV signal at 155 eV. These energies could have also been reached by the SWIR OPA driven HHG. However, the OPA efficiency of 9 % was limiting the intensity on the target. Thus, the post-compressed Yb:CaF_2 laser pulses were chosen to efficiently generate the harmonic beam in that spectral region.

We were able to change the repetition of the Yb:CaF_2 laser, so while keeping the same pulse energy we also increase the average power. We would expect to increase the generated harmonic signal with the same ratio as the increased repetition rate. However, here we faced challenges in adapting the system for the high average power regime. The XUV filters used in the experiment could not handle the increased heat load and started burning. Thus another, preferably equally efficient, way of blocking the HHG driving beam should be found.

About a decade ago, it was very common to refer to a new SWIR OPA as the perfect source to drive HHG experiments. However, choosing the perfect driver might be more complicated. Depending on the pulse energy of the driving source and the demands on the generated harmonics energy a different approach should be chosen for each particular case. Unless one needs to reach high energies in the EUV or X-Rays, the OPA based sources are not yet efficient enough, especially considering that the energy conversion from near-infrared pump laser to the middle-infrared OPA hardly exceed 20 %. However, they are very interesting sources for strong field physics experiments in solids. Furthermore, lower harmonics are efficiently generated by post-compressed near-infrared laser sources, so at the moment, they are a reliable go-to for a HHG source we use everyday.

Bibliography

[1] P. Corkum, "Plasma perspective on strong-field multiphoton ionization," *Physical Review Letters*, vol. 71, no. 13, pp. 1994–1997, 1993.

[2] A. D. Shiner, C. Trallero-Herrero, N. Kajumba, H.-C. Bandulet, D. Comtois, F. Légaré, M. Giguère, J.-C. Kieffer, P. B. Corkum, and D. M. Villeneuve, "Wavelength scaling of high harmonic generation efficiency," *Phys. Rev. Lett.*, vol. 103, no. 7, 2009.

[3] I. T. Sorokina, V. V. Dvoyrin, N. Tolstik, and E. Sorokin, "Mid-IR ultrashort pulsed fiber-based lasers," *IEEE Journal of Selected Topics in Quantum Electronics*, vol. 20, no. 5, 2014.

[4] S. B. Mirov, V. V. Fedorov, D. Martyshkin, I. S. Moskalev, M. Mirov, and S.Vasilyev, "Progress in Mid-IR lasers based on Cr and Fe-doped IIVI chalcogenides," *IEEE Journal of Selected Topics in Quantum Electronics*, vol. 21, no. 1, 2014.

[5] P. A. Franken, A. E. Hill, C. W. Peters, and G. Weinreich, "Generation of optical harmonics," *Phys. Rev. Lett.*, vol. 7, no. 4, pp. 118–120, 1961.

[6] B. E. Schmidt, N. Thiré, M. Boivin, A. Laramée, F. Poitras, G. Lebrun, T. Ozaki, H. Ibrahim, and F. Légaré, "Frequency domain optical parametric amplification," *Nature Communications*, vol. 5, 2014.

[7] H. Pires, M. Baudisch, D. Sanchez, M. Hemmer, and J.Biegert, "Ultrashort pulse generation in the mid-IR," *Progress in Quantum Electronics*, vol. 43, pp. 1–30, 2015.

[8] C. Manzoni and G. Cerullo, "Design criteria for ultrafast optical parametric amplifiers," *Journal of Optics*, vol. 18, no. 10, pp. 103501–103534, 2016.

[9] R. W. Boyd, *Nonlinear Optics*. Cambridge, Massachusetts, United States: Academic Press, 2008.

[10] "bblaser." http://www.bblaser.com/images/05.gif. Accessed on 2018-02-12.

[11] G. Cerullo and S. D. Silvestri, "Ultrafast optical parametric amplifiers," *Review of scientific instruments*, vol. 74, no. 1, pp. 1–18, 2003.

[12] A. Dubietis, G. Tamošauskas, R. Šuminas, V. Jukna, and A. Couairon, "Ultrafast supercontinuum generation in bulk condensed media," *Lith. J. Phys.*, vol. 57, no. 3, pp. 113–147, 2017.

[13] "bblaser." http://iramis.cea.fr/Images/astImg/1731_2.jpg. Accessed on 2018-03-27.

[14] F. Silva, D. Austin, A. Thai, M. Baudisch, M. Hemmer, D. Faccio, A. Couairon, and J. Biegert, "Multi-octave supercontinuum generation from mid-infrared filamentation in a bulk crystal," *Nature Communications*, vol. 3, 2012.

[15] C. Hazera, *NOPCPA Ultracourt Pompé par CPA Fibré Haute Cadence*. PhD thesis, University of Bordeaux, 2014.

[16] E. Boursier, P. Segonds, B. Boulanger, C. Félix, J. Debray, D. Jegouso, B. Ménaert, D. Roshchupkin, and I. Shoji, "Phase-matching directions refined Sellmeier equations, and second-order nonlinear coefficient of the infrared Langatate crystal $La_3Ga_{5.5}Ta_{0.5}4O_{14}$," *Optics Letters*, no. 13, pp. 4033–4036, 2014.

[17] "HITRAN online, http://hitran.org." Accessed on 2017-12-18.

[18] J. Byrnes, *Unexploded Ordnance Detection and Mitigation*. Springer, 2009.

[19] T. Maiman, "Stimulated optical radiation in ruby," *Nature*, vol. 187, pp. 493–494, 1960.

[20] S. Haroche, "Essay: Fifty years of atomic, molecular and optical physics in physical review letters," *Physical Review Letters*, vol. 101, no. 16, 2008.

[21] J. A. Giordmaine, "Mixing of light beams in crystals," *Phys. Rev. Lett.*, vol. 8, no. 1, pp. 19–20, 1962.

[22] P. D. Maker, R. W. Terhune, M. Nisenoff, and C. M. Savage, "Effects of dispersion and focusing on the production of optical harmonics," *Phys. Rev. Lett.*, vol. 8, no. 1, pp. 21–22, 1962.

[23] J. A. Giordmaine and R. C. Miller, "Tunable coherent parametric oscillation in $LiNbO_3$ at optical frequencies," *Phys. Rev. Lett.*, vol. 14, no. 24, p. 973, 1965.

[24] S. Akhmanov, A. Kovrigin, A. Piskarskas, V. Fadeev, and R. Khokhlov, "Observation of parametric amplification in the optical range," *JETP Letters*, vol. 2, no. 7, pp. 191–193, 1965.

[25] P. F. Moulton, "Spectroscopic and laser characteristics of $Ti:Al_2O_3$," *Journal of the Optical Society of America B*, vol. 3, no. 1, pp. 125–133, 1986.

[26] "Peter Moulton on the Ti:Sapphire laser." https://www.youtube.com/watch?v=D4Ej0k6z_fc. Accessed on 2017-01-16.

[27] A. Dubietis, G. Jonušauskas, and A. Piskarskas, "Powerful femtosecond pulse generation by chirped and stretched pulse parametric amplification in BBO crystal," *Optics Communications*, vol. 88, no. 4, pp. 437–440, 1992.

[28] C. P. Hauri, M. Bruck, W. Kornelis, J. Biegert, and U. Keller, "Generation of 14.8-fs pulses in a spatially dispersed amplifier," *Optics Letters*, vol. 29, no. 2, 2004.

[29] S. Ališauskas, R. Butkus, V. Pyragaitė, V. Smilgevičius, A. Stabinis, and A. Piskarskas, "Prospects for increasing average power of optical parametric chirped pulse amplifiers via multi-beam pumping," *Optics Communications*, vol. 283, no. 3, pp. 469–473, 2009.

[30] V. Pyragaitė, R. Butkus, G. Archipovaite, D. Kezys, A. Stabinis, A. Piskarskas, and V. Smilgevičius, "Minimization of parametric diffraction effect in two-beam pumped optical parametric amplification," *Optics Communications*, vol. 309, no. 3, pp. 344–348, 2013.

[31] G. M. Archipovaite, "Two beam pumped parametric amplifier of chirped pulses, Open Readings 2013. 55th Scientific Conference for Young Students of Physics and Natural Sciences," 2012.

[32] G. Mennerat, B. Trophéme, and B. Boulanger, "Experimental demonstration of five-beam-pumped optical parametric amplification," *Optics Letters*, vol. 38, no. 17, pp. 3319–3321, 2013.

[33] J. Boullet, Y. Zaouter, J. Limpert, S. Petit, Y. Mairesse, B. Fabre, J. Higuet, E. Mével, E. Constant, and E. Cormier, "High-order harmonic generation at a megahertz-level repetition rate directly driven by an ytterbium-doped-fiber chirped-pulse amplification system," *Optics Letters*, vol. 34, no. 9, pp. 1489–1491, 2009.

[34] M. Kienel, M. Müller, A. Klenke, J. Limpert, and A. Tünnermann, "12 mJ kW-class ultrafast fiber laser system using multidimensional coherent pulse addition," *Optics Letters*, vol. 41, no. 14, pp. 3343–3346, 2016.

[35] M. Müller, M. Kienel, A. Klenke, T. Gottschall, E. Shestaev, M. Plötner, J. Limpert, and A. Tünnermann, "1 kW 1 mJ eight-channel ultrafast fiber laser," *Optics Letters*, vol. 41, no. 15, pp. 3439–3442, 2016.

[36] C. J. Saraceno, F. Emaury, C. Schriber, M. Hoffmann, M. Golling, T. Südmeyer, and U. Keller, "Ultrafast thin-disk laser with 80 µJ pulse energy and 242 W of average power," *Optics Letters*, vol. 39, no. 1, pp. 9–12, 2014.

[37] F. Emaury, A. Diebold, C. J. Saraceno, and U. Keller, "Compact extreme ultraviolet source at megahertz pulse repetition rate with a low-noise ultrafast thin-disk laser oscillator," *Optica*, vol. 2, no. 11, pp. 980–984, 2015.

[38] "AmpLight." http://amplight.at/. Accessed on 2018-01-15.

[39] M.Nisoli, S. D. Silvestri, and O. Svelto, "Generation of high energy 10 fs pulses by a new pulse compression technique," *Applied Physics Letters*, vol. 68, no. 20, pp. 2793–2795, 1996.

[40] R. Klas, S. Demmler, M. Tschernajew, S. Hädrich, Y. Shamir, A. Tünnermann, J. Rothhardt, and J. Limpert, "Table-top milliwatt-class extreme ultraviolet high harmonic light source," *Optica*, vol. 3, no. 11, pp. 1167–1170, 2016.

[41] T. Balčiūnas, G. Fan, A.Pugžlys, T. Kanai, B. E. Schmidt, V. Cardin, F. Légaré, V. Pervak, and A. Baltuška, "Efficient 170 eV source directly driven by an Yb laser amplifier, CLEO/Europe-EQEC 2017," 2017.

[42] M. Gebhardt, C. Gaida, T. Heuermann, F. Stutzki, C. Jauregui, J. Antonio-Lopez, A. Schulzgen, R. Amezcua-Correa, J. Limpert, and A. Tünnermann, "Nonlinear pulse compression to 43W GW-class few-cycle pulses at 2 µm wavelength," *Optics Letters*, vol. 42, no. 20, pp. 4179–4182, 2017.

[43] D. Brida, M. Marangoni, C. Manzoni, S. D. Silvestri, and G. Cerullo, "Two-optical-cycle pulses in the mid-infrared from an optical parametric amplifier," *Optics Letters*, vol. 33, no. 24, pp. 2901–2903, 2008.

[44] R. M. Hochstrasser, "Two-dimensional spectroscopy at infrared and optical frequencies," *PNAS*, vol. 104, no. 36, pp. 14190–14196, 2007.

[45] K. Sekiguchi, S. Yamaguchi, and T. Taharaa, "Femtosecond time-resolved electronic sum-frequency generation spectroscopy: A new method to investigate ultrafast dynamics at liquid interfaces," *The Journal of Chemical Physics*, vol. 128, 2008.

[46] M. Hemmer, A. Thai, M. Baudisch, H. Ishizuki, T. Taira, and J. Biegert, "18 μJ energy, 160-kHz repetition rate, 250-MW peak power mid-IR OPCPA," *Chinese Optics Letters*, vol. 11, no. 1, 2013.

[47] B. W. Mayer, C. R. Phillips, L. Gallmann, M. M. Fejer, and U. Keller, "Sub-four-cycle laser pulses directly from a high-repetition-rate optical parametric chirped-pulse amplifier at 3.4 μm," *Optics Letters*, vol. 38, no. 21, pp. 4265–4268, 2013.

[48] T. Popmintchev, M. Chen, A. Bahabad, M. Gerrity, P. Sidorenko, O. Cohen, I. P. Christov, M. M. Murnane, and H. C. Kapteyn, "Phase matching of high harmonic generation in the soft and hard X-ray regions of the spectrum," *PNAS*, vol. 106, no. 26, pp. 10516–10521, 2009.

[49] E. Gibson, A. Paul, N. Wagner, R. Tobey, D. Gaudiosi, S. Backus, I. P. Christov, A. Aquila, E. M. Gullikson, D. T. Attwood, M. M. Murnane, and H. C. Kapteyn, "Coherent soft X-ray generation in the water window with quasi-phase matching," *Science*, vol. 302, pp. 95–98, 2003.

[50] T. Kanai, T. Balčiūnas, G. Fan, E. Kaksis, G. Andriukaitis, A. Pugžlys, and A. Baltuška, "Development of a high-power mid-IR parametric amplifier for multicolor driving of high harmonic generation, ASSL," 2015.

[51] T. Popmintchev, M. C. Chen, D. Popmintchev, P. Arpin, S. Brown, S. Ališauskas, G. Andriukaitis, T. Balčiunas, O. D. Mücke, A. Pugzlys, A. Baltuška, B. Shim, S. E. Schrauth, A. Gaeta, C. Hernández-Garca, L. Plaja, A. Becker, A. Jaron-Becker, M. M. Murnane, and H. C. Kapteyn, "Bright coherent ultrahigh harmonics in the keV X-ray regime from mid-infrared femtosecond lasers," *Science*, vol. 136, pp. 1287–1291, 2012.

[52] S. Hädrich, M. Krebs, J. Rothhardt, H. Carstens, S. Demmler, J. Limpert, and A. Tünnermann, "Generation of μW level plateau harmonics at high repetition rate," *Optics Express*, vol. 19, no. 20, pp. 19374–19383, 2011.

[53] "KMLabs." https://kmlabs.com/product/xuus/. Accessed on 2017-12-18.

[54] "Active Fiber Systems." http://www.afs-jena.de/. Accessed on 2017-12-18.

[55] S. Ghimire, A. DiChiara, E. Sistrunk, P. Agostini, L. F. DiMauro, and D. A. Reis, "Observation of high-order harmonic generation in a bulk crystal," *Nature Physics*, vol. 7, pp. 138–141, 2011.

[56] Y. S. You, Y. Yin, Y. Wu, A. Chew, X. Ren, F. Zhuang, S. Gholam-Mirzaei, M. Chini, Z. Chang, and S. Ghimire, "High-harmonic generation in amorphous solids," *Nature Communications*, vol. 8, 2017.

[57] "ELI-ALPS." http://www.eli-hu.hu/?q=en/02_Parameters. Accessed on 2017-12-18.

[58] R. L. Sutherland, *Handbook of Nonlinear Optics*. Boca Raton, Florida, United States: CRC Press, 2003.

[59] V. Dmitriev, G. Gurzadyan, and D. Nikogosyan, *Handbook of Nonlinear Optical Crystals*. Springer, 1991.

[60] D. N. Nikogosyan, *Nonlinear Optical Crystals: A Complete Survey*. Springer, 2005.

[61] "SNLO." http://www.as-photonics.com/snlo. Accessed on 2018-02-08.

[62] "TOPAS, http://lightcon.com/Products/opa-topas.html." Accessed on 2017-12-18.

[63] "Venteon OPCPA, https://www.laserquantum.com/products/detail.cfm?id=79." Accessed on 2017-12-18.

[64] Y. Shamir, J. Rothhardt, S. Hädrich, S. Demmler, M. Tschernajew, J. Limpert, and A. Tünnermann, "High-average-power 2 µm few-cycle optical parametric chirped pulse amplifier at 100 kHz repetition rate," *Optics Letters*, vol. 40, no. 23, pp. 5546–5549, 2015.

[65] J. Nillon, *Amplification Paramétrique Ultra-Large Bande Dans L'Infrarouge en Regime de Forte Énergie et de Forte Puissance Moyenne*. PhD thesis, University of Bordeaux, 2012.

[66] A. Lyachev, I. O. Musgrave, Y. Tang, C. Hernandez-Gomez, I. N. Ross, M. Galimberti, O. V. Chekhlov, and J. Collier, "Development of a novel large bandwidth front-end system for high peak power opcpa systems," *Optics Express*, vol. 29, no. 17, 2011.

[67] V. Pasiskevicius, G. Strömqvist, F. Laurell, and C. Canalias, "Quasi-phase matched nonlinear media: Progress towards nonlinear optical engineering," *Optical Materials*, vol. 34, no. 3, pp. 513–523, 2012.

[68] D. A. Bryan, R. Gerson, and H. E. Tomaschke, "Increased optical damage resistance in lithium niobate," *Appl. Phys. Lett.*, vol. 9, no. 44, pp. 847–849, 1984.

[69] Y. Deng, A. Schwarz, H. Fattahi, M. Ueffing, X. Gu, M. Ossiander, T. Metzger, V. Pervak, H. Ishizuki, T. Taira, T. Kobayashi, G. Marcus, F. Krausz, R. Kienberger, and N. Karpowicz, "Carrier-envelope-phase-stable, 1.2 mJ, 1.5 cycle laser pulses at 2.1 µm," *Optics Letters*, vol. 37, no. 23, pp. 4973–4975, 2012.

[70] W. Li, Y. Li, Y. Xu, J. Lu, P. Wang, J.Du, and Y. Leng, "Measurements of nonlinear refraction in the mid-infrared materials $ZnGeP_2$ and $AgGaS_2$," *Appl. Phys. B*, vol. 82, no. 123, 2017.

[71] G. M. Archipovaite, P. Malevich, E. Cormier, T. Lihao, A. Baltuška, and T. Balčiūnas, "Efficient few-cycle mid-IR pulse generation in the 5-11 µm window driven by an Yb amplifier, ASSL," 2017.

[72] F. Rotermund, V. Petrov, and F. Noack, "Difference-frequency generation of intense femtosecond pulses in the mid-IR (4-12 μm) using $HgGa_2S_4$ and $AgGaS_2$," *Optics Communications*, vol. 185, pp. 177–183, 2000.

[73] L. von Grafenstein, M. Bock, D. Ueberschaer, K. Zawilski, P. Schunemann, U. Griebner, and T. Elsaesser, "5 μm few-cycle pulses with multi-gigawatt peak power at a 1 kHz repetition rate," *Optics Letters*, vol. 42, no. 19, pp. 3796–3799, 2017.

[74] D. Sanchez, M. Hemmer, M. Baudisch, S. L. Cousin, K. Zawilski, P. Schunemann, O. Chalus, C. Simon-Boisson, and J. Biegert, "7 μm, ultrafast, sub-millijoule-level mid-infrared optical parametric chirped pulse amplifier pumped at 2 μm," *Optica*, vol. 3, no. 2, pp. 147–150, 2016.

[75] T. Kanai, P. Malevich, S. S. Kangaparambil, K. Ishida, M. Mizui, K. Yamanouchi, H. Hoogland, R. Holzwarth, A. Pugzlys, and A. Baltuska, "Parametric amplification of 100 fs mid-infrared pulses in $ZnGeP_2$ driven by a Ho:YAG chirped-pulse amplifier," *Optics Letters*, vol. 42, no. 4, pp. 683–686, 2017.

[76] H. J. Liu, G. F. Chen, W. Zhao, Y. S. Wang, T. Wang, and S. H. Zhao, "Phase matching analysis of noncollinear optical parametric process in nonlinear anisotropic crystals," *Optics Communications*, vol. 4-6, no. 10, pp. 507–514, 2001.

[77] "spdcalc." http://spdcalc.org/. Accessed on 2018-02-08.

[78] "NIST." https://www.nist.gov/services-resources/software/noncollinear-phase-matching-uniaxial-and-biaxial-crystals. Accessed on 2018-02-08.

[79] C. Heese, C. R. Phillips, L. Gallmann, M. M. Fejer, and U. Keller, "Ultrabroadband, highly flexible amplifier for ultrashort mid infrared laser pulses based on aperiodically poled $Mg : LiNbO_3$," *Optics Letters*, vol. 35, no. 14, pp. 2340–2342, 2010.

[80] C. R. Phillips, B. W. Mayer, L. Gallmann, and U. Keller, "Frequency-domain nonlinear optics in two-dimensionally patterned quasi-phase-matching media," *Optics Express*, vol. 24, no. 14, 2016.

[81] N. Garejev, G. Tamošauskas, and A. Dubietis, "Comparative study of multioctave supercontinuum generation in fused silica, YAG, and LiF in the range of anomalous group velocity dispersion," *Journal of the Optical Society of America B*, vol. 34, no. 1, pp. 88–94, 2016.

[82] A. Calendron, H. Çankaya, G. Cirmi, and F. X. Kärtner, "White-light generation with sub-ps pulses," *Optics Express*, vol. 23, no. 11, pp. 13866–13879, 2015.

[83] M. Bradler, P. Baum, and E. Riedle, "Femtosecond continuum generation in bulk laser host materials with sub-μJ pump pulses," *Applied Physics B*, vol. 97, no. 3, pp. 561–574, 2009.

[84] A. Dubietis, *Netiesinė Optika*. Vilniaus Universiteto leidykla, 2011.

[85] A. Brodeur and S. L. Chin, "Band-gap dependence of the ultrafast white-light continuum," *Phys. Rev. Lett.*, vol. 80, no. 20, pp. 4406–4409, 1998.

[86] M. Sheik-Bahae, D. C. Hutchings, and D. J. Hagan, "Dispersion of bound electronic nonlinear refraction in solids," *IEEE Journal of Quantum Electronics*, vol. 27, no. 6, pp. 1296–1309, 1991.

[87] B. E. Schmidt, P. Béjot, M. Giguére, A. D. Shiner, C. Trallero-Herrero, E. Bisson, J. Kasparian, J.-P. Wolf, D. M. Villeneuve, J.-C. Kieffer, P. B. Corkum, and F. Légaré, "Compression of 1.8 μm laser pulses to sub two optical cycles with bulk material," *Applied Physics Letters*, vol. 96, no. 12, 2010.

[88] G. Andriukaitis, T. Balčiūnas, S. Ališauskas, A. Pugžlys, A. Baltuška, T. Popmintchev, M. Chen, M. M. Murnane, and H. C. Kapteyn, "90 GW peak power few-cycle mid-infrared pulses from an optical parametric amplifier," *Optics Letters*, vol. 36, no. 15, pp. 2755–2757, 2011.

[89] N. Thiré, R. Maksimenka, B. Kiss, C. Ferchaud, P. Bizouard, E. Cormier, K. Osvay, and N. Forget, "4-W, 100-kHz, few-cycle mid-infrared source with sub-100-mrad carrier-envelope phase noise," *Optics Express*, vol. 25, no. 2, pp. 1505–1514, 2017.

[90] A. Baltuška, T. Udem, M. Uiberacker, M. Hentschel, E. Goulielmakis, C. Gohle, R. Holzwarth, V. S. Yakovlev, A. Scrinzi, T. W. Hänsch, and F. Krausz, "Attosecond control of electronic processes by intense light fields," *Letters to Nature*, vol. 421, pp. 611–615, 2003.

[91] A. Baltuška, T. Fuji, and T. Kobayashi, "Controlling the carrier-envelope phase of ultrashort light pulses with optical parametric amplifiers," *Physical Review Letters*, vol. 88, no. 13, 2002.

[92] M. Kakehata, H. Takada, Y. Kobayashi, K. Torizuka, Y. Fujihira, T. Homma, and H.Takahashi, "Single-shot measurement of carrier-envelope phase changes by spectral interferometry," *Optics Letters*, vol. 26, no. 18, pp. 1436–1438, 2001.

[93] M. Görbe, K. Osvay, C. Grebing, and G. Steinmeyer, "Isochronic carrier-envelope phase-shift compensator," *Optics Letters*, vol. 33, no. 22, pp. 2704–2706, 2008.

[94] G. Fan, T. Balčiūnas, T. Kanai, T. Flöry, G. Andriukaitis, B. E. Schmidt, F. Légaré, and A. Baltuška, "Hollow-core-waveguide compression of multi-millijoule CEP-stable 3.2 μm pulses," *Optica*, vol. 3, no. 12, pp. 1308–1311, 2016.

[95] A. Thai, M. Hemmer, P. K. Bates, O. Chalus, and J. Biegert, "Sub-250-mrad, passively carrier-envelope-phase-stable mid-infrared OPCPA source at high repetition rate," *Optics Letters*, vol. 36, no. 19, pp. 3918–3920, 2011.

[96] J. Rothhardt, S. Demmler, S. Hädrich, T. Peschel, J. Limpert, and A. Tünnermann, "Thermal effects in high average power optical parametric amplifiers," *Optics Letters*, vol. 38, no. 5, pp. 763–765, 2013.

[97] R. Riedel, J. Rothhardt, K. Beil, B. Gronloh, A. Klenke, H. Höppner, M. Schulz, U. Teubner, C. Kränkel, J. Limpert, A. Tünnermann, M. Prandolini, and F. Tavella, "Thermal properties of borate crystals for high power optical parametric chirped-pulse amplification," *Optics Express*, vol. 22, no. 15, pp. 17607–17619, 2015.

[98] "InradOptics, White Papers, Zinc Germanium Phosphide."

[99] D. Du, X. Liu, G. Korn, J. Squier, and G. Mourou, "Laser induced breakdown by impact ionization in SiO_2 with pulse widths from 7 ns to 150 fs," *Appl. Phys. Lett.*, vol. 64, no. 3071, 1994.

[100] M. Mero, J. Liu, W. Rudolph, D. Ristau, and K. Starke, "Scaling laws of femtosecond laser pulse induced breakdown in oxide films," *Physical Review B*, vol. 71, no. 11, 2005.

[101] "Eksma optics crystal selection guide," 2013.

[102] F. Bach, M. Mero, M. Chou, F. Noack, and V. Petrov, "High-average-power, picosecond laser induced damage behavior of blank lithium niobate crystals at 1030 nm, ASSL," 2015.

[103] "Lidaris." http://lidaris.com/. Accessed on 2018-12-03.

[104] L. Gallais, D. Douti, M. Commandré, G. Batavičiūtė, E. Pupka, M. Ščiuka, L. Smalakys, V. Sirutkaitis, and A.Melninkaitis, "Wavelength dependence of femtosecond laser-induced damage threshold of optical materials," *Journal of Applied Physics*, vol. 117, 2015.

[105] A. Cabasse, C. Hazera, L. Quintard, E. Cormier, S. Petit, and E. Constant, "Collection and spectral control of high-order harmonics generated with a 50 W high-repetition rate Ytterbium femtosecond laser system," *Journal of Physics B: Atomic, Molecular and Optical Physics*, vol. 49, no. 8, 2016.

[106] C. Jauregui, T. Eidam, H.-J. Otto, F. Stutzki, F. Jansen, J. Limpert, and A. Tünnermann, "Physical origin of mode instabilities in high-power fiber laser systems," *Optics Express*, vol. 20, no. 12, 2012.

[107] J. Darginavičius, N. Garejev, and A. Dubietis, "Generation of carrier-envelope phase-stable two optical-cycle pulses at 2 μm from a noncollinear beta-barium borate optical parametric amplifier," *Optics Letters*, vol. 37, no. 22, pp. 4805–4807, 2012.

[108] C. Homann, M. Bradler, M. Förster, P. Hommelhoff, and E. Riedle, "Carrier-envelope phase stable sub-two-cycle pulses tunable around 1.8 μm at 100 kHz," *Optics Letters*, vol. 37, no. 10, pp. 1673–1575, 2012.

[109] K. Hong, S. Huang, J. Moses, X. Fu, C. Lai, G. Cirmi, A. Sell, E. Granados, P. Keathley, and F. X. Kärtner, "High-energy, phase-stable, ultrabroadband kHz OPCPA at 2.1 μm pumped by a picosecond cryogenic Yb:YAG laser," *Optics Express*, vol. 19, no. 16, pp. 15538–15548, 2011.

[110] J. Moses, S. Huang, K. Hong, O. D. Mücke, E. L. F. ao Filho, A. Benedick, F. O. Ilday, A. Dergachev, J. A. Bolger, B. J. Eggleton, and F. X. Kärtner, "Highly stable ultrabroadband mid-IR optical parametric chirped-pulse amplifier optimized for superfluorescence suppression," *Optics Express*, vol. 34, no. 11, pp. 1639–1641, 2009.

[111] J.Nillon, S. Montant, G. Machinet, and E. Cormier, "Phase-stabilized few-cycle optical parametric amplification at 2.1 μm with 10 μJ at 100 kHz; Lasers, Sources, and Related Photonic Devices Technical Digest," 2012.

[112] X. Gu, G. Marcus, Y. Deng, T. Metzger, C. Teisset, N. Ishii, T. Fuji, A. Baltuska, R. Butkus, V. Pervak, H. Ishizuki, T. Taira, T. Kobayashi, R. Kienberger, and F. Krausz, "Generation of carrier-envelope-phase-stable 2-cycle 740 μJ pulses at 2.1 μm carrier wavelength," *Optics Express*, vol. 17, no. 1, pp. 62–69, 2008.

[113] B. E. Schmidt, A. D. Shiner, P. Lassonde, J.-C. Kieffer, P. B. Corkum, D. M. Villeneuve, and F. Légaré, "CEP stable 1.6 cycle laser pulses at 1.8 μm," *Optics Express*, vol. 19, no. 7, pp. 6858–6864, 2011.

[114] Y. Pertot, C. Schmidt, M. Matthews, A. Chauvet, M. Huppert, V. Svoboda, A. von Conta, A. Tehlar, D. Baykusheva, J.-P. Wolf, and H. J. W orner, "Time-resolved x-ray absorption spectroscopy with a water window high-harmonic source," *Science*, vol. 355, no. 6322, 2017.

[115] G. Archipovaite and R. Butkus, "Generation and parametric amplification of broadband pulses at 2 μm; New Years Physics Conference, *LT*Φ," 2015.

[116] N. Tolstik, E. Sorokin, and I. T. Sorokina, "Graphene mode-locked Cr:ZnS laser with 41 fs pulse duration," *Optics Express*, vol. 22, no. 5, pp. 5564–5571, 2014.

[117] P. Moulton and E. Slobodchikov, "1-GW-Peak-Power, Cr:ZnSe Laser; CLEO," 2011.

[118] S. Duval, M. Bernier, V. Fortin, J. Genest, M. Piché, and R. Vallée, "Femtosecond fiber lasers reach the mid-infrared," *Optica*, vol. 2, no. 7, pp. 623–626, 2015.

[119] P. Rigaud, A. V. de Walle, M. Hanna, N. Forget, F. Guichard, Y. Zaouter, K. Guesmi, F. Druon, and P. Georges, "Supercontinuum-seeded few-cycle mid-infrared OPCPA system," *Optics Express*, vol. 24, no. 23, pp. 26494–26502, 2016.

[120] G. Archipovaite, S. Petit, J.-C. Delagnes, and E. Cormier, "100 kHz Yb-fiber laser pumped 3 μm optical parametric amplifier for probing solid-state systems in the strong field regime," *Optics Letters*, vol. 42, no. 5, pp. 891–894, 2017.

[121] M. Mero, F. Noack, F. Bach, V. Petrov, and M. J. J. Vrakking, "High-average-power, 50-fs parametric amplifier front-end at 1.55 μm," *Optics Express*, vol. 23, no. 26, pp. 33157–33163, 2015.

[122] B. W. Mayer, C. R. Phillips, L. Gallmann, and U. Keller, "Mid-infrared pulse generation via achromatic quasi-phase-matched OPCPA," *Optics Express*, vol. 22, no. 17, pp. 20798–20808, 2014.

[123] P. R. Krogen, H. Suchowski, G. J. Stein, F. X. Kärtner, and J. Moses, "Tunable few-cycle Mid-IR pulses towards single-cycle duration by adiabatic frequency conversion," 2014.

[124] L. Gallmann, *Sources and techniques for attosecond science*. PhD thesis, ETH Zurich, 2011.

[125] M. Baudisch, H. Pires, H. Ishizuki, T. Taira, M. Hemmer, and J. Biegert, "Sub-4-optical-cycle, 340 MW peak power, high stability mid-IR source at 160 kHz," *Journal of Optics*, vol. 17, no. 9, 2015.

[126] D. Kane and R. Trebino, "Characterization of arbitrary femtosecond pulses using frequency-resolved optical gating," *IEEE*, vol. 29, no. 2, 1993.

[127] J. J. Boy, M. Allani, N. Batis, O. Bel, O. Cambon, J. Haines, P. Roumanille, K. Lebbou, H. Cabane, A. E. Hassouni, and C. Pecheyran, "New LGT crystal for ultra-stable resonators," *IEEE*, no. 28, pp. 75–78, 2014.

[128] S. A. Sakharov, A. N. Zabelin, O. A. Buzanov, D. V. Roshchupkin, and M. Y. Barabanenkov, "Physical properties of lanthanum gallium tantalate crystals for high-temperature application," *IEEE*, 2005.

[129] H. Kong, J. Wang, H. Zhang, X. Y. X. Cheng, Y. Lin, X. Hu, X. Xu, and M. Jiang, "Growth and characterization of $La_3Ga_{5.5}Ta_{0.5}4O_{14}$ crystal," *Cryst. Res. Technol*, no. 39, pp. 686–691, 2004.

[130] P. Malevich, T. Kanai, H. Hoogland, R. Holzwarth, A. Baltuška, and A. Pugžlys, "Broadband mid-infrared pulses from potassium titanyl arsenate/zinc germanium phosphate optical parametric amplifier pumped by Tm, Ho-fiber-seeded Ho:YAG chirped-pulse amplifier," *Optics Letters*, vol. 41, no. 5, pp. 930–934, 2016.

[131] D. Sanchez, M. Hemmer, M. Baudisch, S. L. Cousin, K. Zawilski, P. Shunemann, O. Chalus, C. Simon-Boisson, and J. Biegert, "7 μm, ultrafast, sub-millijoule-level mid-infrared optical parametric chirped pulse amplifier pumped at 2 μm," *Optica*, no. 2, pp. 147–150, 2016.

[132] "Fomos materials, http://newpiezo.com/langatate.html." Accessed on 2017-12-18.

[133] E. Boursier, *Génération paramétrique infrarouge dans les cristaux de* $La_3Ga_{5,5}Ta_0,5O_{14}$ *et* $BaGa_4Se_7$. PhD thesis, Université Grenoble Alpes, 2016.

[134] D. Sutter, I. Jung, N. Matuschek, F. Morier-Genoud, F. Kärtner, U. Keller, V. Scheuer, M. Tilsch, and T. Tschudi, "300 nm tunability of 30-fs Ti:sapphire laser pulses with a single set of double chirped mirrors; CLEO," 1998.

[135] "MIRA 900." https://www.coherent.com/lasers/laser/mira-900. Accessed on 2018-03-28.

[136] T. Metzger, A. Schwarz, C. Y. Teisset, D. Sutter, A. Killi, R. Kienberger, and F. Krausz, "High-repetition-rate picosecond pump laser based on a Yb:YAG disk amplifier for optical parametric amplification," *Optics Letters*, vol. 34, no. 14, 2009.

[137] M. Grishin, V. Gulbinas, and A. Michailovas, "Bifurcation suppression for stability improvement in Nd:YVO4 regenerative amplifier," *Optics Express*, vol. 17, no. 18, 2009.

[138] Y. Yao, A. J. Hoffman, and C. F. Gmachl, "Mid-infrared quantum cascade lasers," *Nature Photonics*, vol. 6, pp. 432–439, 2012.

[139] K. L. Vodopyanov, I. Makasyuk, and P. G. Schunemann, "Grating tunable 4 - 14 μm GaAs optical parametric oscillator pumped at 3 μm," *Optics Express*, vol. 22, no. 4, pp. 4131–4136, 2014.

[140] V. Petrov, "Frequency down-conversion of solid-state laser sources to the mid-infrared spectral range using non-oxide nonlinear crystals," *Progress in Quantum Electronics*, vol. 42, pp. 1–106, 2015.

[141] I. Pupeza, D. Sánchez, J. Zhang, N. Lilienfein, M. Seidel, N. Karpowicz, T. Paasch-Colberg, I. Znakovskaya, M. Pescher, W. Schweinberger, V. Pervak, E. Fill, O. Pronin, Z.Wei, F. Krausz, A. Apolonski, and J. Biegert, "High-power sub-two-cycle mid-infrared pulses at 100 MHz repetition rate," *Nature Photonics*, vol. 9, pp. 721–725, 2015.

[142] O. Novák, P. R. Krogen, T. Kroh, T. Mocek, F. X. Kärtner, and K.-H. Hong, "A CEP-stable, femtosecond 8.5 μm source based on intrapulse DFG of 2.1 μm pulses; CLEO/Europe-EQEC," 2017.

[143] V. Petrov, F. Rotermund, and F. Noack, "Generation of high-power femtosecond light pulses at 1 kHz in the mid-infrared spectral range between 3 and 12 μm by second-order nonlinear processes in optical crystals," *J. Opt. A: Pure Appl. Opt*, vol. 3, pp. 1–19, 2001.

[144] V. Kozich, A.Moguilevski, and K.Heyne, "High energy femtosecond OPA pumped by 1030nm Yb:KGW laser," *Optics Communications*, vol. 285, no. 21-22, pp. 4515–4518, 2012.

[145] E. A. Migal, F. V. Potemkin, and V. M. Gordienko, "Highly efficient optical parametric amplifier tunable from near to mid-IR for driving extreme nonlinear optics in solids," *Optics Letters*, vol. 42, no. 24, pp. 5218–5221, 2017.

[146] Q. Ru, N. Lee, X. Chen, K. Zhong, G. Tsoy, M. Mirov, S. Vasilyev, S. B. Mirov, and K. L. Vodopyanov, "Optical parametric oscillation in a random polycrystalline medium," *Optica*, vol. 4, no. 6, pp. 617–618, 2017.

[147] C. Patel, "Optical harmonic generation in the infrared using a CO_2 laser," *Physical Review Letters*, vol. 16, no. 14, pp. 613–616, 1966.

[148] R. Kesselring, A. Kälin, and F. Kneubühl, "Mid-infrared nonlinear phenomena in polycrystalline semiconductors," *Applied Physics B*, vol. 55, pp. 437–445, 1992.

[149] S. Vasilyev, I. Moskalev, M. Mirov, V. Smolski, S. Mirov, and V. Gapontsev, "Mid-IR Kerr-lens mode-locked polycrystalline Cr:ZnS and Cr:ZnSe lasers with intracavity frequency conversion via random quasiphase-matching," 2016.

[150] T. D. Chinh, W. Seibt, and K. Siegbahn, "Dot patterns from second-harmonic and sum-frequency generation in polycrystalline ZnSe," *Journal of Applied Physics*, vol. 90, no. 5, p. 2612, 2001.

[151] A. H. Chin, O. G. Calderón, and J. Kono, "Extreme mid-infrared nonlinear optics in semiconductors," *Physical Review Letters*, vol. 86, no. 15, pp. 3292–3295, 2001.

[152] R. Cireasa, A. E. Boguslavskiy, B. Pons, M. C. H.Wong, D. Descamps, S. Petit, H. Ruf, N. Thiré, A. Ferré, J. Suarez, J. Higuet, B. E. Schmidt, A. F. Alharbi, F. Légaré, V. Blanchet, B. Fabre, S. Patchkovskii, O. Smirnova, Y. Mairesse, and V. R. Bhardwaj, "Probing molecular chirality on a sub-femtosecond timescale," *Nature Physics Letters*, vol. 11, pp. 654–661, 2015.

[153] E. A. Gibson, A. Paul, N. Wagner, R. Tobey, D. Gaudiosi, S. Backus, I. P. Christov, A. Aquila, E. M. Gullikson, D. T. Attwood, M. M. Murnane, and H. C. Kapteyn, "Coherent soft X-ray generation in the water window with quasi-phase matching," *Science*, vol. 302, no. 15, pp. 95–98, 2003.

[154] I. J. Sola, E. Mével, L. Elouga, E. Constant, V. Strelkov, L. Poletto, P. Villoresi, E. Benedetti, J.-P. Caumes, S. Stagira, C. Vozzi, G. Sansone, and M. Nisoli, "Controlling attosecond electron dynamics by phase-stabilized polarization gating," *Nature Physics Letters*, vol. 2, pp. 319–322, 2006.

[155] A. Baltuska, T. Udem, M. Uiberacker, M. Hentschel, E. Goulielmakis, C. Gohle, R. Holzwarth, V. S. Yakovlev, A. S. T. W. Hänsch, and F. Krausz, "Attosecond control of electronic processes by intense light fields," *Letters to Nature*, vol. 42, pp. 611–615, 2003.

[156] S. L. Cousin, F. Silva, S. Teichmann, M. Hemmer, B. Buades, and J. Biegert, "High-flux table-top soft x-ray source driven by sub-2-cycle, CEP stable, 1.85-µm 1-kHz pulses for carbon K-edge spectroscopy," *Optics Letters*, vol. 39, no. 18, pp. 5383–5386, 2014.

[157] M.-C. Chen, C. Mancuso, C. Hernndez-Garca, F. Dollar, B. Galloway, D. Popmintchev, P.-C. Huang, B. Walker, L. Plaja, A. Jaron-Becker, A. Becker, M. M. Murnane, H. C. Kapteyn, and T. Popmintchev, "Generation of bright isolated attosecond soft X-ray pulses driven by multicycle midinfrared lasers," *PNAS*, pp. 2361–2367, 2014.

[158] I. Pupeza, S. Holzberger, T. Eidam, H. Carstens, D. Esser, J. Weitenberg, P. Rußüldt, J. Rauschenberger, J. Limpert, T. Udem, A. Tünnermann, T. W. Hänsch, A. Apolonski, F. Krausz, and E. Fill, "Compact high-repetition-rate source of coherent 100 eV radiation," *Nature Photonics*, no. 7, pp. 608–612, 2013.

[159] M. Gaponenko, F. Labaye, V. J. Wittwer, C. Paradis, N. Modsching, L. Merceron, A. Diebold, F. Emaury, I. J. Graumann, C. R. Phillips, C. J. Saraceno, C. Kränkel, U. Keller, and T. Südmeyer, "High harmonic generation (HHG) inside a modelocked thin-disk laser; FiO/LS," 2017.

[160] M. Schultze, C. Wandt, S. Klingebiel, C. Y. Teisset, M. Häfner, R. Bessing, T. Herzig, S. Prinz, S. Stark, K. Michel, and T. Metzger, "Toward kilowatt-level ultrafast regenerative thin-disk amplifiers," *ASSL*, 2016.

[161] P. Russbueldt, T. Mans, J. Weitenberg, H. D. Hoffmann, and R. Poprawe, "Compact diode-pumped 1.1 kW Yb:YAG innoslab femtosecond amplifier," *Optics Letters*, vol. 35, no. 24, pp. 4169–4171, 2010.

[162] A. Vernaleken, J. Weitenberg, T. Sartorius, P. Russbueldt, W.Schneider, S. L. Stebbings, M. F. Kling, P. Hommelhoff, H.-D. Hoffmann, R. Poprawe, F. Krausz, T. W. Hänsch, and T. Udem, "Single-pass high-harmonic generation at 20.8 MHz repetition rate," *Optics Letters*, vol. 36, no. 17, pp. 3248–3230, 2011.

[163] B. Shan and Z. Chang, "Dramatic extension of the high-order harmonic cutoff by using a long-wavelength driving field," *Physical Review A*, vol. 65, 2001.

[164] D. Riedel, J. L. Hernandez-Pozos, R. E. Palmer, S. Baggott, K. W. Kolasinski, and S. Foord, "Tunable pulsed vacuum ultraviolet light source for surface science and materials spectroscopy based on high order harmonic generation," *Review of Scientific Instruments*, vol. 72, no. 4, pp. 1977–1983, 2001.

[165] P. Colosimo, G. Doumy, C. I. Blaga, J. Wheeler, C. Hauri, F. Catoire, J. Tate, R. Chirla, A. M. March, G. G. Paulus, H. G. Muller, P. Agostini, and L. F. Dimauro, "Scaling strong-field interactions towards the classical limit," *Nature Physics*, vol. 4, pp. 386–389, 2008.

[166] S. L. Cousin, F. Silva, S. Teichmann, M. Hemmer, B. Buades, and J. Biegert, "High-flux table-top soft X-ray source driven by sub-2-cycle, CEP stable, 1.85 µm 1-khz pulses for carbon K-edge spectroscopy," *Optics Letters*, vol. 39, no. 18, pp. 5583–5586, 2014.

[167] C. Ding, W. Xiong, T. Fan, D. D. Hickstein, T. Popmintchev, X. Zhang, M. Walls, M. M. Murnane, and H. C. Kapteyn, "High flux coherent super-continuum soft X-ray source driven by a single-stage, 10mJ, Ti:sapphire amplifier-pumped OPA," *Optics Express*, vol. 22, no. 5, pp. 6194–6202, 2014.

[168] Z. Chang, P. B. Corkum, and S. R. Leone, "Attosecond optics and technology: progress to date and future prospects," *JOSA B*, vol. 33, no. 6, pp. 1081–1097, 2016.

[169] M. Baudisch, A. Thai, M. Hemmer, H. Ishizuki, T. Taira, and J. Biegert, "5-cycle, 160-kHz, 20- µJ mid-IR OPCPA," 2013.

[170] R. Torres, T. Siegel, L. Brugnera, I. Procino, J. G. Underwood, C. Altucci, R. Velotta, E. Springate, C. Froud, I. C. E. Turcu, M. Y. Ivanov, O. Smirnova, and J. P. Marangos, "Extension of high harmonic spectroscopy in molecules by a 1300 nm laser field," *Optics Express*, vol. 18, no. 3, 2010.

[171] V.Cardin, N. Thiré, S. Beaulieu, V. Wanie, F. Légaré, and B. E. Schmidt, "0.42?TW 2-cycle pulses at 1.8?µm via hollow-core fiber compression," *Applied Physics Letters*, vol. 107, 2015.

[172] "X-Ray database, http://henke.lbl.gov/optical_constants/filter2.html."

[173] M. N. Polyanskiy, "Refractive index database." https://refractiveindex.info. Accessed on 2017-12-07.

[174] S. Hädrich, J. Rothhardt, M. Krebs, F. Tavella, A. Willner, J. Limpert, and A. Tünnermann, "High harmonic generation by novel fiber amplifier based sources," *Optics Express*, vol. 18, no. 19, pp. 20242–20250, 2010.

[175] S. Hädrich, A. Klenke, J. Rothhardt, M. Krebs, A. Hoffmann, O. Pronin, V. Pervak, J. Limpert, and A. Tünnermann, "High photon flux table-top coherent extreme-ultraviolet source," *Nature Photonics*, vol. 8, pp. 779–783, 2014.

[176] A. Comby, S. Beaulieu, E. Constant, D. Descamps, S. Petit, and Y. Mairesse, "Absolute gas density profiling in high-order harmonic generation," *Optics Express*, vol. 26, no. 5, 2018.

[177] M. Krebs, S. Hädrich, S. Demmler, J. Rothhardt, A. Zaïr, L. Chipperfield, J. Limpert, and A. Tünnermann, "Towards isolated attosecond pulses at megahertz repetition rates," *Nature Photonics*, vol. 7, pp. 555–559, 2013.

[178] G. K. Tadesse, R. Klas, S. Demmler, S. Hädrich, I. Wahyutama, M. Steinert, C. Spielmann, M. Zürch, T. Pertsch, A. Tünnermann, J. Limpert, and J. Rothhardt, "High speed and high resolution table-top nanoscale imaging," *Nature Photonics*, vol. 41, no. 22, pp. 5170–5173, 2016.

Appendix A

Report on the homogeneity test of the two large aperture KTA crystals

Objective: To test the homogeneity of the large aperture KTA crystals, the aim is to compare the two crystals and choose one to use with large aperture beams.

Crystal characteristics:
KTA cut: $\Theta = 42^\circ$, $\phi = 0^\circ$;
Size: 25 mm $\times 25mm \times 4mm$;
Coatings:$Tbar/1030 + 1300 - 1900 + 2300 - 4200(OPO@1030nm)$

First crystal

Experimental conditions

The 3 μm OPA described in chapter 2 has been used to test the crystal homogeneity by replacing the third stage crystal with the large aperture KTA. A seed beam at 3.2 μm with 21 mW (210 nJ) is mixed with 17.4 W (174 μJ) of pump at 1030 nm. Due to the lack of space we had to perform the transverse scan for the whole area of the crystal, when it was placed at the original stage position of the OPA, the test was done with the crystal position shifted by 6 cm away from the waist. Thus, the amplification efficiency was lower, due to the nonoptimal mode sizes of both signal and pump beams.

Results

The crystal was tested at 25 points (5 rows, 5 columns). The crystal was translated horizontally and vertically maintaining the same spectrum of amplified pulses. A summary of the results is provided below: Table A.1 shows the distribution of power of amplified signal and Table A.2 the normalized efficiency. The shaded table cells marks the position of margin amplification: green shows efficient amplification and orange, no efficient areas on the crystal. The quality of the spots is defined by the amplification efficiency, where the efficient point has the amplification efficiency of 75 % or higher and a non-efficient spot has the amplification efficiency of 25 % or lower.

Table A.1 Power distribution of amplified signal (mW).

82	77	47	42	57
98	96	72	83	39
99	53	100	110	99
49	88	94	97	107
45	41	51	64	86

Table A.2 Normalized efficiency of amplified signal.

0.6	0.5	0.1	0.05	0.2
0.8	0.8	0.5	0.6	0
0.8	0.2	0.9	1	0.8
0.1	0.7	0.8	0.8	0.9
0.1	0.02	0.2	0.3	0.7

The actual location of the measured spots is provided if Fig.A.1. The red dots correspond to the actual spot, where the amplification took place together with the power of amplified signal in mW. At locations, where only the power is indicated, it was not possible to identify the exact OPA position. This was due to the lack of visible scattering from the crystal. The identification of positions was done by treating scattered SHG position at the crystal from the pictures taken at each point.

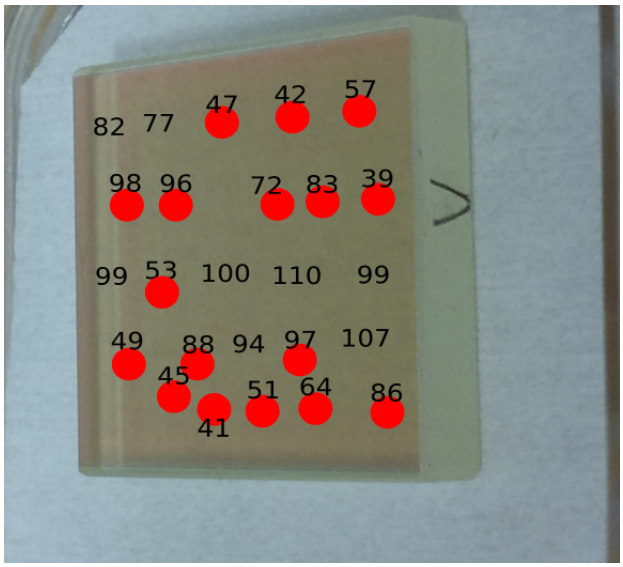

Figure A.1 The map of measured points at the crystal.

The non-uniform shape of back scattering is also observed (see Fig.A.2). The efficiency of SHG and SFG inversely correlates with the efficiency of OPA at 3.2 μm; the mode quality is worsened at low efficiency points. In the case of low amplification, the SHG and SFG beams are distorted, and exit the crystal at different angles with higher divergences. At higher efficiency points, the SHG and SFG beam profiles maintain an almost Gaussian shape, the angle between the two beams remains small and the divergence is low.

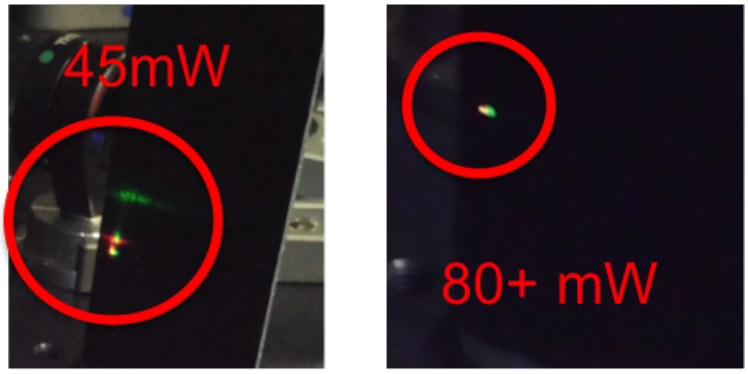

Figure A.2 The back scattering at different spots on the crystal.

Comparing the amplification efficiency of the 6 mm KTA crystal with the 4 mm KTA is that the best point of the large aperture crystal is about 2.5 times lower. In the 6 mm crystal, the amplified signal reaches 275 mW (2.75 μJ), efficiency – 1.5 % in the same conditions. The simulation of amplification in both crystals was done by SNLO program and the results

are provided in Fig.A.3. Theoretically, the amplified signal in 6 mm KTA crystal should be 3 times higher than in 4 mm KTA; the experimental result is 2.5 times higher. It is however hard to conclude from the comparison of just two crystals, as a variation from the theoretical estimation could be impacted by various factors for example: a different coating of the two crystals, the 6 mm crystal has some damaged spots, but the fact that the amplification difference is smaller would indicate that the 6 mm crystal is not amplifying enough rather than that the fault is in the 4 mm crystal.

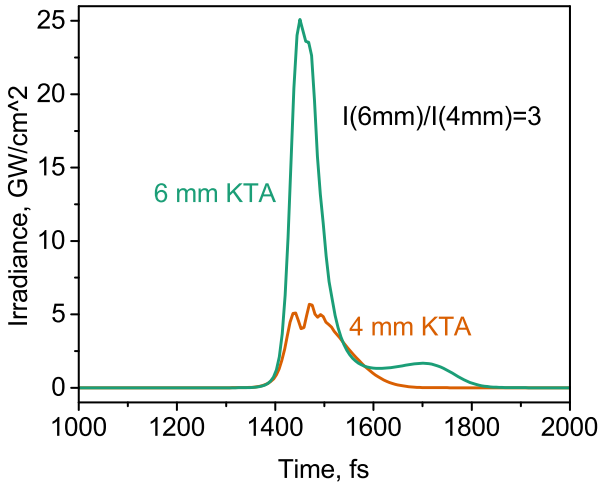

Figure A.3 Results of SNLO simulation of OPA in 6 mm and 4 mm KTA crystals.

Second crystal

Experimental conditions

The test was performed with very similar conditions as for the first KTA crystal. A seed beam at 3.2 µm with 20 mW (200 nJ) is mixed with 18 W (180 µJ) of pump at 1030 nm. Again, due to the lack of space we had to perform the transverse scan for the whole area of the crystal, when it was placed at the original stage position of the OPA, the test was done with the crystal position shifted by 6 cm away from the waist. Thus, the amplification efficiency was lower due to the non optimized mode sizes of both signal and pump beams.

Results

The crystal was tested at 25 points (5 rows, 5 columns). The crystal was translated horizontally and vertically maintaining the same spectrum of amplified pulses. This time the crystal mounting was improved – a two-dimensional translation stage was used to translate the crystal. This way, the measured crystal positions are equally distributed. A summary of the results is provided below: Table.A.3 shows the distribution of the power of the amplified signal and Table.A.4, the normalized efficiency.

Table A.3 Power distribution of amplified signal (mW).

193	317	323	297	327
216	345	322	107	339
129	147	133	326	111
62	162	262	255	164
127	142	104	268	150

Table A.4 Normalized efficiency of amplified signal.

0.46	0.9	0.92	0.83	0.94
0.54	1	0.92	0.16	0.98
0.24	0.3	0.25	0.93	0.17
0	0.35	0.71	0.68	0.36
0.23	0.28	0.15	0.73	0.31

The actual location of the measured spots is provided if Fig.A.4. The red dots correspond to the actual spot where the amplification took place together with the power of amplified signal in mW.

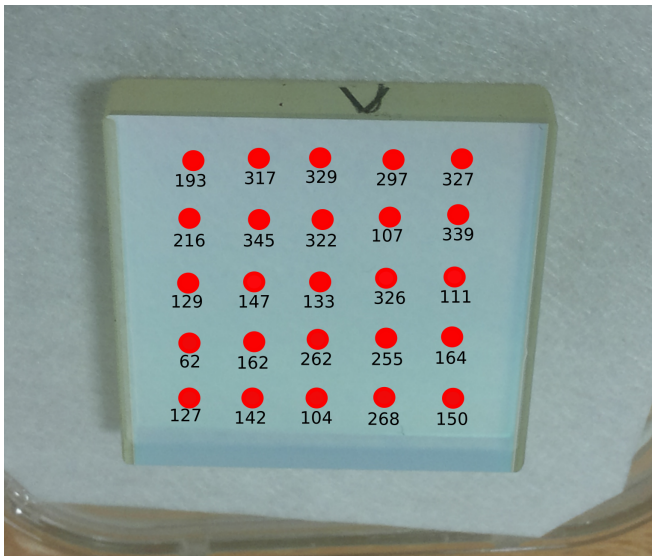

Figure A.4 The map of measured points at the crystal.

The non-uniform shape of back scattering is again observed (Fig.A.5). The efficiency of SHG and SFG inversely correlates with the efficiency of OPA at 3.2 μm, and the mode quality is worsened at lower efficiency points. In the case of low amplification, the SHG and SFG beams are distorted, also exit the crystal at different angles with higher divergence. At higher efficiency points, the SHG and SFG beam profiles maintain an almost Gaussian shape, the angle between the two beams is maintained small and the divergence is low. Here, the effect is weaker than in the first large aperture crystal – the overall scattering is higher and only at the highest amplification points the beam reaches an almost Gaussian shape. Also at different points, different beams (SHG or SFG) could be affected. In b) the stronger scattering is on the SFG, while in c) the SFG beam was only slightly affected and the SHG was strongly distorted.

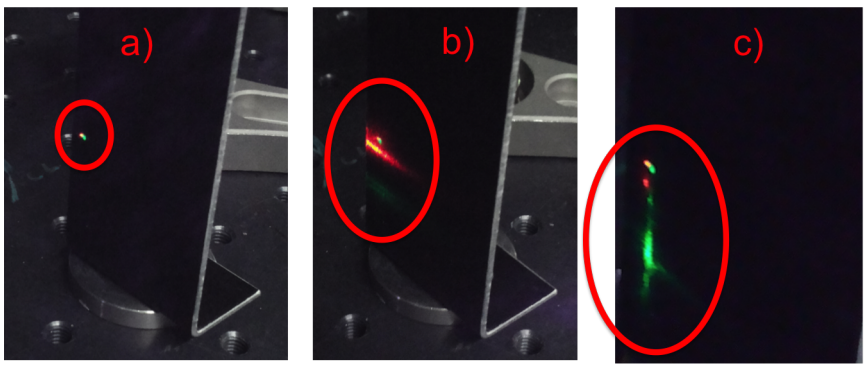

Figure A.5 The back scattering at different spots on the crystal.

Comparison with 6 mm KTA crystal

Comparing the amplification efficiency with the 6 mm KTA crystal the difference is about 1.7 times more at the best point of the large aperture 4 mm KTA. In the 6 mm crystal, the amplified signal reaches 580 mW (5.8 μJ), efficiency– 3.2 % under the same conditions. The simulation of amplification in both crystals was done by SNLO program and the results are provided in Fig.A.3. Theoretically, the amplified signal in the 6 mm KTA crystal should be 3 times higher than in 4 mm KTA; the experimental result is 1.7 times higher. It is again smaller than expected. However, now the ratio is reduced by half. The increased variation from the theoretical value could be due to the non-homogeneity of the smaller 6 mm KTA crystal as the beams interacted in a different spot compared to the previous test.

Comparison between the two 4 mm crystals

Table A.5 Normalized efficiency in the 1st KTA crystal.

0.6	0.5	0.1	0.05	0.2
0.8	0.8	0.5	0.6	0
0.8	0.2	0.9	1	0.8
0.1	0.7	0.8	0.8	0.9
0.1	0.02	0.2	0.3	0.7

Table A.6 Normalized efficiency in the 2nd KTA crystal.

0.46	0.9	0.92	0.83	0.94
0.54	1	0.92	0.16	0.98
0.24	0.3	0.25	0.93	0.17
0	0.35	0.71	0.68	0.36
0.23	0.28	0.15	0.73	0.31

Normalized efficiencies of both crystals are shown in Table.A.5 (first crystal) and Table.A.6 (second/new crystal). The amount of efficient spots (more than 0.75) is similar – 7 in the first and 8 in the 2nd and the number of less efficient spots (less than 0.25) is slightly higher in the first crystal (9 vs 8). The relative efficiencies are higher in the 2nd crystal, which could lead to the conclusion that it has a higher quality.

Sources Paramétriques de Haute Energie et de Haute Cadence dans l'infrarouge Moyen et leurs Applications en Champ Fort

Les sources lasers à impulsions ultracourtes de forte puissance dans la région spectrale du proche à moyen infrarouge sont très demandées pour la physique des champs forts dans les atomes, les molécules et la matière condensée. D'après le modèle en trois étapes [1], l'énergie coupée des harmoniques élevées générées varie comme $I\times\lambda^2$. Cela favorise les longueurs d'onde plus longues pour générer des photons XUV plus énergétiques, et potentiellement des impulsions attosecondes plus courtes. Malheureusement, l'extension de l'énergie des photons se fait au prix d'une diminution de l'efficacité en $\lambda^{-5,5}$ [2]. La disponibilité d'un système laser a haute cadence est un atout majeur pour palier aux problèmes d'efficacité et produire des flux de photons élevés. Même s'il existe quelques matériaux de gain laser adaptes a la génération d'impulsions femtoseconde intense dans la région spectrale infrarouge intermédiaire, l'amélioration globale du taux de répétition, de la durée et de la puissance des impulsions sont encore des défis [3, 4]. Ainsi, les systèmes paramétriques bases sur un mélange non linéaire à trois ondes sont une alternative intéressante pour générer les impulsions ultracourtes requises pour ce type d'expériences. Actuellement, les systèmes paramétriques à haute puissance dans l'infrarouge moyen ne peuvent pas atteindre les intensités requises pour générer des harmoniques dans le gaz. Cependant, ces sources sont des moteurs intéressants pour la génération d'harmonique (HHG) dans les solides, qui nécessitent des intensités sur cible plus faibles. Par ailleurs, les systèmes à haute énergie, mais à taux de répétition plus bas, sont capables de générer des impulsions suffisamment énergétiques pour les expériences HHG dans le gaz. Cependant, l'efficacité globale de ces sources est encore faible. En fonction de l'énergie harmonique requise, le rayonnement peut être génère efficacement par des lasers NIR post-comprimes. Cette thèse décrit le développement des sources MWIR et leurs applications en physique des champs forts. Nous avons choisi d'étudier des sources paramétriques pilotées par un laser à pompe CPA de puissance moyenne élevée et par un système laser a grande énergie Yb: CaF_2. Les impulsions MWIR générées sont ensuite utilisées pour sonder l'interaction du matériau laser à travers HHG dans les solides et les gaz.

Mots clés : Sources Paramétriques, l'infrarouge Moyen, génération d'harmonique

---

High Energy and High Repetition Rate Parametric Sources in the Mid-Wavelength Infrared and their Applications

Ultrashort pulse light sources in the near- to mid-wavelength infrared spectral region are in high demand for strong field physics in atoms, molecules and condensed matter. According to the three step model [1], the energy cut off of generated high harmonics scales as $I\times\lambda^2$, which favors longer driving wavelengths in order to generate more energetic XUV photons, and potentially shorter attosecond, soft X-ray pulses. Unfortunately, photon energy extension is at the cost of an efficiency drop scaling as $\lambda^{-5.5}$ [2]. The availability of a high-repetition rate laser system is paramount to mitigate the efficiency issues and still produce high photon fluxes. Even though there are only a few laser gain media suitable for intense femtosecond pulse generation in the mid-IR spectral region, the overall scalability of the pulse repetition rate, the duration and power are still a challenge [3, 4]. Thus, parametric systems based on a nonlinear three wave-mixing, are an attractive alternative to generate the required ultrashort pulses for those experiments. Currently high power middle infrared parametric systems can't reach the required intensities to reliably drive high harmonic generation (HHG) in gas. However, these sources are attractive drivers for HHG in solids, which requires lower intensities on the target. On the other hand, high energy, but lower repetition rate systems are capable of generating energetic pulses for HHG experiments in gas. However, the overall efficiency of those drivers is still low. Depending on the required harmonics energy, the XUV could be efficiently generated by post-compressed NIR lasers. This thesis describes the development of MWIR sources and their applications in strong field physics. We have chosen to investigate parametric sources driven by high average power fiber CPA pump laser and by high energy Yb:CaF_2 bulk laser system. The generated MWIR few cycle pulses are then used to probe laser material interaction through HHG in solids and gas.

Keywords : Parametric sources, mid-wavelength infrared, high harmonic generation

---

CELIA, UMR5107, l'Université Bordeaux, 43 rue Pierre Noailles, TALENCE